

DISCRIMINATION OF ELEVATED CONVECTION BASED ON LOW-LEVEL
RADAR-DERIVED CONVERGENCE

A Thesis Presented to the Faculty of the Graduate School at the University of Missouri

In Partial Fulfillment of the Requirements for the Degree Masters of Science

by

RYAN J. DIFANI

Dr. Neil Fox, Thesis Advisor

JULY 2016

The undersigned, appointed by the dean of Graduate School, have examined the thesis entitled

DISCRIMINATION OF ELEVATED CONVECTION BASED ON LOW-LEVEL
RADAR-DERIVED CONVERGENCE

Presented by Ryan J. Difani,

a candidate for the degree of master of science,

and hereby certify that, in their opinion, it is worthy of acceptance.

Associate Professor Neil Fox

Professor Patrick Market

Professor Chris Wikle

Acknowledgements

First, I would like to extend my sincerest gratitude to my thesis committee, Dr. Chris Wikle, Dr. Patrick Market and especially my thesis committee chair and advisor, Dr. Neil Fox. I am especially grateful for your guidance and patience while conducting this research. Also, thanks to the National Science Foundation for funding this thesis work. Furthermore, again to Dr. Market and Dr. Fox, as well as Dr. Lupo and Dr. Svoma, I would like to say thank you for your wisdom and expertise that has been, in some small part, passed down to me through graduate coursework taken during my time here. I would also like to extend thanks to my fellow graduate students, not only for moral support along the way, but also for always being there to be a helping hand and so willing to teach me as well as being there for great times both in and out of the office.

Next, I would also like to thank my friends and family outside of the department for all of their support and encouragement. Thanks goes out specifically to those a part of Graduate Christian Fellowship, C2 (Christian Chapel) Church, Mizzou Chi Alpha and Graduate/d Lifegroup. I cannot possibly imagine my time at Mizzou without the people in these groups becoming a part of my life. Moreover, thanks to my family back home in Arkansas. I love and appreciate you so much for more than words could ever express.

Lastly, and most importantly, I would like to thank God for not only providing me the opportunity and pleasure to continue to pursue my education but also for wisdom, joy, strength, peace and my salvation. Can we not better understand the creation (including our atmosphere) if we first get to know the Creator? *“For the invisible things of Him from the creation of the world are clearly seen, being understood by the things that are made, even His eternal power and Godhead;” – Romans 1:20a (KJV)*

Table of Contents

Acknowledgements.....	ii
List of Figures.....	v
List of Tables	ix
Abstract.....	x
Chapter 1 Introduction	1
1.1 Purpose and Objectives.....	2
Chapter 2 Literature Review	4
2.1 Elevated Convection Defined	4
2.2 Elevated Convection Climatology	5
2.3 Thermodynamic Environment of Elevated Convection	8
2.4 Synoptic Conditions for Elevated Convection.....	9
2.5 Lifting Mechanisms of Elevated Convection	13
2.6 Severe Hazards Related to Elevated Convection.....	16
2.7 An Insufficient Understanding of Elevated Convection.....	18
2.7.1 Modeling Evidence for Redefining Elevated Convection	20
2.7.2 Observational Evidence for Redefining Elevated Convection	24
2.7.3 Summary of a Redefined Understanding of Elevated Convection	26
2.7.4 The Effective Inflow Layer.....	27
2.8 Radar Observations of Elevated Convection	28
2.8.1 Intensity Considerations.....	28
2.8.2 Gust Fronts and Cold-Pools.....	29
2.8.3 Observed Wave-Like Features.....	31
2.8.4 Summary of Radar Observations of Elevated Convection	32

Chapter 3 Methodology	34
3.1 Event Selection: Elevated Cases	34
3.1.1 Field Deployment Criteria	36
3.2 Event Selection: Surface-Based Case	37
3.3 Radar Data Retrieval and Processing.....	38
3.4 Selected Radar Products	39
3.5 MATLAB Analysis.....	41
3.5.1 Z_{DR} Column Location	42
3.5.2 Definition and Identification of a “Convergence Column”	44
3.5.3 Vertical Cross-Sections.....	48
3.6 Cell Selection	48
Chapter 4 Results	50
4.1 Thermodynamic Overview of Cases.....	50
4.2 Elevated Case Study	53
4.3 Surface-Based Case Study	67
4.4 Elevated versus Surface-Based Convergence Comparisons.....	77
4.5 Remaining IOP Convergence Column Summaries.....	82
Chapter 5 Conclusions	93
5.1 Summary	93
5.2 Conclusions.....	96
5.3 Future Work	99
Appendix A.....	102
Appendix B.....	129
References.....	138

List of Figures

- Figure 2.1: The number of elevated thunderstorms (reports/station) identified over the 4-year period from September 1978 through August 1982. Figure taken from Colman (1990a).6
- Figure 2.2: Schematic low-level plan view diagram that summarizes the typical conditions associated with warm-season elevated thunderstorms attended by heavy rainfall. Dashed lines are representative θ_e values decreasing to the north, dashed-cross lines represent 925-850-hPa moisture convergence maxima, the shaded area is a region of maximum θ_e advection, the broad stippled arrow denotes the LLJ, the encircled X represents the MCS centroid location, and the front is indicated using standard notation. Taken from Moore et al. (2003).12
- Figure 2.3: Schematic cross-sectional view taken parallel to the LLJ across the frontal zone. Dashed lines represent typical θ_e values, the large stippled arrow represents the ascending LLJ, the thin dotted oval represents the ageostrophic direct thermal circulation associated with the low-level frontogenetical forcing. The area aloft enclosed by dotted lines indicates upper-level divergence; the area aloft enclosed by solid lines denotes location of upper-level jet streak. Note that in the cross section the horizontal distance between the MCS and the location of the upper-level jet maximum is not to scale. Taken from Moore et al. (2003).16
- Figure 2.4: a) A matrix showing the stable boundary layer used in each experiment arranged by varying inversion height and stable boundary layer potential temperature lapse rate. Temperature is in black. CIN, CAPE, and DCAPE are shown in units of J/kg. b) Normalized histogram of 4-km updraft parcel origin altitude (km) for each stable layer simulation. The matrix in b) directly corresponds to the profiles in matrix a). Taken from Nowotarski et al. (2011). ...23
- Figure 2.5: Cross section showing a range-height indicator (RHI) of radial velocity through the squall line's cold pool. Taken from Billings and Parker (2012).31
- Figure 2.6: a) Composite reflectivity data showing a line of evenly spaced elevated thunderstorms, some supercells, over southern WI at 0600 CDT 4 Oct 2006. Conventional surface data locate west-east-oriented cold front along radar fineline over northern IL. Surface-based warm sector thunderstorms are present over northern IL and northwest IN. b) Composite reflectivity data showing elevated shower and thunderstorms in short bands over southern IL at 1800 CDT 26 Mar 2008. Conventional surface data show west-east-oriented stationary front extending from southern MO into western KY. Taken from Corfidi et al. (2008).33

Figure 3.1: An example of a Z_{DR} column as selected by the algorithm used in this study; Z_{DR} shown in dB. The star represents the location of the selected Z_{DR} base. The black boxes are indicative of the maximum 3 x 3 average Z_{DR} at each 0.5 km AGL height and are thus part of the Z_{DR} column. Note: while this is based on real data, this may not actually be representative of the actual Z_{DR} column selected. The actual algorithm very well may select pixels not shown in this cross-section (they could be from neighboring cross-sections analogous to moving west or east). This image is merely for illustrative purposes.47

Figure 3.2: An example of a convergence column as selected by the algorithm used in this study; convergence (blue)/divergence (red) shown in $10^{-3} s^{-1}$. The star is located at the base of the Z_{DR} column (as in Figure 2.1). A 3 x 3 box (shown in green) centered on the Z_{DR} column base (star) is the starting location for the algorithm to extract the values and locations of the maximum convergence corresponding to the convergence column. The 4 x 3 box from which the maximum convergence is selected is shown in yellow for the 0.5 km levels both above and below the Z_{DR} column base level. At each height, the magenta box outlines the pixel of maximum convergence from within the convergence column. Note: while this is based on real data, this may not actually be representative of the actual maximum convergence values selected. The actual algorithm very well may select pixels not shown in this cross-section (they could be from neighboring cross-sections analogous to moving west or east). This image is merely for illustrative purposes.47

Figure 4.1: Surface analysis valid at 0600 UTC on 02 April 2014. Map courtesy of the Weather Prediction Center (WPC).....54

Figure 4.2: Observed upper-air sounding from Clinton, MO valid at 0400 UTC on 02 April 2014.55

Figure 4.3: Composite reflectivity of the first round of convection, including Cell 1 and 5, as observed from the (and centered upon) the Pleasant Hill, MO (KEAX) WSR-88D. Image valid at 0550 UTC 04/02/14.....57

Figure 4.4: Composite reflectivity of the second round of convection, including Cell 2, 3 and 4, as observed from the (and centered upon) the Pleasant Hill, MO (KEAX) WSR-88D. Image valid at 1020 UTC 04/02/14.....57

Figure 4.5: a) Plan view of reflectivity (dBZ) at 2 km AGL centered on IOP 1 Cell 1. Dashed arrow indicates the location of the north (N)-to-south (S) cross-sections shown in b), c) and d). b) Reflectivity (dBZ) cross-section of IOP 1 Cell 1. c) Z_{DR} (dB) cross-section of IOP 1 Cell 1. d) Convergence (blue)/divergence (red) ($10^{-3} s^{-1}$) cross-section of IOP 1 Cell 1. All valid at 0503 UTC 04/02/14.59

Figure 4.6: Average convergence with height for all times analyzed in IOP 1 Cell 1.60

Figure 4.7: a) North (N)-to-south (S) Convergence (blue)/divergence (red) (10-3 s-1) cross-section of IOP 1 Cell 2 valid at 1011 UTC 04/02/14. b) Same as a) of IOP 1 Cell 3 valid at 1011 UTC 04/02/14. c) Same as a) of IOP 1 Cell 4 valid at 1030 UTC 04/02/14. d) Same as a) of IOP 1 Cell 5 valid at 0513 UTC 04/02/14.63

Figure 4.8: a) Average convergence with height for all times analyzed in IOP 1 Cell 2. b) Average convergence with height for all times analyzed in IOP 1 Cell 3. c) Average convergence with height for all times analyzed in IOP 1 Cell 4. d) Average convergence with height for all times analyzed in IOP 1 Cell 5.....65

Figure 4.9: Observed upper-air sounding from Omaha, NE valid at 0000 UTC on 21 June 2014. Figure courtesy of the University of Wyoming.68

Figure 4.10: Surface analysis valid at 0000 UTC on 21 June 2014. Map courtesy of the Weather Prediction Center (WPC).....69

Figure 4.11: Composite reflectivity of SB 1 Cells 2, 4, and 5, respectively, as observed from (and centered upon) the Omaha, NE (KOAX) WSR-88D. Image valid at 2324 UTC 06/20/14.70

Figure 4.12: Composite reflectivity of SB 1 Cells 1, and 3, respectively, as observed from (and centered upon) the Omaha, NE (KOAX) WSR-88D. Image valid at 0224 UTC 06/21/14.70

Figure 4.13: a) Plan view of reflectivity (dBZ) at 2 km AGL centered on SB 1 Cell 1. Dashed arrow indicates the location of the north (N)-to-south (S) cross-sections shown in b), c) and d). b) Reflectivity (dBZ) cross-section of SB 1 Cell 1. c) ZDR (dB) cross-section of SB 1 Cell 1. d) Convergence (blue)/divergence (red) (10-3 s-1) cross-section of SB 1 Cell 1. All valid at 0218 UTC 06/21/14.73

Figure 4.14: Average convergence with height for all times analyzed in SB 1 Cell 1.....74

Figure 4.15: a) North (N)-to-South (S) Convergence (blue)/divergence (red) (10-3 s-1) cross-section of SB 1 Cell 2 valid at 2221 UTC 06/20/14. b) Same as a) of SB 1 Cell 3 valid at 0322 UTC 06/21/14. c) Same as a) of SB 1 Cell 4 valid at 2307 UTC 06/20/14. d) Same as a) of SB 1 Cell 5 valid at 2352 UTC 06/20/14.....75

Figure 4.16: a) Average convergence with height for all times analyzed in SB 1 Cell 2. b) Average convergence with height for all times analyzed in SB Cell 3. c) Average convergence with height for all times analyzed in IOP 1 Cell 4. d) Average convergence with height for all times analyzed in SB Cell 5.76

Figure 4.17: A box-and-whisker plot comparing 0.5 km AGL convergence from all cells analyzed in IOP 1 (elevated) to the same from all cells (with sufficient data) analyzed in SB 1 (surface-based). The box is indicative of the 25th and 75th percentiles, respectively. The 'x' marks the average value while the line near the center of the box is representative of the median value.....	80
Figure 4.18: Summary of convergence at 0.5 km AGL over the lifecycle of IOP 2 Cell 1.....	90
Figure 4.19: Radar reflectivity a 2 km AGL during the analyzed lifecycle of IOP 2 Cell 1 at a) 2029 UTC, b) 2046 UTC, c) 2103 UTC, d) 2125 UTC, and e) 2142 UTC all valid for 06/04/14.....	91

List of Tables

Table 3.1: All intense observing periods (IOPs) from the 2014-2015 Program for Research on Elevated Convection with Intense Precipitation (PRECIP) field season. Italicized IOPs were ultimately excluded from this study.	35
Table 4.1: A summary of the thermodynamic environment for the IOPs examined in this study. The values represented here are from actual observed upper-air data collected from the PRECIP field team. Italicized columns emphasize soundings with no SBCAPE. SBCAPE and MUCAPE values with an asterisk (*) are likely not representative of the actual environmental values at the indicated times. In such cases, the upper-air flight was terminated early due to flight errors of some kind and thus the sounding is not complete. Thus the actual SBCAPE and MUCAPE values in these instances are almost certainly higher.	52
Table 4.2: A summary of the 5 most intense cells based on composite reflectivity from the IOP 1 as observed from the Pleasant Hill, MO (KEAX) radar. These 5 cells were used as the basis for studying IOP 1. *Convergence values reported here are raw values.	58
Table 4.3: A summary of the 5 most intense cells based on composite reflectivity from the IOP 1 as observed from the Pleasant Hill, MO (KEAX) radar. These 5 cells were used as the basis for studying SB 1. *Convergence values reported here are raw values.	69
Table 4.4: Comparisons of the 0.5 km AGL convergence from all times in all analyzed cells from IOP 1 to the same for that of SB 1.	81
Table 4.5: Summary of the convergence column within the analyzed cells from IOP 4.	84
Table 4.6: Summary of the convergence column within the analyzed cells from IOP 5. The asterisk (*) highlights the change for this IOP of a low-level analyzed height of 1 km AGL rather than 0.5 km AGL (as in other cases) due to insufficient 0.5 km AGL data for IOP 5.	86
Table 4.7: Summary of the convergence column within the analyzed cells from IOP 2.	88
Table 4.8: Summary of the convergence column within the analyzed cells from IOP 7.	88

Abstract

Elevated convection has now been widely associated with severe hazards such as large hail and heavy rainfall, however, high winds and tornadoes are not as common (e.g., Grant 1995, Moore et al. 2003, Horgan et al. 2007). While these operational impacts of elevated convection are known, as well as the environmental conditions favorable for elevated convection (e.g., Moore et al. 2003), recent studies have called into question our understanding of how to identify convection as elevated as it seems more complex than once thought (e.g., Corfidi et al. 2008). Thus, this study seeks to gain further insight to elevated convection using dual-polarization Doppler radar, a method by which elevated convection has been studied quite rarely. Specifically, the Doppler velocity-derived convergence (divergence) product will be used to examine any differences specifically with respect to low-level convergence at the base of a convective updraft. Overall comparisons of the newly defined convergence column associated with the updraft will also be made. Both an elevated case and a surface-based case will be closely examined with the aforementioned comparisons made. The elevated case is one (IOP 1) of several intense observing periods (IOPs) which included the deployment of teams to collect upper-air data via weather balloons that are derived from the 2014 and 2015 Program for Research on Elevated Convection with Intense Precipitation (PRECIP) field campaign. Four other IOPs will also be examined with respect to the results from the elevated versus surface-based comparisons. Statistical evidence indicates that convergence is reduced in association with an elevated convective event beneath the inversion as compared to the low-levels of surface-based event. Furthermore, there are

indications that the radar-derived convergence product can be used to classify convective type on a cell-by-cell basis and that transitions of cells from one convective type to another can be observed.

Chapter 1: Introduction

Elevated convection, convection rooted above a low-level stable layer, regularly occurs over the central Plains of the United States (Colman 1990a). Such convection can pose a risk of large hail and flash flooding, however, threats of high winds and tornadoes are typically kept to a minimum (e.g., Grant 1995, Rochette and Moore 1996, Horgan et al. 2007). Several studies of elevated convection through the years have led to a fairly good understanding of the environment in which these events are too occur (e.g., Colman 1990a, Moore et al. 1998, Moore et al. 2003). Typically, elevated convective events occur just north of a synoptic front, typically a warm or stationary front (e.g., Colman 1990a, Moore et al. 2003). A strong 850-mb low-level jet (LLJ) is responsible for advecting warm-moist air over such a front, creating an inversion to the north of the boundary. A combination of isentropic ascent, lift via frontogenesis, as well as upper-level support from an upper-level jet streak, all typically allow for the lifting of parcels from, or just above, the inversion into an unstable environment (Moore et al. 2003). In such a case, though convective available potential energy (CAPE) from lifting a parcel from the surface may be zero, a parcel lifted from near the top of the inversion would have sufficient amounts of elevated or most unstable CAPE (e.g., Colman 1990a).

It has typically been accepted that if an inversion exists, and thus creates an environment with more most unstable CAPE (MUCAPE) than surface-based CAPE (SBCAPE), that convection would be primarily elevated in nature (e.g., Rochette and Moore 1996, Nowotarski et al. 2011, Schumacher 2015). However, recent studies have begun to challenge this notion. Corfidi et al. (2008) led the way by questioning whether a

simple dichotomy between elevated and surface-based convection actually exists. They furthermore suggested that convection was often likely on a spectrum between purely elevated and purely surface-based. Several modeling (Parker 2008, Nowotarski et al. 2011, Schumacher 2015) and a few observational studies (Marsham et al. 2011, Billings and Parker 2012) then went on to give support to the ideas presented in Corfidi et al. (2008), so much so, that to assume convection is elevated when some amount of SBCAPE is available is likely flawed. This seems to even be true when MUCAPE is much greater than SBCAPE due to an inversion. That is not to say that convection in such a case is absolutely surface-based, it very well might not be. What it does say is that thermodynamic profiles alone do not render us the ability to determine the convective type in such a case. Therefore, some alternative way to classify such cases should be explored.

1.1 Purpose and Objectives

In this study, National Weather Service (NWS) WSR-88D dual-pol Doppler radar data will be used to study elevated convection to see if a defining characteristic within the radar data can be associated with elevated convection. Therefore, any such defining radar characteristic could aid in the determination of convective types when thermodynamic profiles are not sufficient enough to make a determination. The identification of the convective type to any degree remains important because such a classification should then provide information into potential hazards associated with the convection, as well as factors such as longevity. The most obvious radar product thought to be useful in discriminating between elevated and surface-based convection is the Doppler velocity-derived convergence (divergence) product. It is hypothesized that low-level convergence

should be reduced in association with an elevated convective cell because inflow from the cell's updraft should not extend all the way to the surface. Inflow from a surface-based cell however, would be expected to contribute to convergence within the updraft all the way to the surface.

Thus, the objectives of this study are to:

- 1) Explore the potential use of the convergence (divergence) Doppler radar velocity-derived product to determine if convergence is decreased near the surface, and below the inversion, for elevated convection as compared to surface-based convection.
- 2) If so, can this determination be extended to identify, or at least provide evidence in favor of identifying, a convective event as either elevated or surface-based?
- 3) Moreover, could such information then be more specifically used to determine the convective mode of an individual convective cell? If this is possible, then it should also be reasonable to observe the transition of a cell from one convective type to another in such cases where this may occur.

Chapter 2: Literature Review

2.1 Elevated Convection Defined

Elevated convection was first examined in depth by Colman (1990a) though it was certainly studied previously (e.g., Means 1952, Maddox 1979, Cotton et al. 1989). The term “elevated” was used by Colman (1990a) to describe convection that is rooted above a stable boundary layer and thus would be “isolated from strong diabatic effects” due to a low-level stable layer. This type of convection would therefore be in contrast to surface-based convection which is rooted in the boundary layer and driven by the destabilization of the lower atmosphere. Colman (1990a) found that elevated thunderstorms were characteristically different than their surface-based counterparts. Primarily, elevated thunderstorms occur in regions with little-to-no positive convective available potential energy (CAPE) when lifting a parcel from the surface. This is because the surface is characterized by very stable air beneath a low-level frontal temperature inversion.

Specifically, Colman (1990a) provided this definition for convection that typically occurred in an overrunning situation in which convection developed on the cold side of a front above a low-level inversion. Corfidi et al. (2008) provide essentially the same technical definition of elevated convection, in that the parcels of such convection are ingested from above the low-level stable layer, however, they note that elevated convection can occur “above any near-surface stable layer.” Thus, this broader definition is to include the stable layer that develops at night as a result of near-surface nocturnal

cooling. Today, this broader definition (Corfidi et al. 2008) is generally implied so that elevated convection would include convection rooted above the near-surface stable layer on the cold side of a surface boundary or over a nocturnally induced inversion.

2.2 Elevated Convection Climatology

Colman (1990a) went on to offer a first look at the climatology of elevated convection. Colman's (1990a) climatology of elevated thunderstorms (based on cases from September 1978 to August 1982) was founded upon the basis that elevated convection occurs on the cold side of a front that is characterized by a clear delineation in temperature, dewpoint, and wind. Moreover, there should be a clear gradient of equivalent potential temperature (θ_e) along the front with higher θ_e values on the warm side of the front and lower θ_e values on the cold side of the boundary. Ultimately, Colman (1990a) found that almost all U.S. thunderstorms during the winter season and east of the Rockies (with the exception of Florida) are elevated in nature. The most common location, climatologically, for elevated thunderstorms to occur is over the central Plains with a maximum located over eastern Kansas (Fig. 2.1).

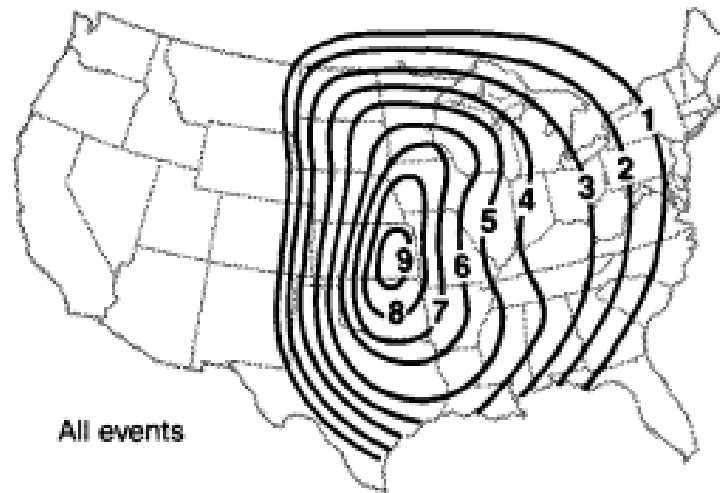


Figure 2.1: The number of elevated thunderstorms (reports/station) identified over the 4-year period from September 1978 through August 1982. Figure taken from Colman (1990a).

Elevated convection was found to vary annually with the most common occurrence between March and June (most frequent in April) with a secondary peak in September (Colman 1990a). When Horgan et al. (2007) specifically examined a 5-year climatology of severe reports from elevated convection, they found a nearly identical seasonal cycle to Colman (1990a), with the most severe reports in May and a secondary peak in September. Colman (1990a) went on to also suggest that there was a diurnal variation in the occurrence of elevated convection with respect to the type of front present, though this was based on only using observations from 0000 UTC and 1200 UTC. He found that elevated thunderstorms were more likely to occur at 1200 UTC north of a warm or stationary front, however, they would be more likely to occur at 0000 UTC north of a cold front. Horgan et al. (2007) found a broad afternoon peak (1800 – 0100 UTC) in the initial severe reports from elevated convection. This should not be considered to refute the results of Colman (1990a), but rather might be better interpreted

that severe weather is most likely during the early stages of potentially elevated thunderstorms that continue overnight (e.g., Fritsch and Forbes 2001).

As a part of an extensive field project, the International H₂O Project (IHOP_2002), Wilson and Roberts (2006) examined the initiation and evolution of convection over the defined study area. Their study concluded that there was a “common occurrence of nocturnal initiation of elevated storms” over the central-southern Great Plains, which generally agrees with the climatologically expected regions for elevated convection (Colman 1990a). An area of thunderstorm initiation was deemed as elevated if there was no surface convergence features identified in their study. Thus, Wilson and Roberts (2006) used surface convergence as a proxy for identifying convection that was rooted in surface air. Overall, Wilson and Roberts (2006) found that most nocturnal initiated thunderstorms were elevated in nature. This further supports the notion of diurnal variations in the occurrence of elevated convection as suggested by Colman (1990a).

Colman (1990a) further examined the spatial climatology of elevated thunderstorms with respect to the surface low and surface front. He found that the greatest frequency of such elevated thunderstorms occurs in an area just north of the surface low that extends eastward a little more than 500 km. This eastward extension would coordinate to the area along the cold side of a front. Colman (1990a) further showed that most of the cases of elevated convection examined occurred on the cold side of a warm front (49%) or a stationary front (29%), while generally fewer events occurred on the cold side of a cold front (23%).

Colman (1990a) found that the median distance that elevated thunderstorms occurred from the associated front was around 200 km into the cold sector. Grant (1995) found, within his 11 cases which resulted in severe reports from elevated convection, that the initial severe report was on average 230 km north of either a warm or stationary front. In a study of 21 warm-season elevated thunderstorm events which produced heavy rainfall, Moore et al. (2003) found that the elevated mesoscale convective system (MCS) centroid was on average 160 km north of a west-to-east boundary. While these distances vary somewhat from those found by Colman (1990a), the three studies reasonably agree, especially when considering that the range of the elevated MCS centroids in Moore et al. (2003) varied from 40 km to 425 km.

2.3 Thermodynamic Environment of Elevated Convection

As previously mentioned as a defining characteristic of elevated convection, the near-surface layer is characterized by an inversion which typically stabilizes the layer with respect to convective measurements such as CAPE or the lifted-index (LI) (Colman 1990a). However, positive CAPE was found in representative soundings in several of the aforementioned studies (Grant 1995, Rochette and Moore 1996, Moore et al. 1998) when lifting a parcel from the point at which the highest θ_e occurred. In fact, in the Moore et al. (1998) heavy rainfall cases, 1793 J/kg of “elevated CAPE” existed in a representative sounding when lifting a parcel from the level of the highest θ_e . Meanwhile, no CAPE was present when lifting the mean parcel from the lowest 100 hPa of the sounding (i.e. the near-surface). A similar sounding was presented in Grant (1995) and while the sounding from the Rochette and Moore (1996) case study did find significant amounts of CAPE

even when lifting the parcel from near the surface, the amount of CAPE significantly increased when lifting the parcel from its most unstable point.

Rochette and Moore (1996) concluded that, in general, “the mean low-level parcel CAPE does not truly represent the instability of the environment” with respect to elevated convection given that the synoptic scale lifting occurs above the low-level stable planetary boundary layer (PBL). Rochette et al. (1999) went on to explicitly point out the need to examine CAPE and CIN with respect to lifting a parcel from the level of the highest θ_e in order to best assess the potential for elevated convection that may result in heavy rainfall (Rochette and Moore 1996, Moore et al. 1998) or severe weather such as large hail (Grant 1995, Horgan et al. 2007). Moore et al. (2003) provided more support that such near-surface indices were not indicative of the available elevated convective instability when the composite of each of their 21 cases found that near-surface CAPE indicated around 600 J/kg of energy available. However, the highest θ_e CAPE was around 1250 J/kg at the MCS centroid for these same cases. Moore et al. (2003) went on to stress the importance of also examining the highest θ_e convective inhibition (CIN) as it revealed a local decrease near the MCS centroid.

2.4 Synoptic Conditions for Elevated Convection

Moore et al. (2003) performed a composite analysis of 21 warm-season excessive rainfall (> 5 in.) events that were associated with elevated MCSs. In relation to the upper-level synoptic conditions, Moore et al. (2003) found that the elevated MCS was generally located within the right-entrance region of a slightly anticyclonically curved 250-hPa jet streak. This is an area which has been determined to be a favored region of divergence

aloft and thus could enhance low-level convergence and lift (Moore and VanKnowe 1992). This finding corroborates earlier findings from Junker et al. (1999) in a study of heavy rain producing MCSs (though not necessarily elevated) in which the heaviest rainfall occurred within an area of 250-hPa divergence.

Furthermore, Moore et al. (2003) found that most elevated convection occurs near the mid-level inflection point between anticyclonic and cyclonic flow. Colman (1990a) suggested the same in his climatology of elevated thunderstorms but added that 40% of the cases occurred downstream of the inflection point. Therefore, elevated convection can occur within a region of slight mid-level ridging. Moore et al. (2003) did note an approaching mid-level shortwave in the composite of all 21 cases, but also stated that most of the cases exhibited neutral to weakly positive vorticity within the mid-levels. Junker et al. (1999) also found that many of the heavy rainfall cases in his study were not necessarily associated with upper- or mid-level positive vorticity advection, but rather were connected to 850-hPa warm-air advection.

Moore et al. (2003) went on to conclude that given a lack of forcing from vorticity advection, low-level warm-air advection and isentropic upglide must play a large role in producing vertical motion for such events. Indeed, the low-levels have garnished the most attention with regards to the conditions favorable for elevated convection. In the work in which Colman (1990a) originally discusses elevated thunderstorms, he also noted the low-level environment in which they tended to form. This included the observation that elevated thunderstorms were most frequently located downstream of the 850-hPa trough near a region of horizontal-wind deformation within the left-exit region of the LLJ. This environment is further characterized by warm-air advection (Colman 1990a).

There is no shortage of research supporting the important role of the LLJ and associated warm-air advection with respect to either organized nocturnal convection, much of which has been assumed to be elevated (Maddox et al. 1979, Trier and Parsons 1993, Augustine and Caracena 1994), or was specifically described as elevated convection (Colman 1990b, Grant 1995, Rochette and Moore 1996, Moore et al. 1998, Moore et al. 2003). Trier and Parsons (1993) heavily emphasized the role the LLJ had in advecting moist, unstable air within the region of a potentially elevated mesoscale convective complex (MCC). Grant (1995) found that the LLJ extended at least 160 to 300 km on the cold side of the front, which corresponds to the most frequent location of elevated convection with respect to the surface front (Colman 1990a, Grant 1995, Moore et al. 2003).

Moore et al. (2003) concluded from their composite analyses that the LLJ is oriented almost normal to the low-level thermal and moisture gradients (Fig. 2.2) and therefore results in substantial advection of these fields, and aids as forcing located above the PBL. Their composite map of 850-hPa θ_e advection reveals a large area of positive θ_e advection nearly collocated with the elevated MCS location. Moore et al. (2003) went on to state that such “advection of higher θ_e air is critical in the destabilization process by promoting elevated convective instability above the surface boundary.” Overall, several of the aforementioned studies (Colman 1990a,b, Grant 1995, Rochette and Moore 1996, Moore et al. 1998) pointed to the idea that the LLJ, located around the 850-hPa level, is an important factor in advecting warm/high θ_e air over the stable boundary layer. Indeed, the same studies commonly found that the highest θ_e air occurred around 850-hPa with an area of elevated instability located above this level.

Below 850-hPa, the environment is characterized by a low-level stable layer due to a very shallow frontal temperature inversion (e.g. Colman 1990a, Grant 1995, Moore et al. 1998, Fritsch and Forbes 2001). As already alluded to, this low-level stable layer is largely the result of southerly warm-air advection near 850-hPa, meanwhile, the near-surface layer is much cooler and drier with winds usually having an easterly component (Colman 1990a). This creates a substantial amount of both speed and directional shear within the near-surface to 850-hPa layer (Colman 1990a, Grant 1995).

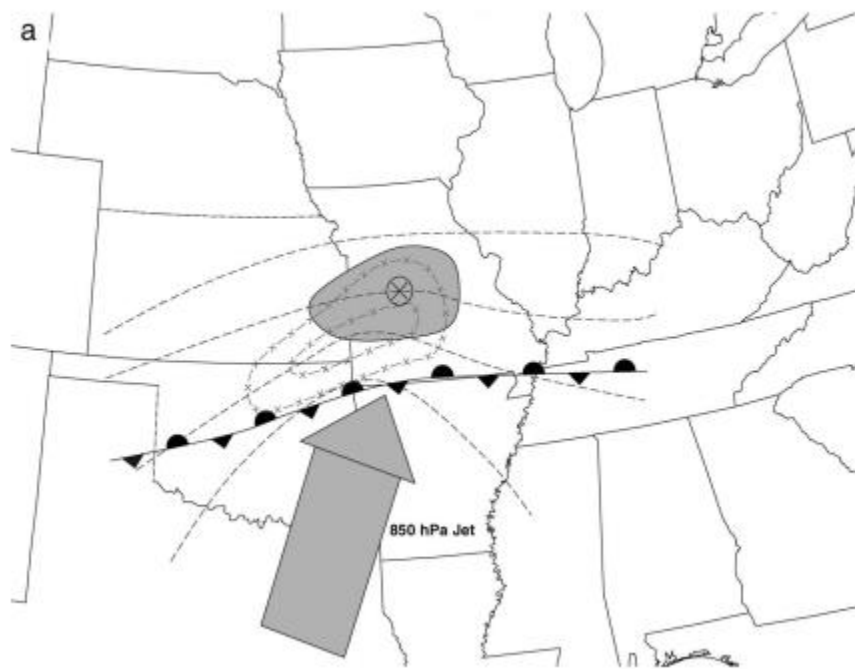


Figure 2.2: Schematic low-level plan view diagram that summarizes the typical conditions associated with warm-season elevated thunderstorms attended by heavy rainfall. Dashed lines are representative θ_e values decreasing to the north, dashed-cross lines represent 925-850-hPa moisture convergence maxima, the shaded area is a region of maximum θ_e advection, the broad stippled arrow denotes the LLJ, the encircled X represents the MCS centroid location, and the front is indicated using standard notation. Taken from Moore et al. (2003).

2.5 Lifting Mechanisms of Elevated Convection

With seemingly no instability for a near-surface based parcel (e.g., Colman 1990a, Moore et al. 1998), or substantial amounts of CIN to overcome (e.g., Rochette and Moore 1996), it is inherent that the forcing mechanism be examined for cases in which elevated thunderstorms occur. In an extended look at several of the individual cases within the elevated thunderstorm climatology (Colman 1990a), Colman (1990b) determined that the best explanation for the development of thunderstorms in an environment with no CAPE was slantwise convection. Slantwise convection would most likely either be forced by moist symmetric instability or by frontogenetical circulations, based on the idea of local conditional symmetric instability as described by Emanuel (1983).

In one particular case upon which Colman (1990b) focused, he found that the air was unstable with respect to slantwise displacement, up to a point at which it potentially developed into upright convection. In general however, Colman (1990b) concluded that the majority of elevated thunderstorms are not the result of upright convection. Williams (1991) was quick to challenge this idea though, claiming that, while the “feeder air” for convection does indeed not originate from below the frontal surface (Colman 1990a), that the more traditional understanding of conditional instability (as opposed to symmetric) be more rigorously examined. Moore et al. (1998) also challenged the notion that most elevated convection was not upright (Colman 1990b) when their work examined two cases of upright elevated convection. Moreover, while neither Grant (1995) nor Rochette and Moore (1996) explicitly examined the role of upright versus slantwise convection with respect to their studies of elevated convection, they both inferred the existence of

upright convection when considering that parcels could be lifted from above the frontal inversion into a region of elevated convective instability (Moore et al. 1998).

Moore et al. (1998) determined that lift, via isentropic upglide, was enough in both cases examined therein to lift a parcel to its level of free convection (LFC). This would then allow for the areas of analyzed elevated CAPE to be realized which, in turn, would allow upright convection to occur. While Moore et al. (1998) did consider slantwise convection to be a potential factor in these cases of elevated convection, they determined, in opposition to Colman (1990b), that it likely plays a lesser role when compared to upright convection. Certainly the idea of isentropic upglide/warm-air advection providing substantial lifting is supported by other studies (Rochette and Moore 1996, Junker et al. 1999, Moore et al. 2003).

In their analysis of elevated convection during the IHOP_2002 project, Wilson and Roberts (2006) used upper-level Rapid Update Cycle (RUC) model analysis in order to take a closer look at the initiation of the elevated nocturnal thunderstorms. They found that two-thirds of the elevated thunderstorm initiation cases had convergent or confluent wind patterns between 900 and 600 hPa within areas of mid-level instability. While Wilson and Roberts (2006) provide little description of the meteorological factors for such an area of wind convergence, it seems reasonable to assume that at least some of the cases were related to horizontal wind deformation near the terminus of the LLJ (Colman 1990a). As aforementioned, there are numerous studies emphasizing the important role that the LLJ seems to play in organizing elevated convection (e.g., Trier and Parsons 1993, Grant 1995, Moore et al. 2003).

Meanwhile, Augustine and Caracena (1994) concluded that frontogenesis plays a significant role in forcing large MCSs. While Augustine and Caracena (1994) did not explicitly examine elevated MCSs, their results are suggestive of MCSs located on the cold side of a frontal boundary over a low-level inversion, and thus are likely elevated MCSs. Moore et al. (2003) also went on to conclude that frontogenesis likely enhances forcing that leads to elevated MCSs, and indeed found that positive values of frontogenesis occurred with over 80% of times and heights (both 850-hPa and 925-hPa) evaluated in their study. Ultimately, Moore et al. (2003) provided a schematic cross-sectional view taken normal to the surface front which summarizes the roles of the LLJ, isentropic upglide, and frontogenetical and upper-level jet circulation forcings in the development of an elevated MCS over a cool, stable air mass (Fig. 2.3). This study was the first to concisely describe the role that each of these factors seem to contribute to the development of elevated thunderstorms.

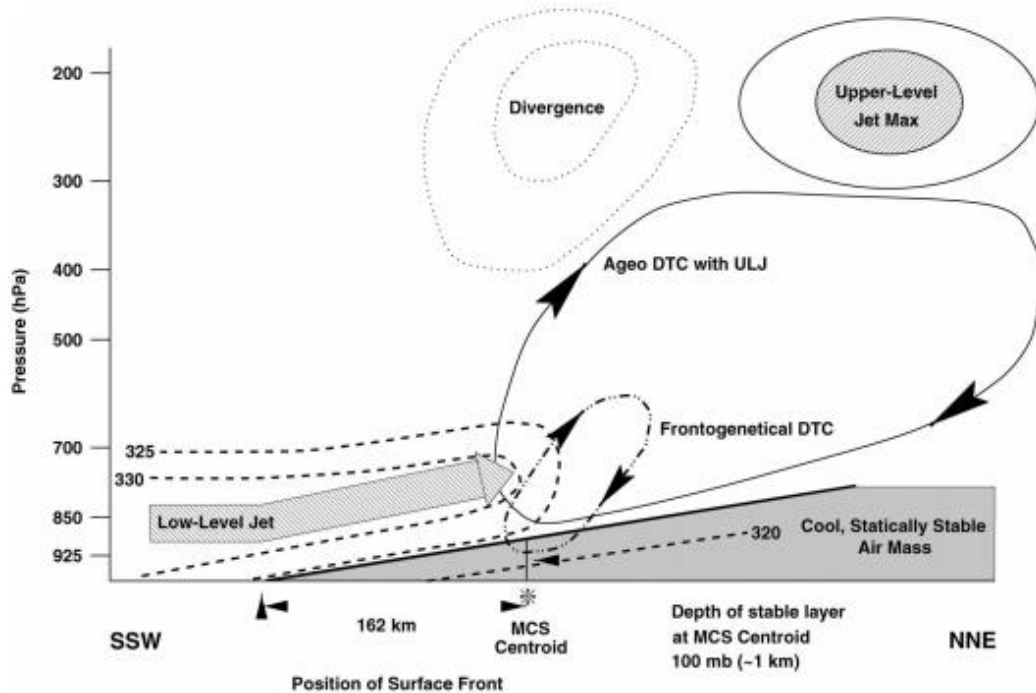


Figure 2.3: Schematic cross-sectional view taken parallel to the LLJ across the frontal zone. Dashed lines represent typical θ_e values, the large stippled arrow represents the ascending LLJ, the thin dotted oval represents the ageostrophic direct thermal circulation associated with the low-level frontogenetical forcing. The area aloft enclosed by dotted lines indicates upper-level divergence; the area aloft enclosed by solid lines denotes location of upper-level jet streak. Note that in the cross section the horizontal distance between the MCS and the location of the upper-level jet maximum is not to scale. Taken from Moore et al. (2003).

2.6 Severe Hazards Related to Elevated Convection

Grant (1995) was the first to study the severe weather hazards associated specifically with elevated convection as termed by Colman (1990a). Grant (1995) studied 11 cases of elevated convection between April 1992 and April 1994 which had associated severe weather reports. His results indicated that the most typical severe weather reported with elevated convection was large hail (92% of reports). There were far fewer severe wind (7%) and tornado (1%) reports. Horgan et al. (2007) expanded upon the work of Grant (1995) by extending the climatology to a 5 year study which, as a result, included several more cases (129 compared to 11 in Grant 1995). While Horgan et al. (2007) agreed with Grant (1995) that large hail was the most common severe weather report in

association with elevated thunderstorms, there were considerably more severe wind reports (37%) and slightly more tornado reports (4%) in his study. Horgan et al. (2007) did go on to note that significant wind and tornado reports (as defined by the Storm Prediction Center) were clearly less likely in association with elevated convection than with surface-based convection, while significant hail reports were about the same for both convective types.

In a study on MCSs, Fritsch and Forbes (2001) noted that due to the low-level stable layer, moist downdrafts in association with these elevated MCSs do not reach the surface. This not only limits the development of a convectively induced cold pool, but it also results in a lesser likelihood of severe hazards such as high winds and tornadoes in association with MCSs. Obviously, this is supported by other studies and serves to explain a reduction of these severe hazards with elevated convection (Grant 1995, Horgan et al. 2007). Trier and Parsons (1993) furthermore used surface observations from near the center of an MCS to find that the downdrafts were unable to penetrate the low-level stable layer as suggested by Fritsch and Forbes (2001).

In a modeling study of supercells over a low-level stable layer, Nowotarski et al. (2011) found that downdrafts are actually able to penetrate low-level stable layers, though weakened. Furthermore, they stated that the “near-surface circulation is reduced in simulations of supercells situated over stably stratified layers, whether or not the updraft is able to lift the stable low-level air.” Both of these are important findings with respect to potential severe weather in the form of high winds or tornadoes. Basically, such findings support the overall climatology of severe weather associated with elevated convection (Grant 1995, Horgan et al. 2007), in that while high winds or tornadic

circulations could reach the surface, the occurrence is generally reduced. Thompson et al. (2007) further substantiates a reduction, but not the impossibility of tornadoes with elevated thunderstorms (Grant 1995, Horgan et al. 2007, Corfidi et al. 2008) when they found that 10 of the 280 weakly tornadic cases in their dataset had an effective inflow layer base above the ground (i.e., were elevated).

Elevated MCSs have also been studied in relation to their heavy rain production (e.g. Rochette and Moore 1996, Moore et al. 2003). Maddox et al. (1979) outlined what they deemed a “frontal” type flash flood event in which unstable air was advected over a surface front (typically west-to-east) with heavy rainfall occurring on the cool side of the front. In other words, Maddox et al. (1979) noted that flash flooding often occurred as a result of elevated convection just north of a surface front. Rochette and Moore (1996) found a similar setup to that outlined by Maddox et al. (1979) for a case of elevated convection that did produce flash flooding over Missouri. Moreover, Moore et al. (2003) found 21 cases where elevated MCSs produced heavy rainfall in excess of five inches over a five year period during the warm season which certainly speaks to its commonality.

2.7 An Insufficient Understating of Elevated Convection

As previously noted, Corfidi et al. (2008) extended the definition of elevated convection to include all forms of convection where the air parcels originate above any near-surface stable layer. Thus, elevated thunderstorms may not only necessarily be on the cool side of a surface boundary as first described by Colman (1990a), but storms could also be elevated above a stable nocturnal inversion.

Corfidi et al. (2008) went on to challenge the understanding of elevated convection in general, as they noted that air from a near-surface stable layer can still be incorporated into updrafts if the resulting parcels can become positively buoyant. They questioned what is to be considered “mainly” with respect to surface-based convection being rooted “mainly” in the PBL, and pointed out that two seemingly identical “surface-based storms” could have differing levels of most unstable inflow. Thus, Corfidi et al. (2008) deemed that “the widely accepted notion that a simple dichotomy exists between surface-based and elevated storms” be reconsidered. Corfidi et al. (2008) substantiated their claims using the work of Coniglio et al. (2007) as an example of the indistinct line between what is surface-based and elevated convection and ultimately stated that to classify convection explicitly as either surface-based or elevated is beyond the current knowledge of convective processes. They further concluded that a continuum from purely surface-based to purely elevated convection likely exists.

Moreover, Corfidi et al. (2008) went on to clearly indicate a deficiency in the overall understanding of elevated convection and the forecasting challenges that accompany such a lack of knowledge. They noted insufficient clarity between the overall characteristics as well as the morphology of elevated storms as compared to surface-based storms. They also discussed the forecasting challenges associated with the transition from either elevated to surface-based convection or vice versa. Such challenges included potential severe weather forecasting given the fact that elevated thunderstorms are less likely to produce hazards such as high winds and tornadoes (Grant 1995, Horgan et al. 2007). Even then, Corfidi et al. (2008) brought to light questions regarding why

some seemingly elevated thunderstorms do indeed produce high winds or tornadoes while most do not.

2.7.1 Modeling Evidence for Redefining Elevated Convection

In a modeling study considering the effect of nocturnal cooling on a squall-line, Parker (2008) discovered key results in favor of the notion provided by Corfidi et al. (2008). The model simulations most accurately depict convection that is initially surface-based but then transitions to elevated due to nocturnal cooling near the surface as opposed to the development of an inversion north of a synoptic front. Nevertheless, Parker (2008) provided evidence that cold-pool driven convection, regardless of other synoptic factors, can overcome considerable stabilization in the near-surface environment so long as there is some amount of near-surface CAPE remaining. Typically, convection in an environment with considerable amounts of CIN and higher most-unstable CAPE than near-surface CAPE (both due to a low-level inversion) would have been considered to be elevated (e.g., Rochette and Moore 1998, Moore et al. 2003).

Seeing that convection was able to maintain surface interactions, Parker (2008) went on to conclude that many nocturnal convective systems that were before considered to be elevated may be surface-based. Parker (2008) further found that in order for the simulated convective system to remain surface based, both near-surface CAPE and deep cold pool lifting need to be present. They also noted that deep lifting may actually occur best with weaker cold pools. Once the simulated convection transitioned into what Parker (2008) deemed the “elevated stage,” which nearly corresponds to the time at which near-

surface parcels no longer had any CAPE, the near-surface air in the stable layer passed mainly beneath the system without being lifted into the convective updrafts.

It is worth noting that one of the simulations by Parker (2008) resulted in a convective system that was “right on the threshold between being surface based and elevated” which seems, in particular, to support the idea that there is a continuum between surface-based and elevated convection as concluded by Corfidi et al. (2008).

Nowotarski et al. (2011) specifically examined the role of low-level static stability on presumably elevated supercells using a three-dimensional modeling study. Their study varies from many other modeling studies (e.g., Parker 2008, Schumacher 2015) given a focus on specifically supercell thunderstorms as opposed to some variation of convective complex (MCS or squall-line). Given a focus on presumably elevated supercells, this study carries potential operational implications since tornadoes occur much less frequently from elevated thunderstorms (Grant 1995, Horgan et al. 2007). Nowotarski et al. (2011) used a control simulation with surface-based CAPE of 2096 J/kg and surface-based CIN of 41 J/kg. Furthermore, each simulation used the same wind profile so as to isolate the effects of the low-level stability on the simulated supercells in each run. Nowotarski et al. (2011) performed a number of different simulations ranging from the described control simulation (the least stable) to a simulation with a very strong low-level inversion and no surface-based CAPE (Fig. 2.4a). In each simulation, only the low-level stability profile was altered, just as in Parker (2008), so that the most unstable CAPE (2456 J/kg) remained the same in each simulation.

Using trajectories traced backwards from the mid-levels of the updraft, Nowotarski et al. (2011) found that most of the supercells in the simulations had parcels that originated in the near-surface environment and thus were not purely elevated (Fig. 2.4b). Only four of the simulations had no trajectories that led to the immediate near-surface environment and three of these four simulations had surface-based CAPE of either 1 or 0 J/kg (the fourth case had surface-based CAPE of 1171 J/kg). They further noted that in one of the simulations that had no surface-based CAPE, it remained possible for convection to ingest air from within the top of the low-level stable layer. In the end, they concluded that the ability of the updrafts in the supercell simulations to overcome the stable boundary layer was likely the result of dynamic vertical perturbation pressure gradient force (VPPGF). As a result of finding that many of the simulations continued to draw in near-surface air despite strong surface-based CIN and a much more unstable elevated environment, Nowotarski et al. (2011) went on to explicitly support Corfidi et al. (2008). Nowotarski et al. (2011) stated that “it generally would be difficult to assess the degree of elevation, especially when surface-based CAPE exists despite the presence of substantial CIN.”

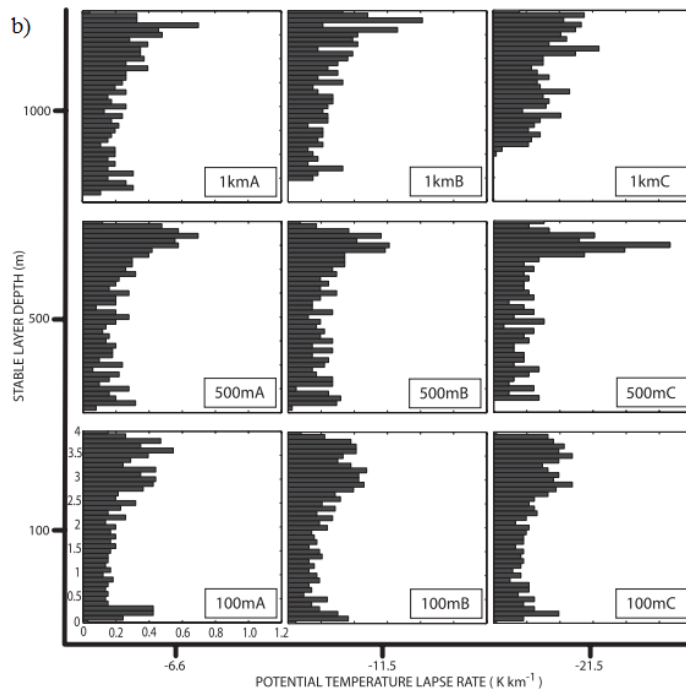
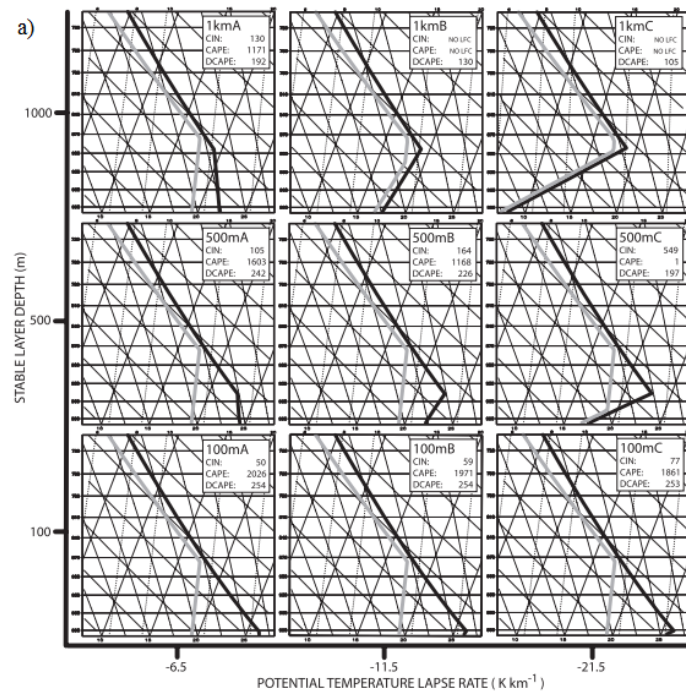


Figure 2.4: a) A matrix showing the stable boundary layer used in each experiment arranged by varying inversion height and stable boundary layer potential temperature lapse rate. Temperature is in black. CIN, CAPE, and DCAPE are shown in units of J/kg. b) Normalized histogram of 4-km updraft parcel origin altitude (km) for each stable layer simulation. The matrix in b) directly corresponds to the profiles in matrix a). Taken from Nowotarski et al. (2011).

Schumacher (2015) also performed model simulations of seemingly elevated convective systems in order to best understand the role that low-level moisture changes have on the precipitation accumulation from the convection. In the end, his results found that lesser total accumulation of precipitation in cases of drier air near the surface (as compared to the control run) was predominately a result of changes in low-level CAPE as opposed to increased low-level evaporation (though some increased low-level evaporation was indeed found in the early stages of the simulated convective systems).

This result was apparently unexpected given that the simulated convection was thought to be elevated and in each simulation only the low-levels were altered which left values of most unstable CAPE unchanged. However, Schumacher (2015) ultimately found that even though near-surface CAPE was not extremely significant (ranging from 113 – 618 J/kg with 61-162 J/kg of CIN), especially compared to most unstable CAPE (1200 J/kg), that parcels in the simulations were still being lifted from the near-surface stable layer as was the case in Parker (2008) and Nowotarski et al. (2011). Tracers placed within both the low-level stable layer and at a level just above this layer (between 1 and 2.5 km) indicated that the simulated convection was predominately elevated but that considerable near-surface air was being ingested into updrafts to the point that a change in near-surface CAPE altered the overall rainfall accumulation.

2.7.2 Observational Evidence for Redefining Elevated Convection

Parker (2008), Nowotarski et al. (2011) and Schumacher (2015) found support of an altered understanding of elevated versus surface-based convection in accordance with Corfidi et al. (2008) using strictly modeling studies. To add to these studies, Marsham et

al. (2011) used an observational approach while Billings and Parker (2012) used both modeling and observations to substantiate the findings of Corfidi et al. (2008).

Marsham et al. (2011) observed the transition from an elevated MCS to a surface-based MCS. During the transition period, they found that even when near-surface air was likely being lifted to its LFC, that most unstable CAPE remained more substantial than surface-based CAPE. Thus, even though surface-based CAPE eventually dominated, it seems there was a period where convection was neither purely elevated nor purely surface-based as suggested by Corfidi et al. (2008).

Meanwhile, Billings and Parker (2012) examined nocturnal convection over the central Plains during the Bow Echo and Mesoscale Convective Vortex Experiment (BAMEX). In the particular event examined, surface-based thunderstorms initiated during the evening hours and continued overnight even as the boundary layer became stable due to nocturnal cooling. Tornadoes were even reported with supercells well after sunset which would suggest they remained at least somewhat surface-based given that tornadoes seldom occur from elevated thunderstorms (Grant 1995, Horgan et al. 2007, Nowotarski et al. 2011).

Through observations, including dropsondes, surface station data, and even radar observations, Billings and Parker (2012) deemed that the squall line in this case remained cold pool driven and surface-based during the overnight hours. They went on to perform model simulations that also suggested the squall line remained surface-based. While Billings and Parker (2012) admitted it was difficult to determine through the available observations whether a separate area of northeastward moving supercells were surface-

based, their model simulations led them to believe that they too remained surface-based throughout much of the night. They stated that these supercells likely maintained surface influences due to the VPPGF as also concluded by Nowotarski et al. (2011).

2.7.3 Summary of a Refined Understanding of Elevated Convection

In light of the results from the recent modeling (Parker 2008, Nowotarski et al. 2011, Billings and Parker 2012, Schumacher 2015) and observational studies (Marshall et al. 2011, Billings and Parker 2012), when some amount of near-surface CAPE is available, despite much higher amounts of elevated or most unstable CAPE, there is often still some degree of surface air contributing to the convection. Thus, the convection is not purely elevated (Corfidi et al. 2008).

In fact, based on these studies, it seems safer to assume that if some amount of near-surface CAPE is available, even with relatively high amounts of surface-based CIN (Parker 2008, Schumacher 2015), that the convection is likely to some degree surface-based. That is not to say that convection might not be dominated by elevated convection, which did seem to be the case in the parcel tracer results of Nowotarski et al. (2011) and Schumacher (2015). But, given that elevated convection is defined by not having any surface parcel influence (Colman 1990a, Corfidi et al. 2008), it seems only safe to consider convection elevated when no surface-based CAPE is present (Nowotarski et al. 2011). Certainly, convection can be elevated even when near-surface parcels have positive CAPE, as suggested by Nowotarski et al. (2011) in the case that had 1171 J/kg of surface-based CAPE but no surface parcels were ingested in the tracer results, though this seems to be the exception. Thus, a better way of assessing whether convection is elevated

is needed in situations where there are appreciable amounts of surface-based CIN due to a low-level inversion yet some near-surface CAPE remains.

2.7.4 The Effective Inflow Layer

Thompson et al. (2007) made a first attempt to better define the “effective inflow layer” of a particular thunderstorm in order to more accurately portray parameters such as storm relative helicity or bulk shear, parameters which are typically based on arbitrary defined levels (i.e. 0-6 km). Thompson et al. (2007) particularly noted that this could benefit such parameters with respect to elevated thunderstorms. In fact, they specifically give an example of a representative sounding for an elevated supercell that exhibits no surface-based CAPE but has over 1300 J/kg of most unstable CAPE. Thompson et al. (2007) defined the effective inflow base as occurring where a lifted parcel would first have greater than 100 J/kg of CAPE and less than -250 J/kg of CIN. The effective inflow layer would then continue at each successive higher level until these constraints were not met.

In the aforementioned example, Thompson et al. (2007) found the effective inflow based for this elevated supercell to be at 900 hPa or 699 m AGL. They noted that an obviously elevated supercell environment could be defined by having a representative sounding with an effective inflow based above the ground. Thus, this method described by Thompson et al. (2007) seems to provide a reasonable way of better assessing whether convection is truly elevated or has some surface influences. Indeed, they did go on to state that there are some cases that can be considered as “somewhat elevated” when the most unstable parcel is lifted from a level above the surface, but the effective inflow base

extends to the surface. Again, this seems to agree with the previously mentioned idea of a continuum from purely surface-based to purely elevated convection as presented by Corfidi et al. (2008). Furthermore, using such an approach would likely do well to better understand when convection is truly elevated or has some surface-based influences.

2.8 Radar Observations of Elevated Convection

Radar has been used widely as a research tool for meteorologists, particularly as means to research thunderstorms to various degrees (e.g., Byers and Braham 1948, Brandes 1977, Wakimoto 1982, Houze et al. 1989, Bluestein et al. 1995, Przybylinski 1995). However, in comparison to thunderstorms in general, elevated thunderstorms have been researched using radar much less, especially since elevated convective studies in general were lacking until Colman (1990a) led the charge with his study on the topic.

2.8.1 Intensity Considerations

Smull and Augustine (1993) were one of the earliest to make any noteworthy examinations of the characteristics of elevated convection using radar. They noted in their examination of an MCC, that the convective updrafts in the elevated portion of the MCC were less intense than those in the seemingly surface-based portion of the MCC based on reflectivity. Otherwise, using radar as a tool to study the characteristics of elevated convection was fairly limited in many of the early studies of elevated convection.

In a transition event from elevated convection to surface-based convection, Marsham et al. (2011) used mesonet and radiosonde data to determine that the squall-line likely became surface-based by 1530 UTC, a time at which reflectivities generally

increased. Therefore, this would tend to support an idea that elevated convection may, in general, be less intense than surface-based convection in an otherwise similar environment, as first suggested in the results of Smull and Augustine (1993).

2.8.2 Gust Fronts and Cold-Pools

After Smull and Augustine (1993), it really was not until a study by Wilson and Roberts (2006) on convection within the IHOP_2002 project that any further insight was gained on the characteristics of specifically elevated convection using radar. Wilson and Roberts (2006) found that the median lifespan of elevated thunderstorm clusters was about 4 hours, which was noticeably less than the surface-based thunderstorm clusters within the same study. Wilson and Roberts (2006) speculate that this difference owes itself largely to the finding that only 31% of the elevated thunderstorm clusters produced an observable gust front. Those elevated cases that did have observable gust fronts all had lifespans of greater than 4 hours and some over 8 hours. The lack of a gust front noted in Wilson and Roberts (2006) with the clusters of elevated thunderstorms is almost certainly a direct result of the difficulty that elevated convection has in penetrating the surface-stable layer (e.g. Trier and Parsons 1993, Fritsch and Forbes 2001).

Marsham et al. (2011) went on to also closely examine one of the elevated cases from IHOP_2002, which was defined by four separate thunderstorm initiation clusters that merged and eventually transitioned into a surface-based squall line. Marsham et al. (2011) first noted that, in comparison to surface-based convection, it is more difficult for the downdrafts of elevated convection to create cold-pool outflow, which is in general agreement with previous studies (e.g. Trier and Parsons 1993, Fritsch and Forbes 2001).

In the particular MCS studied by Marsham et al. (2011) however, a cold-pool outflow did eventually form. Using radiosonde and surface mesonet data, they estimated that this MCS became surface-based once the cold-pool developed and was thus able to lift surface air to its LFC. In the end, Marsham et al. (2011) questioned how many of the longer living elevated thunderstorm episodes from Wilson and Roberts (2006), which had observable gust fronts, had near-surface air contributing to the updrafts.

Marsham et al. (2011) also used radar to observe a deepening cold pool over time as the thunderstorms became a surface-based squall line. Between 1253 UTC and 1424 UTC, the radar observed northerly ground-relative winds, thought to correspond to the cold pool, increased from a depth of 0.75 km to nearly 2 km. Thus, it is reasonable to assume that Marsham et al. (2011) provide a record of the first radar observations of convection transitioning from elevated to surface-based.

Radar observations of nocturnal supercells and an MCS during BAMEX were examined by Billings and Parker (2012). In particular, they used radar to help determine whether the convection was elevated or surface-based. Such a task required an examination of the lowest 1 km AGL. In their examination of the nocturnal squall line, many observations, including radar velocities, led them to believe the squall line was ingesting near-surface air as a result of lifting from the thunderstorm generated cold pool. Indeed, the Doppler velocity observed outflow from the storms was around 2-2.5 km deep which corresponds with the height of the LFC when lifting a parcel from the surface (Fig. 2.5). The modeling simulations of this event from Billings and Parker (2012) seemed to also indicate that the thunderstorms were indeed surface-based, and thus, such radar observations do not give us insight to the radar characteristics of elevated

thunderstorms. Nevertheless, they do provide an interesting perspective of radar velocities in a squall-line originally thought to be elevated but was in actuality likely surface-based.

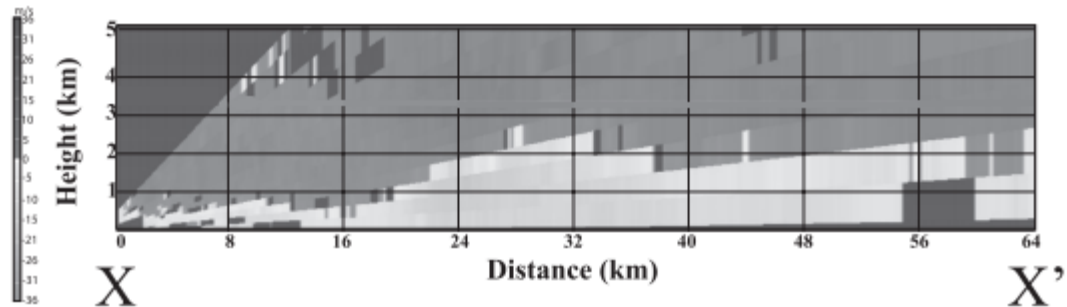


Figure 2.5: Cross section showing a range-height indicator (RHI) of radial velocity through the squall line's cold pool. Taken from Billings and Parker (2012).

2.8.3 Observed Wave-like Features

Marsham et al. (2011) provided several detailed looks at the elevated convective episodes using reconstructed range-height indicators (RHIs). They found that one of the elevated clusters seemed to initiate near the intersection of a southeastward-propagating gravity wave and a convergence line. The wave-like feature can be seen in a reconstructed RHI of reflectivity. Indeed, Marsham et al. (2011) examined the amplitude of the wave observed via radar and found that it was such that parcels could be lifted to their LFC so that the region of most unstable CAPE could be accessed. In association with a separate cluster of elevated thunderstorms associated with the same event, Marsham et al. (2011) found banded wave structures in the Doppler winds ahead of the elevated convection. They stated that these waves are likely bores resulting from the downdrafts as they meet the low-level stable layer. These bores eventually initiated more convection.

Corfidi et al. (2008) also made some general observations about the radar characteristics of elevated thunderstorms. They observed that elevated thunderstorms which occur in regions of strong warm air advection near a front sometimes form in regularly spaced lines that are somewhat parallel to the isentropic surfaces. Yet they also observed elevated storms which occur in short bands somewhat perpendicular to the isentropic surfaces in other cases. Corfidi et al. (2008) went on to state that there appears to be some arrangement in the spacing between some of the observed areas of elevated thunderstorms (Fig. 2.6), though such spacings often vary between systems and even with time during the same system. The reasoning for such arrangements to occur at times within elevated convection was concluded to be unknown by Corfidi et al. (2008) but it is reasonable to assume that a series of gravity waves or bores as observed in later studies of elevated convection could be a factor (Marshall et al. 2011).

2.8.4 Summary of Radar Observations of Elevated Convection

Since it appears that a simple dichotomy between surface-based and elevated convection apparently does not exist (e.g., Corfidi et al. 2008, Parker 2008, Nowotarski et al. 2011), yet given the hazards associated (or typically not associated) with elevated convection (e.g., Grant 1995, Moore et al. 2003, Horgan et al. 2007), it is important operationally to determine whether convection is elevated or surface-based or somewhere on a spectrum between the two. Both Marshall et al. (2011) and Billings and Parker (2012) found at least some success in using radar velocities in determining convection to be, or transitioning to, surface-based rather than elevated. Furthermore, other characteristics such as somewhat weaker reflectivities (Smull and Augustine 1993, Marshall et al. 2011), an overall lack of a gust front (Wilson and Roberts 2006, Marshall

et al. 2011), and unique spacings and orientation (Corfidi et al. 2008) in association with elevated convection have been observed. Still, these observations largely lack substantiating research given the limited use of radar observations to advance our understanding of elevated convection.

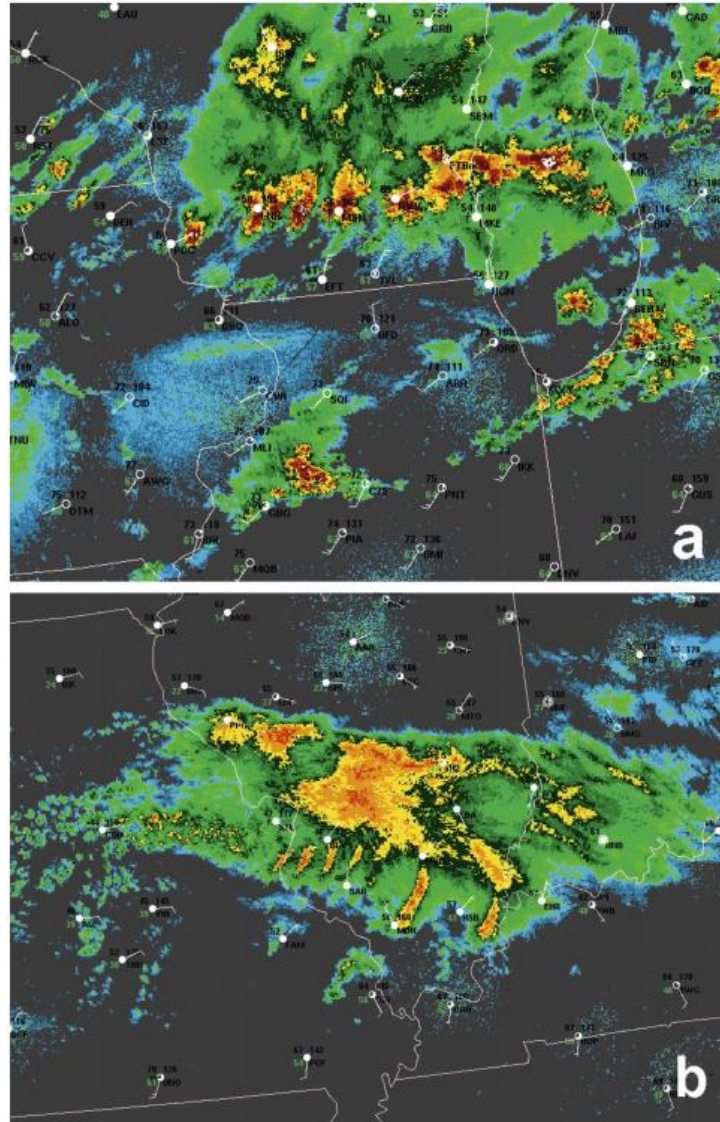


Figure 2.6: a) Composite reflectivity data showing a line of evenly spaced elevated thunderstorms, some supercells, over southern WI at 0600 CDT 4 Oct 2006. Conventional surface data locate west-east-oriented cold front along radar fineline over northern IL. Surface-based warm sector thunderstorms are present over northern IL and northwest IN. b) Composite reflectivity data showing elevated shower and thunderstorms in short bands over southern IL at 1800 CDT 26 Mar 2008. Conventional surface data show west-east-oriented stationary front extending from southern MO into western KY. Taken from Corfidi et al. (2008).

Chapter 3: Methodology

3.1 Event Selection: Elevated Cases

Cases of elevated convection were examined which correspond to field deployments within the broader scope of this research work known as the Program for Research on Elevated Convection with Intense Precipitation (PRECIP). Field deployments for this project took place during 2014 and 2015 between the months of March and October which fully encompasses the climatological peak of elevated convection (Colman 1990a). The study area from which these field deployments, and thus the corresponding cases examined, were drawn was generally over the central Plains from Oklahoma northward to Nebraska and Iowa, which again relates to the areas climatologically most favorable for elevated convection to occur (Colman 1990a).

Through the 2014 and 2015 field season campaigns, a total of 8 deployments or intense observing periods (IOPs) occurred. Most of the IOPs occurred during the month of June (5) and no IOPs occurred after the month of July. Given the climatology of Colman (1990a), it is not surprising that occurrences of heavy elevated convection occurred less frequently during the later portions of the field seasons; however, more cases would have typically been expected to have occurred in April and May.

Table 3.1: All intense observing periods (IOPs) from the 2014-2015 Program for Research on Elevated Convection with Intense Precipitation (PRECIP) field season. Italicized IOPs were ultimately excluded from this study.

	Date	Deployment Location(s)	Supporting Radar
IOP 1	02 April 2014	Clinton, MO/Ozark, MO	Kansas City, MO (KEAX)
IOP 2	03-04 June 2014	Stuart, IA/Bethany, MO	Omaha, NE (KOAX)
<i>IOP 3</i>	<i>07 June 2014</i>	<i>Emporia, KS/ Arkansas City, KS</i>	<i>Wichita, KS (KICT)</i>
IOP 4	17 July 2014	Chickasha, OK	Altus Air Force Base, OK (KFDR)
IOP 5	04-05 June 2015	Nebraska City, NE/ St. Joseph, MO	Hastings, NE (KUEX)
<i>IOP 6</i>	<i>10-11 June 2015</i>	<i>Columbus, NE/Beatrice, NE</i>	<i>Omaha, NE (KOAX)</i>
IOP 7	24-25 June 2015	Iowa City, IA/ Bloomfield, IA	Des Moines, IA (KDMX)
<i>IOP 8</i>	<i>08 July 2015</i>	<i>Columbia, MO</i>	<i>Columbia, MO (MZZU)</i>

Although 8 total deployments occurred, only 5 of these IOPs were included in this study. The other 3 cases were not examined for various reasons. IOP 3 was excluded because this event was primarily one large mesoscale convective system (MCS) that swept through the region. This is opposed to several individual convective cells or at least groups of cells as was typically observed in the IOPs that were included. A similar occurrence was the reasoning behind the exclusion of IOP 6. Again, this case was largely an incoming MCS with less than desirable individual convective cells. Furthermore, the

MCS actually underwent weakening as it reached a distance close enough to the KOAX radar site. Finally, IOP 8 was excluded for two reasons. First, the event was largely stratiform rainfall and convective cells were very limited and weak. Second, while the newly installed MZZU radar was collecting data, the collected format remained very raw at this point in time and thus data would be difficult to use for this event.

3.1.1 Field Deployment Criteria

In order for a field deployment to occur, a team of forecasters associated with the project must deem that heavy rainfall with the potential for flash flooding would occur as a result of elevated convection within the aforementioned study area. This determination was primarily based upon the results of McCoy (2014) which outlined the most likely meteorological parameters that would indicate a favorable setup for heavy rainfall to occur as a result of elevated convection.

Convection was forecast to be elevated based largely on those criteria originally outlined by Colman (1990a). That is that elevated convection would occur on the cold side of a surface front which was clearly delineated by temperature, dewpoint, and wind and a clear theta-e gradient with lower values on the cold side of the front and higher values on the warm side of the front. Given the advantage of having access to model forecast soundings, an environment that seemed favorable for elevated convection would also be examined to be assured that convection would occur in a region with a low-level stable layer (indicated by a temperature inversion and a region of increasing theta-e with height) with CAPE to be realized by lifting a parcel from the layer of highest theta-e (Rochette et al. 1999).

With specific regards to the radar-related aspects of this project, a field deployment must occur to a region within the study area with the aforementioned favorable conditions that is also well observed by Doppler radar. As much as possible, deployments occurred to locations within 100 km of an NWS WSR-88D radar in order to best examine the lowest levels of any elevated thunderstorms that may occur. Due to the curvature of the earth, at distances much further than 100 km the radar beam would overshoot, and thus not sample, some seemingly critical levels to understanding elevated convection, particularly those at or below 1 km AGL. After a date of 01 July 2015 locations within 70 km of the newly installed MZZU research radar, located just southeast of Columbia, MO at South Farm of the University of Missouri, could also be considered for deployment.

3.2 Event Selection: Surface-Based Case

While elevated convective cases were the original focus of this study, it became evident that a surface-based case was also needed to act as a comparative control. This is especially true with regard to the convergence (divergence) characteristics within the respective cell types given that such convergence (divergence) characteristics have not been widely studied in surface-based or elevated cells. In order for surface-based cells to lie on the other end of the spectrum (Corfidi et al. 2008) from elevated cells, the events included in the pool of potential cases from which one was selected were required to have a representative sounding in which surface-based CAPE was equal to most unstable CAPE. This was seemingly the best way to ensure that the surface-based cells were absolutely rooted within the near-surface layer based on soundings alone.

Potential cases were then selected from the month of June from the same two years that correspond to the PRECIP field deployments. To be selected, a number of convective cells needed to be evident near (within 100 km) an NWS WSR-88D that was collocated with an NWS upper-air site so that a representative sounding would be available. Furthermore, these sites were limited to generally the same region that corresponded with the PRECIP field deployments (i.e., the central Plains). A total of 4 surface-based cases were selected from June of either 2014 or 2015. From this pool of 4 cases, a case within the synoptic warm sector ahead of a cold front near Omaha, NE on 20 June 2014 was selected. This case had the best range of well-developed individual surface-based cells in close proximity to the radar site (KOAX). This case will be referred to as SB 1 during this study.

3.3 Radar Data Retrieval and Processing

Once a case was identified, NEXRAD Level-II radar data was downloaded from the National Oceanic and Atmospheric Administration's (NOAA) National Centers for Environmental Information (NCEI). Data was selected for a timeframe that encompassed the entirety of an event over the region primarily impacted. The radar site chosen to examine the data was that which best covered the convective event with more weight given to the radar site that best sampled areas of convective initiation in the case that multiple radars sampled a significant portion of the event. This might include a radar location that did not necessarily cover the areas to which a deployment occurred (in the case of the IOPs). When this occurred, convection either developed upstream of the deployment location within a region serviced by another radar (IOP 2), or the convection

primarily moved south of the deployment location in a region serviced by another radar (IOP 4).

Upon data retrieval from NCEI, the data was processed using the Warning Decision Support System – Integrated Information (WDSS-II; Lakshamanan et al. 2007) software developed by both the National Severe Storms Laboratory (NSSL) and the Cooperative Institute for Mesoscale Meteorological Studies (CIMMS) at the University of Oklahoma. The software not only converts the data to netcdf files (which are widely usable in the meteorological community) but it also merges the data from each of the elevation scans into Constant Altitude Plan Position Indicators (CAPPIs) on a 256 km x 256 km Cartesian grid (Lakshamanan et al. 2006). Thus, instead of the radar data being along a particular elevation scan that continually changes height with increasing distance from the radar, the data will be merged into sets of data along equal plains of height above ground level (AGL). These CAPPIs were developed and examined starting at a height of 0.5 km AGL going up to 12 km AGL at 0.5 km intervals with 1 km resolution.

3.4 Selected Radar Products

While the WDSS-II software is able to process numerous output products, this particular study will primarily only examine the reflectivity, convergence (divergence), and differential reflectivity (Z_{DR}) products. Reflectivity is used in order to best understand the overall precipitation structure of the convective cell(s). Meanwhile, convergence (divergence), a derived product from the velocity field (Smith and Elmore 2004), will be used as a proxy to best understand the region within the convective updraft from which parcels are being ingested. Z_{DR} is utilized to examine what are known as Z_{DR}

columns, a column of locally high Z_{DR} values extending above the freezing level, which is known to correspond to the updraft of convection (Kumjian 2013).

Using velocity derived convergence (divergence) within either the operational or research radar meteorological community has been quite rare. However, azimuthal shear, which is calculated in WDSS-II using the same two-dimensional, local, linear least squares derivative (LLSD) method outlined in Smith and Elmore (2004), has been more widely used. This is especially true in relation to rotation tracks (which are based on azimuthal shear) which are used to efficiently locate and track any mesocyclones within thunderstorms (Newman et al. 2013; Miller et al. 2013). Thus, despite the use and reliability of azimuthal shear, convergence (divergence) has not been used and is likely not utilized to its full potential as a meteorological radar tool.

Wilson and Roberts (2006) used surface convergence as a proxy to determine storm initiation within the IHOP_2002 project. This surface convergence was determined based on a number of factors including 3-hourly Hydrometeorological Prediction Center (HPC) surface maps, surface station reports, visible satellite, as well as fine lines noted on radar reflectivity and “Doppler velocity convergence features.” It is hypothesized that the LLSD convergence (divergence) product processed by the WDSS-II software may also be able to be used as a proxy to determine whether a convective cell may be either surface-based or elevated. Particularly, where strong convergence extends to the surface in close proximity to the convective updraft, the cell may be more likely to be deemed as surface-based.

3.5 MATLAB Analysis

Once the data was processed to the 256 km x 256 km Cartesian grid, the data was ingested into MATLAB software for analysis. For a selected time, one which would nearly correspond to the initiation of a convective cell or the entrance of a convective cell into the region of close enough proximity to the radar in order to analyze the low-levels, reflectivity for the 2 km CAPPI was analyzed to identify individual storm cells based on a minimum reflectivity threshold ranging from 42-56 dBZ. A storm cell would be identified as such when an area of adjacent pixels exceeds the minimum reflectivity threshold. A storm cell could be as few as only 1 pixel. The threshold range was altered based on the nature of convection on a particular day (i.e., many clustered relatively strong cells might require a higher threshold), or the time being sampled with respect to the cells lifecycle (i.e., the threshold might be initially lower in order to capture the cells' initiation).

Once each of the individual storm cells was identified, the particular cell of interest would be input by the user (based on the associated cell ID). Once the cell of interest was input by the user, the code would then reconstruct the vertical column (based on the 0.5 km interval CAPPIs) of reflectivity, convergence (divergence), and Z_{DR} for a 31 x 31 km area centered on the location of maximum reflectivity. From within this 31 x 31 km box the code would then accomplish three main goals: 1) locate the approximate location of the convective updraft based on the Z_{DR} column, 2) extract the location and magnitude of the vertically extending convergence column from within the approximated convective updraft, and 3) produce 3-dimensional vertical cross-sections in the west-to-east, north-to-south, and northwest-to-southeast directions through the updraft area.

This process would continue for the selected convective cell so long as the user continued to input the cell ID of the cell being analyzed once the analysis of the previous time had finished. Occasionally, when two cells were in close proximity to one another (and thus seemingly merged), or when a cell was weakening, the code had to be stopped in order to input a new minimum reflectivity threshold. In such cases, the cell would need to simply begin to be tracked again using the original steps starting from the time at which the minimum reflectivity was required to be updated.

3.5.1 Z_{DR} Column Location

Again, a number of studies (e.g., Illingworth et al. 1987, Brandes et al. 1995, Scharfenberg et al. 2005) indicate that a column of enhanced Z_{DR} values that extends above the local freezing level is indicative of the region that very nearly corresponds to the convective updraft. This is because the convective updraft is strong enough to loft both large supercooled drops as well as wet ice particles above the freezing level which thus enhances Z_{DR} values (e.g., Hall et al. 1984, Illingworth et al. 1987, Kumjian 2013).

It should be noted that the Z_{DR} values referred to herein are a 3 x 3 pixel average of the raw Z_{DR} values unless otherwise noted. This is done to clean up noise noted within the raw values. Furthermore, for the purposes of locating the Z_{DR} column, only raw Z_{DR} values corresponding to pixels of reflectivity greater than 25 dBZ were considered in calculating this average. Thus, a Z_{DR} column could not be located where reflectivity was less than 25 dBZ. Also, if a pixel did have a reflectivity value above 25 dBZ but neighboring pixels within the 3 x 3 average did not, the pixels that failed to meet the threshold were assigned a value of 0 dB and then averaged.

The algorithm composed for this research work (Appendix A) examines the region between 2.5 km AGL and 4.5 km AGL for a coherent column of enhanced Z_{DR} (dB) values compared to the surrounding areas. If the maximum Z_{DR} at each of these levels is found to exist in a columnar fashion, the particular identified location within the convective cell is deemed the location of the Z_{DR} column. For example, if the maximum Z_{DR} at 2.5 km AGL was found to be at cell (17, 15), and the maximum Z_{DR} at 3 and 3.5 km AGL was in cell (16, 14), and the maximum Z_{DR} at 4 km AGL was (15, 14), this would be considered a columnar fashion and thus be considered a Z_{DR} column with a base located at cell (17, 16) of 2.5 km AGL. Within 2 grid cells is close enough to be consider a part of the column. Only two levels need to have a maximum within the column for a Z_{DR} column to be identified. That is to say, if the same example were altered to a maximum Z_{DR} at 2.5 km AGL found at cell (17, 15), and the same at 3 km AGL was at cell (2, 19), but the same at 3.5 and 4 km AGL was at cell (17, 16), the maximum at 3 km AGL would be assumed to be either erroneous or just not associated with the updraft and thus the Z_{DR} column base would still be located at (17, 16) at 2.5 km AGL.

The process of checking for a column occurs in two stages: 1) stage 1 beginning at 2.5 km AGL and going up to 4 km AGL and 2) stage 2 beginning at 3 km AGL and going up to 4.5 km AGL. If a column is not found in stage 1, perhaps the Z_{DR} column is a bit higher and can be found in stage 2. If a column is found in both stages, the base of the Z_{DR} column is assigned to the cell and height corresponding with the stage that found a more coherent column (based on the number of checked levels found to be in the column). Stage 1 corresponds to a base height of 2.5 km AGL and stage 2 the same at 3 km AGL. If columns in both stages happened to be found to be equally coherent, the cell

and height is set to the stage with the highest Z_{DR} value at the base. An example of the locating of the Z_{DR} column is provided in Figure 3.1.

It is then assumed that the Z_{DR} column nearly corresponds with the convective updraft (e.g., Tuttle et al. 1989, Bringi et al. 1991, Brandes et al. 1995). This method could admittedly be improved by allowing for a better range of heights for the Z_{DR} column to exist, particularly as the height of the freezing level is altered. However, this method has shown enough success to be implemented for this study as described in the next section.

3.5.2 Definition and Identification of a “Convergence Column”

Obviously, it is well known that winds within a convective updraft converge and rise (e.g., Byers and Braham 1948). Furthermore, it has already been established that the Z_{DR} column corresponds to the convective updraft and so it is assumed that a region of Doppler velocity derived convergence would be located near the Z_{DR} column. This has indeed been found to typically be the case (this is explored in greater detail below). Therefore, since there is an area of convergence seemingly associated with the convective updraft, and is in some ways a measure of the updraft, details with respect to the titled column of convergence, or “convergence column,” such as height and magnitude are used as a proxy for these details with respect to the updraft itself. The determination of inflow source region of the updraft (i.e., surface-based or elevated) is based upon the degree to which the convergence column reaches the near-surface layer.

Proper identification of the Z_{DR} column is essential to locating the convergence column associated with the convective updraft. The location of the Z_{DR} column base (the

star in Figures 3.1 and 3.2) is the starting point to identifying the typically tilted column of convergence. The algorithm used here (Appendix A) begins by recording the location and value of the maximum convergence within a 3 x 3 grid (green box in Figure 3.2; analogous to a 9 km² box) centered on the grid cell corresponding to the previously determined Z_{DR} column base (the star in Figures 3.1 and 3.2). Then the maximum convergence is selected from a 4 x 3 box at the level 0.5 km below the Z_{DR} base. The 4 x 3 box has two pixels to the south (right in Figure 3.2) and one pixel to the north (left in Figure 3.2) of the pixel associated with the maximum convergence at the height above. Thus, the selection of the maximum convergence at 0.5 km below the Z_{DR} base is locationally based on the maximum convergence at the base of the Z_{DR} column. This process is then repeated at each 0.5 km level until the 0.5 km AGL level is reached, each time basing the 4 x 3 box from which the level's convergence maximum is chosen on the location of the convergence maximum at the level 0.5 km above.

A similar process is used to detect the convergence column going up in height. Again, a 4 x 3 box, this time at the level just above the Z_{DR} column base, is used to select the maximum convergence. However, when going up in height from the Z_{DR} column base, two pixels of the 4 x 3 box are to the north (left Figure 3.2) and only one pixel is to the south (right in Figure 3.2) in relation to the location of the pixel of the maximum convergence at the level previously analyzed below. Again, the maximum convergence is then chosen from this 4 x 3 box and the process repeats at each 0.5 km level above until 12 km AGL has been reached or a raw convergence of less than $0.5 \times 10^{-3} \text{ s}^{-1}$ has been selected.

Going in either direction, up or down from the Z_{DR} column base, the grid is extended to 4 grid cells (analogous to 4 km) in the north-south direction in order to best compensate for the typical tilting of the convergence column in the north-south direction.

An example is provided in Figures 3.1 and 3.2 below to best illustrate both how the Z_{DR} column is located and then how this location is, in turn, used to locate the convergence column. Note that while these examples indicate that each value in either column is located in this particular cross-section, in the actual algorithm the Z_{DR} column and the convergence column can move in both the north-south direction (as shown in these example figures) and in the east-west direction according to the box dimensions outlined above (i.e., into another cross-section).

Given that there is some inherent noise in the convergence data, the convergence column data required an averaging technique after finding the maximum convergence at each level within the column. This was done by taking a 3 x 3 average centered on the pixel at each height with the maximum convergence. This is thought to be more representative of the convergence column than only recording the maximum convergence value itself, given that, on occasion, the maximum value seemed to be a bit erroneous. If, of course, the value was in error, this value would now hold much less weight given that it would be averaged out by seemingly more representative values around it. This does possibly also average out some maximum values that are of good quality. Where these values seem to occur, they may be reported in raw form. In general, values of convergence will be averaged using the aforementioned technique unless otherwise stated to be in “raw” form.

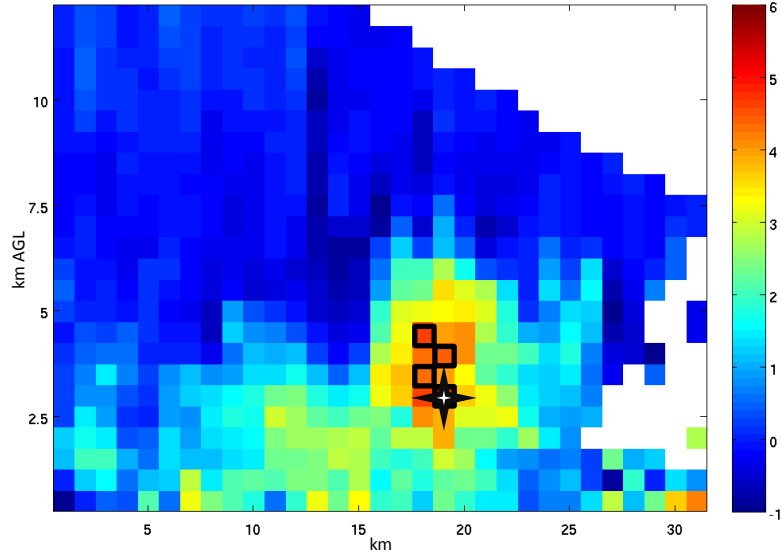


Figure 3.1: An example of a Z_{DR} column as selected by the algorithm used in this study; Z_{DR} shown in dB. The star represents the location of the selected Z_{DR} base. The black boxes are indicative of the maximum 3×3 average Z_{DR} at each 0.5 km AGL height and are thus part of the Z_{DR} column. Note: while this is based on real data, this may not actually be representative of the actual Z_{DR} column selected. The actual algorithm very well may select pixels not shown in this cross-section (they could be from neighboring cross-sections analogous to moving west or east). This image is merely for illustrative purposes.

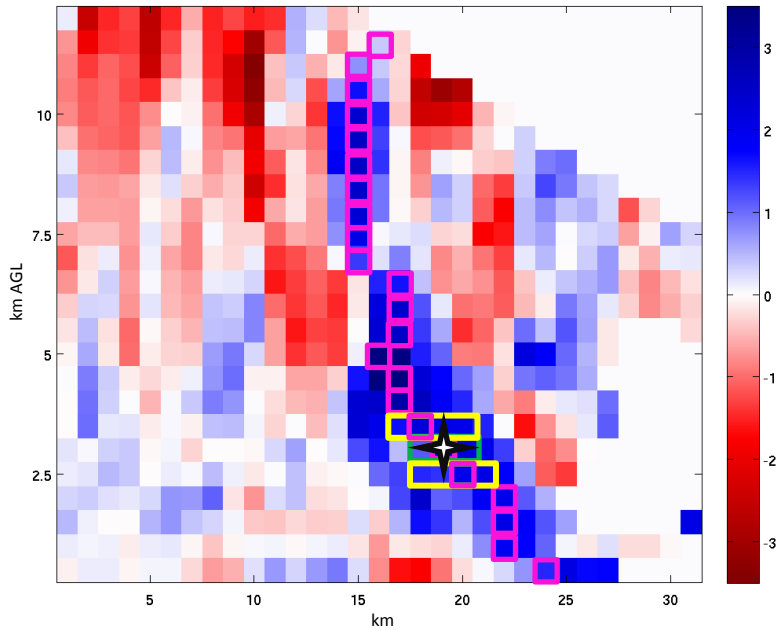


Figure 3.2: An example of a convergence column as selected by the algorithm used in this study; convergence (blue)/divergence (red) shown in 10^{-3} s^{-1} . The star is located at the base of the Z_{DR} column (as in Figure 3.1). A 3×3 box (shown in green) centered on the Z_{DR} column base (star) is the starting location for the algorithm to extract the values and locations of the maximum convergence corresponding to the convergence column. The 4×3 box from which the maximum convergence is selected is shown in yellow for the 0.5 km levels both above and below the Z_{DR} column base level. At each height, the magenta box outlines the pixel of maximum convergence from within the convergence column. Note: while this is based on real data, this may not actually be representative of the actual maximum convergence values selected. The actual algorithm very well may select pixels not shown in this cross-section (they could be from neighboring cross-sections analogous to moving west or east). This image is merely for illustrative purposes.

Using the method for identifying a convergence column described above, a convergence column was detected around 74% of the times at which cells were observed in this study. A *convergence column* in this study is defined as having a 3 x 3 convergence average (centered on the maximum convergence as described) greater than 0.10^{-3} s^{-1} over a 4 km depth within a coherent column. This column is associated with the convective updraft based on its collocation with the Z_{DR} column. Examples of convergence columns that are clearly associated with the convective updraft given a collocation with the Z_{DR} column are given in Appendix B.

3.5.3 Vertical Cross-Sections

Vertical cross-sections were also extracted by the code in west-to-east, north-to-south, and northwest-to-southeast slices through the 31 x 31 km box and across the cell. Originally, only west-to-east and north-to-south cross-sections were examined. However, it seemed advantageous based upon early results to include a diagonal cross-section through the convection given a general observation that areas of strong convergence were found to possibly follow a northwest-to-southeast pattern when examining the west-to-east and north-to-south cross-sections. The cross-sections are particularly useful for examining the convergence column with height.

3.6 Cell Selection

In order to limit the complexity of data extraction and analysis for each respective case, only five individual convective cells were selected per case. To best objectively select the five cells from the event, the five most intense convective cells based upon composite reflectivity were analyzed. The cell would then be traced forward and

backward in time from the point at which the cell was the most intense in order to best perceive the changes in the convective cell throughout its lifecycle. On occasion, one of the top five most intense cells from within the range of the radar's coverage during the event might be excluded. This would be the case if most of the cell's lifecycle occurred at a distance near the periphery of the radar's best coverage or if the data for a particular cell was consistently poor. In such cases, the next most intense cell was included in the dataset so that each case had a total of five cells examined. There is certainly room to expand this study to more convective cells including those that only reach weak to moderate intensities.

Chapter 4: Results

4.1 Thermodynamic Overview of Cases

Before examining the specific radar details within the convective cells from the events analyzed, it is important to understand the thermodynamic environment associated with each case. This is especially essential to this study given that the literature has consistently shown that a case cannot be specified as elevated based on having considerably more most unstable CAPE (MUCAPE) than surface-based CAPE (SBCAPE) (e.g., Parker 2008, Nowotarski et al. 2011, Billings and Parker 2012, Schumacher 2015). As summarized in Section 2.7.3, it seems a case can only be *absolutely* classified as being elevated if no SBCAPE exists. Events in which MUCAPE exceeds SBCAPE likely lie somewhere on a spectrum somewhere between purely elevated and purely surface-based (Corfidi et al. 2008). Given that this was not necessarily considered when deploying the PRECIP field team to take observations, each intense observing period (IOP) included in this study needs to be closely examined thermodynamically to determine if the case is purely elevated or could potentially lie somewhere along the aforementioned spectrum.

Examining the five IOPs used in this study, only upper-air observations from IOP 1 (Clinton, MO) and IOP 4 (Chickasha, OK) had no SBCAPE throughout the event (Table 4.1). Meanwhile, in both cases over 1000 J/kg of MUCAPE was observed at some point during the observation period. Furthermore, each of the cases had an effective inflow layer base (EILB: as defined by Thompson et al. 2007), between 0.7 km and 1.3

km AGL. Thus, a difference should in theory be observable between the 0.5 km AGL radar-detected convergence and the convergence detected at heights above the EILB (such as at 1.5, 2, 2.5, etc. km AGL).

The other IOPs varied in amounts of SBCAPE and EILB heights. Of all the observed soundings from the northern, and presumed elevated observation sites, only the initial and pre-convective observed sounding from Stuart, IA in IOP 2 had an EILB height that extended all the way to the surface. The remaining observed soundings from IOP 2 at Stuart, IA had EILB heights below 0.1 km and thus were essentially at the surface. Certainly no difference would be expected to be observed in 0.5 km AGL convergence values observed by radar in such a case. Thus, it seems reasonable to assume that convection, at least initially, during IOP 2 was dominated by surface-based convection despite its location north of the synoptic warm front, a location that has typically been considered to be dominated by elevated convection (e.g., Colman 1990a, Moore et al. 2003). Nevertheless, this event will be more closely scrutinized from a radar perspective in Section 4.4.

Observed soundings from IOP 7 at Bloomfield, IA are very similar to that of IOP 2, however, in each of these soundings the EILB is at least somewhat above the surface due to a great deal of surface-based CIN as a result of a low-level inversion. Nevertheless, the EILB remains below 0.5 km AGL, yet again making a radar determination of any degree of elevated inflow not possible. The observed soundings from Iowa City, IA, further north during the same event, are more promising with EILB heights above 0.5 km AGL. Unfortunately, this location is a great distance from the radar. Furthermore, convection was limited in this area.

Table 4.1: A summary of the thermodynamic environment for the IOPs examined in this study. The values represented here are from actual observed upper-air data collected from the PRECIP field team. Italicized columns emphasize soundings with no SBCAPE. SBCAPE and MUCAPE values with an asterisk (*) are likely not representative of the actual environmental values at the indicated times. In such cases, the upper-air flight was terminated early due to flight errors of some kind and thus the sounding is not complete. Thus the actual SBCAPE and MUCAPE values in these instances are almost certainly higher.

Event	Time	SBCAPE (J/kg)	MUCAPE (J/kg)	Height of MU Parcel (km)	EILB (km)
<i>IOP 1 – Clinton, MO</i>	<i>0400 UTC 04/02/14</i>	<i>0</i>	<i>893</i>	<i>~1.19</i>	<i>~0.92</i>
	<i>1000 UTC 04/02/14</i>	<i>0</i>	<i>1066</i>	<i>~1.50</i>	<i>~0.80</i>
IOP 2 – Stuart, IA	2200 UTC 06/04/14	*698	*698	0	0
	0000 UTC 06/05/14	99	1009	~2.13	~0.06
<i>IOP 4 – Chickasha, OK</i>	<i>0400 UTC 07/17/14</i>	<i>0</i>	<i>1039</i>	<i>~1.40</i>	<i>~0.87</i>
	<i>0600 UTC 07/17/14</i>	<i>0</i>	<i>610</i>	<i>~2.09</i>	<i>~0.87</i>
IOP 5 – Nebraska City, NE	0000 UTC 06/05/15	536	1138	~0.82	~0.75
	0300 UTC 06/05/15	*84	*151	~2.96	~2.76
IOP 7 – Bloomfield, IA	2300 UTC 06/24/15	840	1894	~0.61	~0.01
	0400 UTC 06/25/15	*117	*966	~0.80	~0.11

Finally, upper-air observations from Nebraska City, NE during IOP 5 have EILB heights ranging from 0.7 km to over 2.7 km, the highest EILB of any observed soundings in this study. While there is some limited amount of SBCAPE in the Nebraska City, NE soundings, a strong inversion results in a large amount of CIN when lifting a parcel from

the surface. This is exactly the type of case where radar-derived convergence could provide a considerable amount of value in determining where on the spectrum of elevated or surface-based convection a cell may occur, especially as an inversion may be altered dynamically with the introduction of convection.

4.2 Elevated Case Study

To initially determine if a difference is indeed observable within the radar-derived convergence below the EILB, IOP 1 was selected as the best purely elevated case and thus was closely examined. IOP 1 was selected over IOP 4 because the upper-air site at Clinton, MO in IOP 1 directly sampled a significant portion of the convective event. However, during IOP 4, many of the most intense convective cells were displaced well to the south of the upper-air observation site at Chickasha, OK. Much of the convective event took place near the Red River valley and closer to the warm front where the EILB was likely lower and some degree of SBCAPE could have been available to convective cells.

The PRECIP field team deployed to portions of western Missouri (Clinton and Ozark, MO) to observe and sample elevated convection via upper-air weather balloons from the evening hours of 01 April 2014 through the morning hours of 02 April 2014 (this event is referred to as IOP 1). The synoptic setup included a west-southwesterly upper- and mid-level flow with slight ridging by 1200 UTC, not uncommon for elevated convective situations (Colman 1990a, Moore et al. 2003). Furthermore, a 100-125 kt jet-streak was located from Iowa into the Great Lakes region during the deployment time frame, which placed portions of western Missouri and central to eastern Kansas within

the right-entrance region of the jet-streak which created an enhanced area of upper-level divergence.

At 700 mb, a shortwave was evident moving from the panhandles of Texas and Oklahoma at 0000 UTC 02/04 into central Kansas by 1200 UTC. Meanwhile, an 850-mb low-level jet (LLJ) seemed to advect warm, moist air over an analyzed surface stationary/warm front located over southern Missouri. This created an area of elevated instability (as evidenced by collected upper-air data) over a low-level stable layer north of the surface front. With multiple forms of lift in place (upper-level divergence, 700-mb shortwave, warm-air advection and low-level isentropic ascent), this was a prime setup for elevated convection from eastern Kansas into portions of western Missouri.

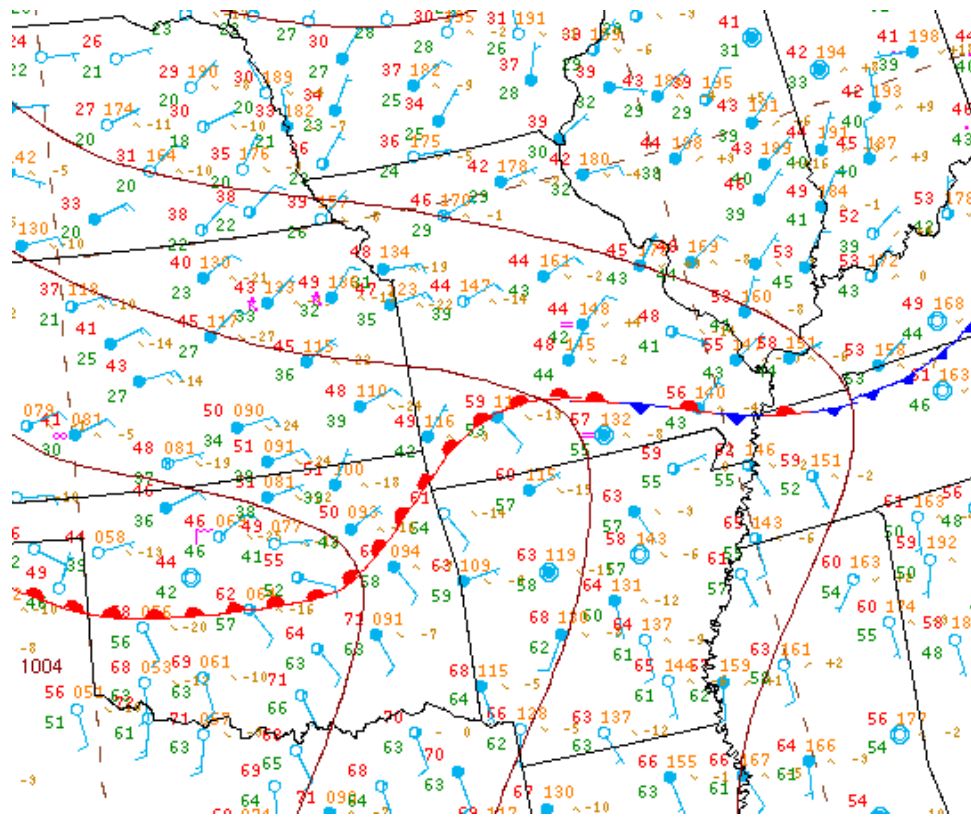


Figure 4.1: Surface analysis valid at 0600 UTC on 02 April 2014. Map courtesy of the Weather Prediction Center (WPC).

Again, of particular note, there was no SBCAPE available as indicated by soundings taken by the PRECIP field team in Clinton, MO. Meanwhile, around 900-1000 J/kg of MUCAPE was present in these same soundings (Figure 4.2). Given that the primary objective of this project is to use the radar derived convergence as a proxy for determining inflow within the observed convective cells, it is important to note the height at which CAPE becomes available to lifted parcels. The EILB in the observed soundings from Clinton, MO at 04 UTC (Figure 4.2) and 10 UTC 02/04 (not shown), the two times that approximately correspond to the two waves of convection observed during this event, was as low as around 0.78 km AGL. Thus, it would be reasonable to see convergence associated with the inflow of these convective cells in all but the lowest 0.5 km AGL.

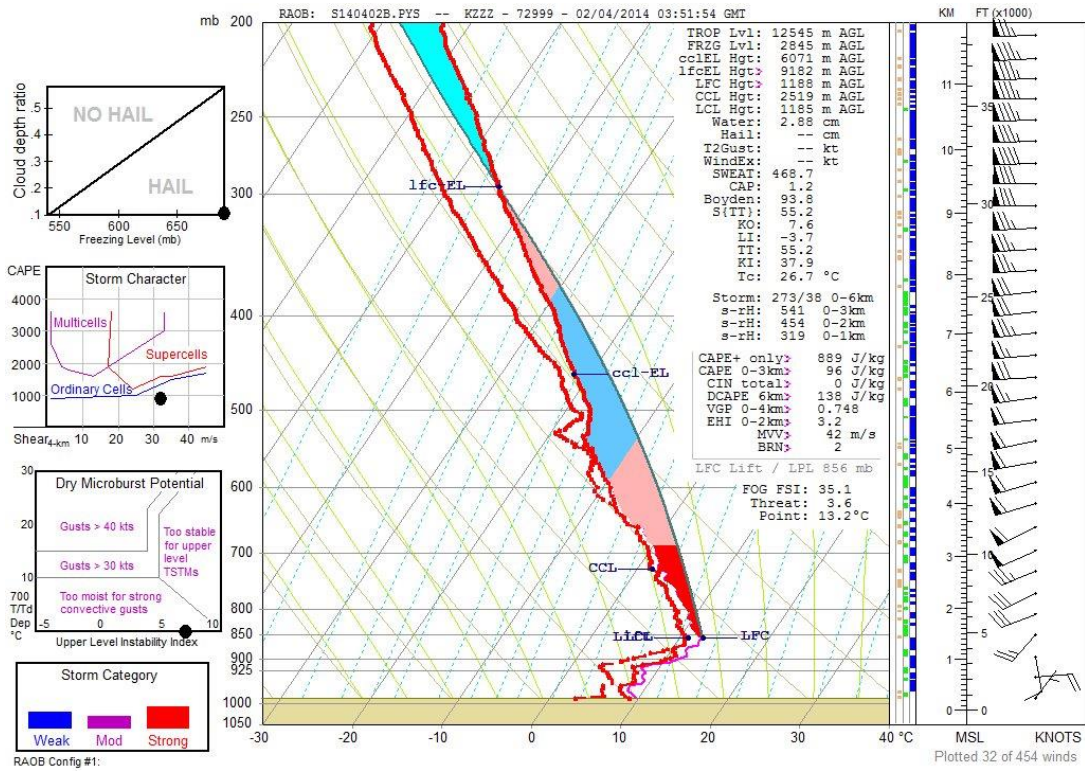


Figure 4.2: Observed upper-air sounding from Clinton, MO valid at 0400 UTC on 02 April 2014.

As already alluded to, two distinct episodes of elevated convection occurred over eastern Kansas and western to central Missouri between 2100 UTC 01/04 and 1200 UTC 02/04. The first round of elevated convection (Figure 4.3) initiated over extreme east-central Kansas around 2230 UTC 01/04 with a continual increase in coverage and intensity over the next couple of hours as convection drifted eastward into western and eventually central Missouri. This round of convection passed directly over the PRECIP upper-air deployment site located in Clinton, MO. Much of this round of convection pushed into central Missouri, and east of the PRECIP launch site, by 0300 UTC 02/04.

The second wave of elevated convection (Figure 4.4) initiated over eastern Kansas, especially in the area from Emporia to Manhattan, KS around 0230 UTC 02/04. This round of convection also propagated eastward, expanding considerably in areal coverage by 0430 02/04. Convection passed directly over the Kansas City metropolitan area, including the local NWS WSR-88D radar located in Pleasant Hill, KS (KEAX). Furthermore, this round of convection passed directly over or within 100 km of the PRECIP upper-air site, again located at Clinton, MO, and thus elevated convection was well sampled by the PRECIP field team. Continued upstream development of convection prolonged this round as compared to the first. All convection had primarily moved east of both the KEAX radar coverage and the PRECIP upper-air site by 1000 UTC.

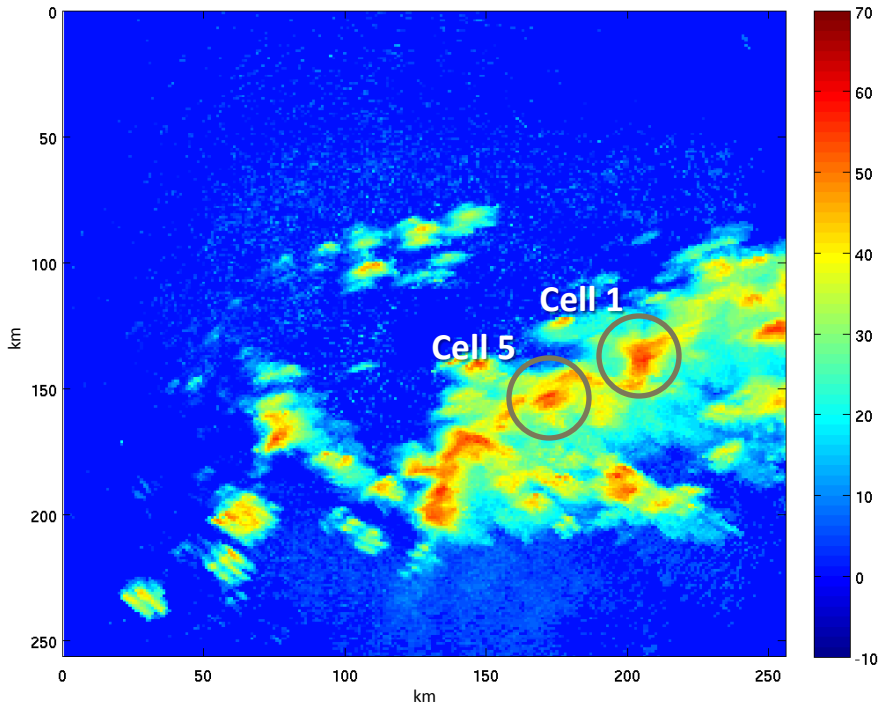


Figure 4.3: Composite reflectivity of the first round of convection, including Cell 1 and 5, as observed from the (and centered upon) the Pleasant Hill, MO (KEAX) WSR-88D. Image valid at 0550 UTC 04/02/14.

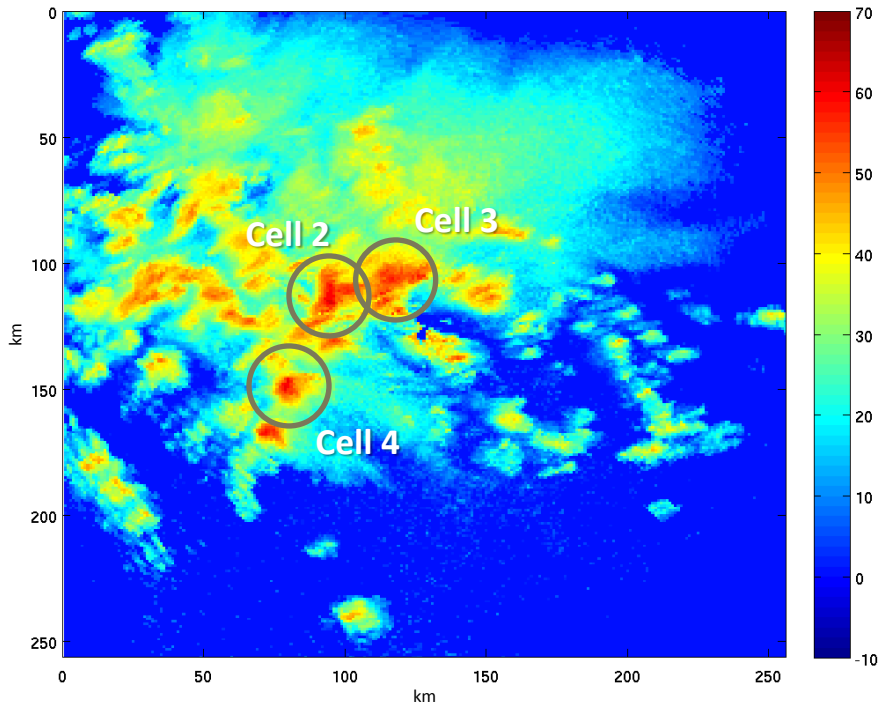


Figure 4.4: Composite reflectivity of the second round of convection, including Cell 2, 3 and 4, as observed from the (and centered upon) the Pleasant Hill, MO (KEAX) WSR-88D. Image valid at 1020 UTC 04/02/14.

A number of individual convective elements were evident via radar reflectivity from the KEAX site throughout both rounds of elevated convection. The strongest convective cells reached composite reflectivity values between 61 and 66 dBZ (Table 4.2). In order to better assess the convergence patterns within these elevated cells, each of the five most intense cells (as determined by composite reflectivity) were closely examined. Two of these selected cells occurred with the first wave of convection (Cells 1 and 5), while the other three were associated with the second.

Table 4.2: A summary of the 5 most intense cells based on composite reflectivity from IOP 1 as observed from the Pleasant Hill, MO (KEAX) radar. These 5 cells were used as the basis for studying IOP 1. *Convergence values reported here are raw values.

	Cell 1	Cell 2	Cell 3	Cell 4	Cell 5
Time Frame (UTC)	0454 – 0550	0933 – 1058	0933 – 1058	1001 – 1117	0435 – 0616
Max Composite Reflectivity (dBZ)	65.2	64.2	61.7	61.8	61.3
{time of occurrence (UTC)}	{0522}	{0952}	{1048}	{1011}	{0513}
Max Convergence* (10^{-3} s^{-1}) {time of occurrence (UTC)}	3.44 {0522}	3.95 {1011}	5.38 {1020}	3.35 {1039}	4.93 {0435}

Cell 1, the most intense by composite reflectivity (dBZ), initiated along the southern flank of a preexisting cell around 0500 UTC 04/02 almost directly between the KEAX radar site and the PRECIP upper-air site. The cell quickly intensified, reaching its maximum intensity around 0522 UTC 04/02, only about 25 minutes later. As early as 0503 UTC 04/02, just after the initiation of the cell, there is a detectable convergence column that appears to reach all the way to the surface (Figure 4.5d). The strongest convergence at this time is located at a height of 3 km AGL with a raw value already

greater than $2 \cdot 10^{-3} \text{ s}^{-1}$. Also of note, a secondary convergence column is distinguishable just north of the aforementioned in association with the preexisting cell on the northern flank of the developing Cell 1. These convergence columns correspond well with the location of the Z_{DR} columns shown to be consistent with the updraft of the cell (Figure 4.5c, d). Thus, the convergence column seems to be a reasonably good representation of the updraft with respect to its location.

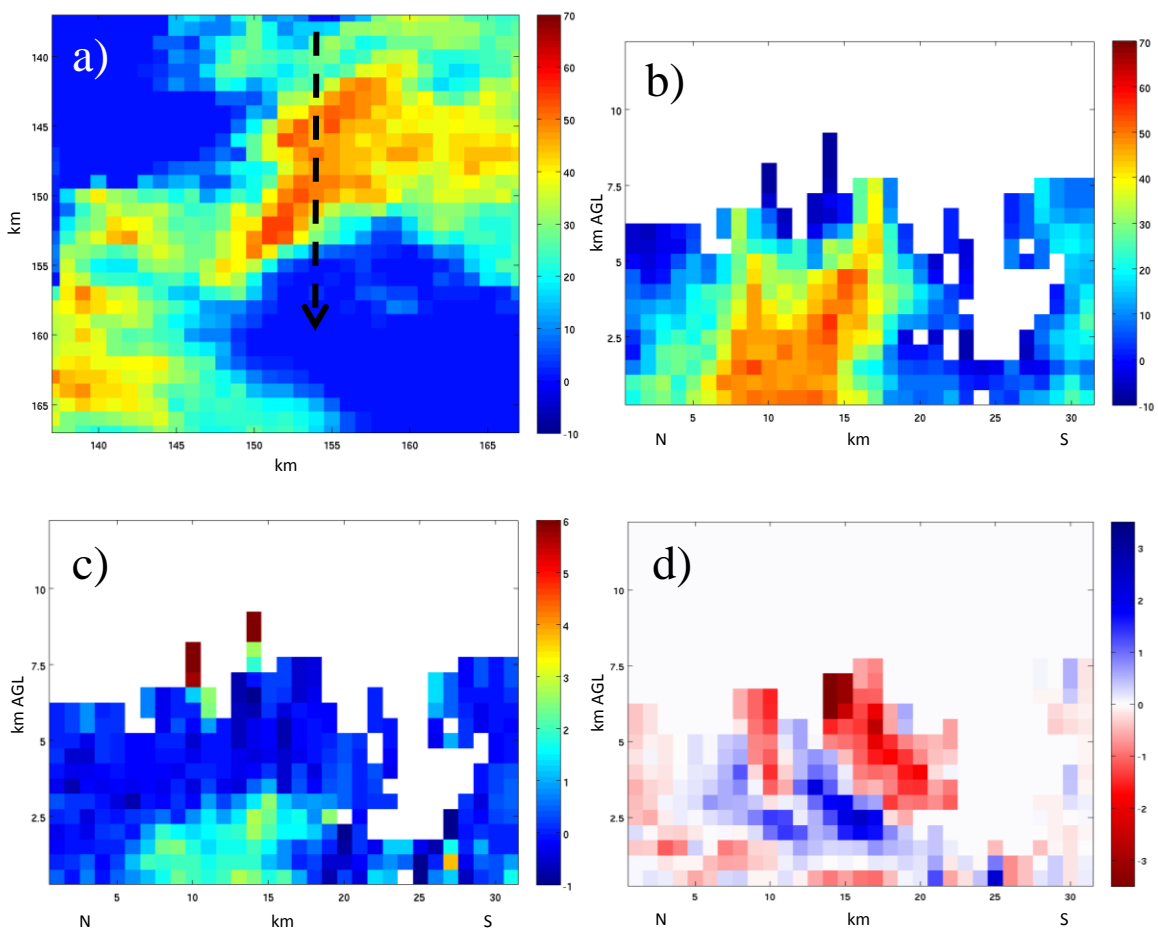


Figure 4.5: a) Plan view of reflectivity (dBZ) at 2 km AGL centered on IOP 1 Cell 1. Dashed arrow indicates the location of the north (N)-to-south (S) cross-sections shown in b), c) and d). b) Reflectivity (dBZ) cross-section of IOP 1 Cell 1. c) Z_{DR} (dB) cross-section of IOP 1 Cell 1. d) Convergence (blue)/divergence (red) (10^{-3} s^{-1}) cross-section of IOP 1 Cell 1. All valid at 0503 UTC 04/02/14.

The cell maintained a consistently distinguishable convergence column throughout its time frame within the distance reasonably observable by the KEAX radar site. Convergence column maximum values also generally remained constant, with only slight fluctuations to note. Both the maximum reflectivity and convergence value correspond to the same time (Table 4.2). However, the maximum convergence value lies at a height of 6 km AGL, which is somewhat inconsistent with the other maximum convergence height levels throughout the observed time of the convective cell. Generally speaking, the maximum convergence from within the convergence column was located from 2 to 3 km AGL for Cell 1. The average convergence profile for Cell 1 does in fact reveal the height of maximum convergence to be 2.5 km AGL with a value just over $1 \times 10^{-3} \text{ s}^{-1}$ (Figure 4.6). This is just above the height of most unstable parcel which occurred from roughly 1-1.5 km AGL.

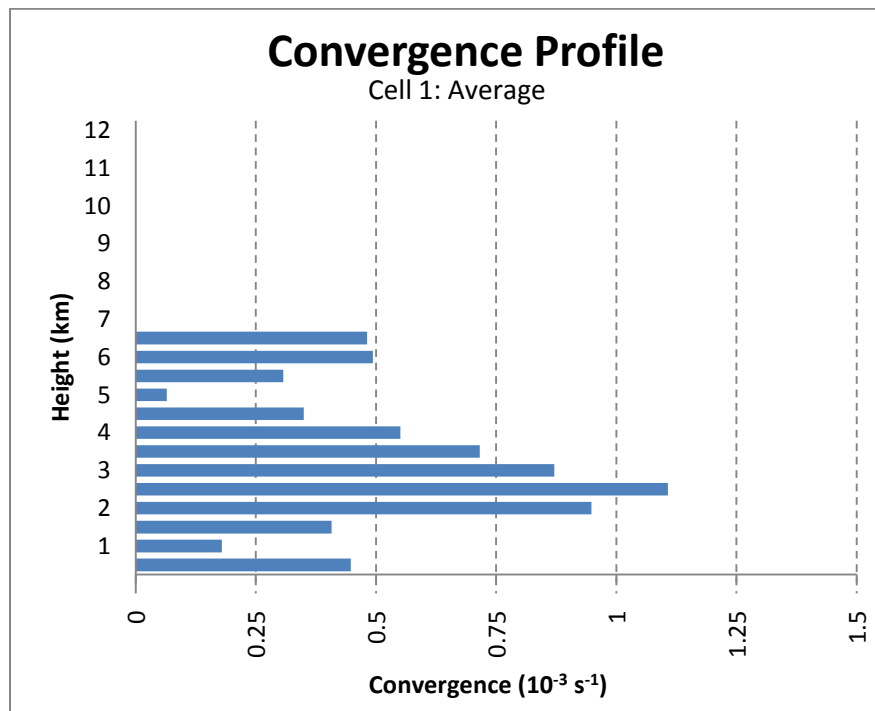


Figure 4.6: Average convergence with height for all times analyzed in IOP 1 Cell 1.

As was noted near the time of the cell's initiation, the convergence column appears to extend all the way to the lowest observed level, 0.5 km AGL (Figure 4.5d). In fact, the average convergence value at 0.5 km AGL of all times analyzed during Cell 1 was $0.45 \cdot 10^{-3} \text{ s}^{-1}$ (Figure 4.6). A 0.5 km AGL convergence value as high as $0.62 \cdot 10^{-3} \text{ s}^{-1}$ was observed at 0522 UTC 02/04. Clearly however, 0.5 km AGL is located below the height of the inversion and furthermore is below the EILB, which again was observed to be as low as around 0.78 km AGL in the 10 UTC observed sounding from Clinton, MO. Given this, it is clear that this low-level convergence is likely not entirely (or at all) related to inflow within the convective cell. Upon close examination, it should be noted that this area of low-level convergence near the base of the convergence column is just to the south of the convective downdraft where the highest reflectivity values reach the 0.5 km AGL level (Figure 4.5b, d). Thus, it seems quite plausible that outflow from the downdraft is contributing to some degree of low-level convergence. Furthermore, coupling areas of convergence/divergence near the surface provides some evidence of ducted convective rolls present during this event (Figure 4.5d). If this is in fact the case, these could also be enhancing areas of convergence near the base of the convergence column. Moreover, these ducted convective rolls could have played a role in the initial lifting required for convective initiation just above the inversion level.

When extending the analysis to the remaining 4 most intense cells from this event, a few noteworthy observations can be made. However, it should first be noted that the original Cell 3 was never in close enough proximity to the KEAX radar to be sampled at the 0.5 km AGL level. Given the importance of this level, the original Cell 3 (based on composite reflectivity) was discarded from the sample.

First, observable convergence columns were identifiable within each of the remaining 4 cells analyzed, although they took on different shapes and magnitudes (Figure 4.7). With regards to the low-level convergence at the base of the convergence column, specifically that at 0.5 km AGL, each of the 4 other cells indicated lower convergence values than an analysis of only Cell 1 (Figure 4.8). It should be noted that the average convergence value at 0.5 km AGL for Cell 1 was based on only 3 sampled times; a likely cause for a potentially misleading error. In fact, when all times sampled for each respective cell are averaged, Cells 2-5 have 0.5 km AGL convergence values of $0.13 \cdot 10^{-3} \text{ s}^{-1}$ with a standard deviation of $0.33 \cdot 10^{-3} \text{ s}^{-1}$. This further suggests that the low-level convergence within Cell 1 was a bit higher of a value than typically expected. Overall, this suggests fairly low values of convergence just above the surface, and below the inversion, as compared to heights within the convergence column just above the inversion. Obviously, the range of averages from each individual cell, which ranged from $0.45 \cdot 10^{-3} \text{ s}^{-1}$ to $0.02 \cdot 10^{-3} \text{ s}^{-1}$, should be considered. Furthermore, it is worth noting that with respect to individual observed times, a convergence value as high as $1.10 \cdot 10^{-3} \text{ s}^{-1}$ was observed at 0.5 km AGL in Cell 2. Such high convergence values do not seem to be typical overall however.

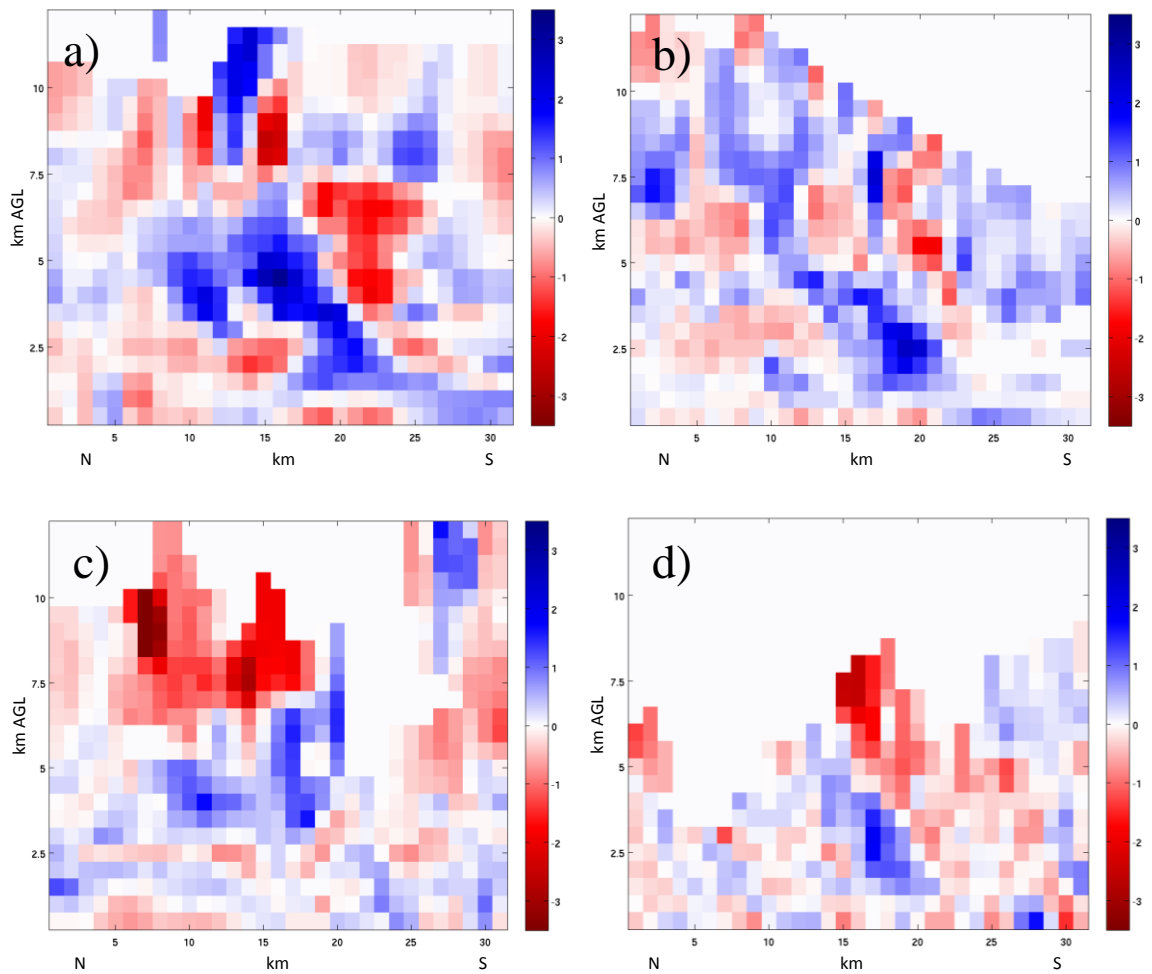


Figure 4.7: a) North (N)-to-south (S) Convergence (blue)/divergence (red) (10^{-3} s^{-1}) cross-section of IOP 1 Cell 2 valid at 1011 UTC 04/02/14. b) Same as a) of IOP 1 Cell 3 valid at 1011 UTC 04/02/14. c) Same as a) of IOP 1 Cell 4 valid at 1030 UTC 04/02/14. d) Same as a) of IOP 1 Cell 5 valid at 0513 UTC 04/02/14.

Nevertheless, values do indicate at least some slight convergence down to 0.5 km AGL. This would not necessarily be expected given that any convergence which feeds the convective updraft should occur entirely above this level. This is because air at 0.5 km AGL is below the inversion and the EILB, and thus is stable. Again, it is believed that these small convergence values may be attributable, at least in part, to outflow from the downdraft of the convective cell. This is likely not the only reason however. There are likely many different minor factors that could contribute to such low values of

convergence near the surface. Furthermore, it could be just the seemingly noisy nature of the convergence (divergence) product itself.

Given that the values of convergence near the surface do seem to be consistently small, it is assumed that, regardless of the specific explanation behind these values, they are unlikely to represent convergence extending to the surface as a result of the convective updraft. An examination of the convergence columns displayed in Cells 4 and 5 (Figure 4.7c, d) provides some evidence that some of this weak low-level convergence is not associated with the convergence column. In these examples, little, if any, coherence of the convergence column extends to the near-surface level despite areas of weak convergence that do extend to 0.5 km AGL. Higher values of convergence above the inversion, such as those clearly associated with the updraft within the convergence column, would be expected to more coherently extend to the surface if indeed the parcels were being ingested from near the surface. This will be explored in much greater detail in Section 4.3 with respect to a surface-based convective case in order to make a proper comparison between the two convective types.

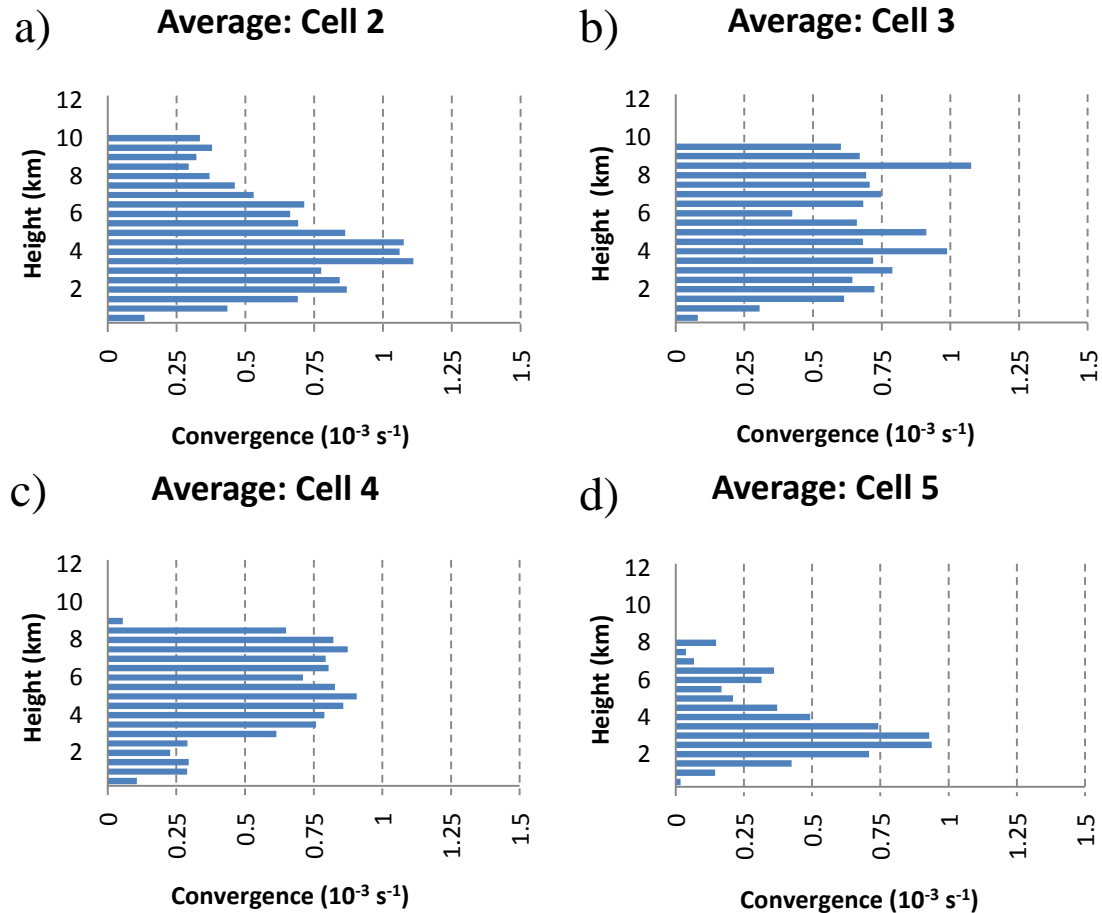


Figure 4.8: a) Average convergence with height for all times analyzed in IOP 1 Cell 2. b) Average convergence with height for all times analyzed in IOP 1 Cell 3. c) Average convergence with height for all times analyzed in IOP 1 Cell 4. d) Average convergence with height for all times analyzed in IOP 1 Cell 5.

Observations from Cells 2-5 also reveal that the level at which the maximum convergence occurs is a bit more variable than that indicated in only Cell 1 (Figure 4.8). However, it should be noted that Cell 1 also most consistently had the shallowest convergence column depth as compared to the other 4 cells (Figure 4.6). Overall, the maximum convergence height was most often located in the 2.5 km to 5 km AGL range with values between $0.8 \times 10^{-3} \text{ s}^{-1}$ and $1.2 \times 10^{-3} \text{ s}^{-1}$. The overall standard deviation for all cells was maximized (within the low-levels) near this level, at 5 km AGL, with a standard deviation of $0.56 \times 10^{-3} \text{ s}^{-1}$ suggesting a higher degree of variability with respect to the strength of the convergence column. Cell 3 most notably goes against the 2.5 to 5 km

maximum convergence height notion however, with the height of the maximum convergence reaching as high as 9.5 km AGL at 0952 UTC 04/02. Furthermore, after the convergence column values at each observed time during Cell 3 were averaged, the height of the maximum convergence was located at 8.5 km AGL (Figure 4.8b). This observation draws attention to a double peak, one maximum within the 2.5 km to 5 km AGL range and a second above 7 km AGL, within the histogram of convergence with respect to height in not only Cell 3, but also each other observed cell (Figures 4.6 & 4.8). Typically, however, the upper-level peak in convergence was less than the upper-level peak with Cell 3 again being the notable exception.

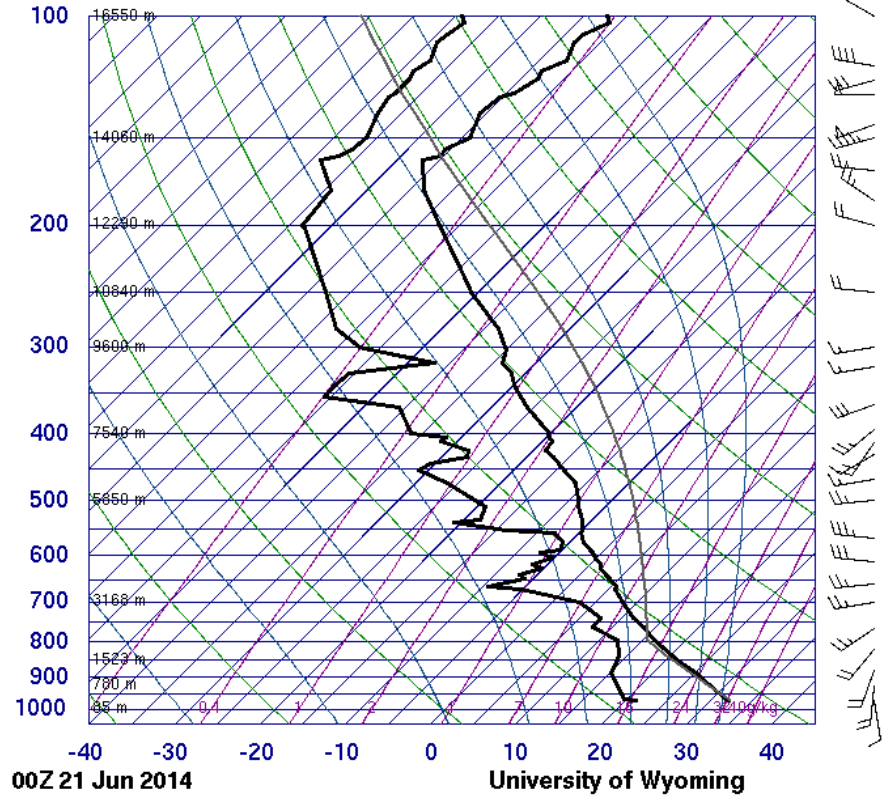
In summary, the analysis from the 01-02 June 2014 elevated convective case over eastern Kansas and western Missouri provided several key initial observations. First, the convergence column seems to clearly indicate the convective updraft within the convective cell. Convergence within this column typically is maximized in the 2.5 km to 5 km AGL range, with a secondary maximum located in the upper-level portions of the convective cell anywhere from 6 to 9.5 km AGL. Values of convergence do often extend all the way to 0.5 km AGL despite this height being below the inversion and the EILB in a layer of stable air. Convergence values are generally much reduced at this level however, and minor values of convergence are not totally unexpected given factors such as outflow from the convective downdraft and convective rolls beneath the inversion. Furthermore, minor values of convergence are not unreasonable for any number of reasons near the surface. Most importantly, the values at 0.5 km AGL are small and overall averaged $0.13 \times 10^{-3} \text{ s}^{-1}$, while convergence just above the inversion, at only 2-3 km AGL, typically ranged from 0.5 to $0.75+ \times 10^{-3} \text{ s}^{-1}$.

4.3 Surface-Based Case Study

In order to do a proper comparison, a surface-based case is essential. Using the method described in Section 3.2, a selection of potential surface-based cases was chosen. From this, the seemingly best case was selected for the sake of this comparison. Ultimately, a surface-based case (SB 1) just ahead of an advancing cold front near Omaha, NE on 20 June 2014 was selected. While consideration for this comparison could have reasonably been given to IOP 2 because of the aforementioned thermodynamic considerations, this was ultimately decided against. The reasoning for such was because convective activity associated with IOP 2 was largely located north of a warm front and not within the traditional warm sector where surface-based convection would typically be expected.

On 20 June 2014, several convective cells developed near Omaha, NE. These cells were classified as being surface-based given that the upper-air data collected from the KOAX upper-air site at 0000 UTC 06/21 had surface-based CAPE equal to the CAPE assessed from lifting the most unstable parcel (Figure 4.9). The synoptic setup for this case is fairly insignificant. Weak westerly zonal flow was present over the region at 300 mb with much the same evident in the mid-levels. At 700 mb, a shortwave was present over western Nebraska while a 20 kt south-southwesterly LLJ could be noted at 850 mb. Meanwhile, surface analysis revealed a weak area of low pressure over south-central Minnesota with a warm front extending southeastward into extreme eastern Iowa and a cold front extending into north-central Nebraska (Figure 4.10). This obviously places the entire region surrounding Omaha, NE within the warm-sector, which was to be expected given the observed sounding from KOAX.

72558 OAX Omaha



SLAT	41.31
SLON	-96.36
SELV	350.0
SHOW	-4.40
LIFT	-6.46
LFTV	-7.28
SWET	460.0
KINX	39.70
CTOT	23.30
VTOT	30.30
TOTL	53.60
CAPE	2875.
CAPV	3069.
CINS	-27.8
CINV	-10.1
EQLV	159.0
EQTV	158.8
LFCT	773.5
LCV	790.5
BRCH	51.80
BRCV	55.29
LCLT	288.9
LCLP	799.3
MLTH	308.0
MLMR	14.37
THCK	5765.
PWAT	40.01

Figure 4.9: Observed upper-air sounding from Omaha, NE valid at 0000 UTC on 21 June 2014. Figure courtesy of the University of Wyoming.

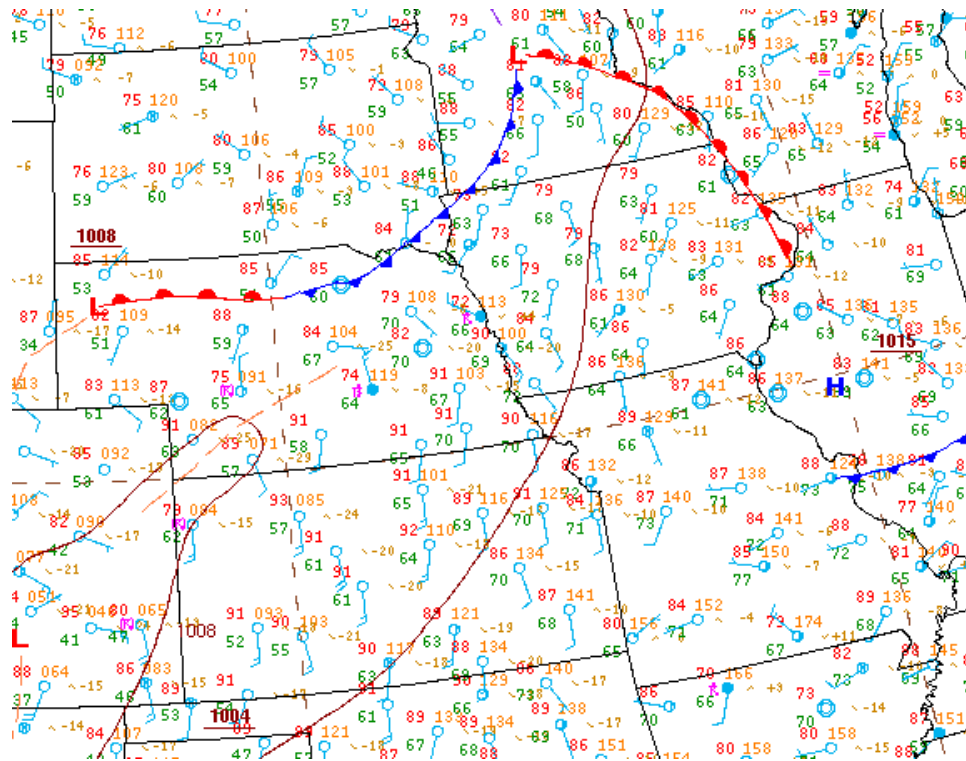


Figure 4.10: Surface analysis valid at 0000 UTC on 21 June 2014. Map courtesy of the Weather Prediction Center (WPC).

Radar analysis indicates convective initiation north and west of Omaha, NE from central into northeast Nebraska around 1930 UTC 06/20. Convective cells continued to develop as the entire cluster of cells moved south and east into the immediate area near the KOAX radar site (located just west of Omaha, NE) around 0000 UTC 06/21. Convection continued over the immediate area near the KOAX radar site until at least 0600 UTC 06/21, however, when considering the most intense cells to be analyzed for this case, only cells generally before 0400 UTC 06/21 were considered given that conditions by this point may no longer be best represented by the 0000 UTC 06/21 observed KOAX sounding. The radar analysis of the selected cells for SB 1 is summarized in Figures 4.11 and 4.12 as well as Table 4.3.

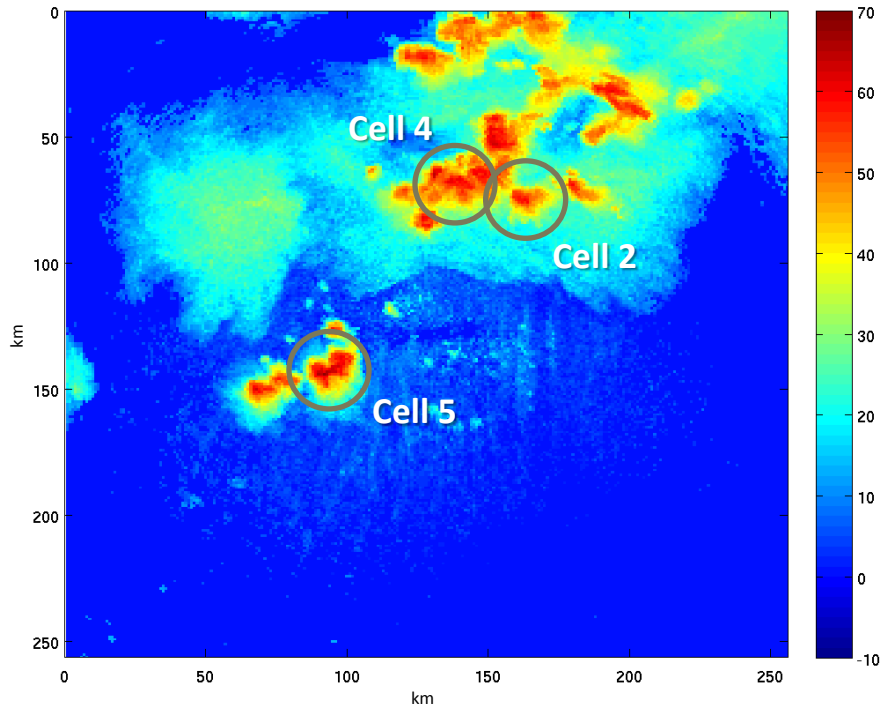


Figure 4.11: Composite reflectivity of SB 1 Cells 2, 4, and 5, respectively, as observed from (and centered upon) the Omaha, NE (KOAX) WSR-88D. Image valid at 2324 UTC 06/20/14.

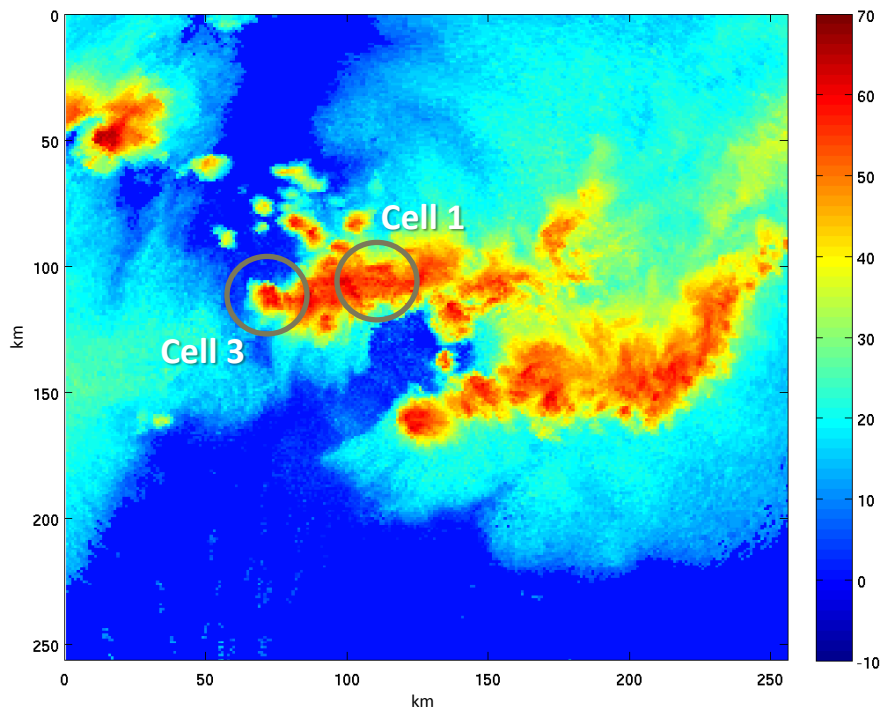


Figure 4.12: Composite reflectivity of SB 1 Cells 1, and 3, respectively, as observed from (and centered upon) the Omaha, NE (KOAX) WSR-88D. Image valid at 0224 UTC 06/21/14.

Table 4.3: A summary of the 5 most intense cells based on composite reflectivity from SB 1 as observed from the Pleasant Hill, MO (KEAX) radar. These 5 cells were used as the basis for studying SB 1. *Convergence values reported here are raw values.

	Cell 1	Cell 2	Cell 3	Cell 4	Cell 5
Time Frame (UTC)	0144 – 0241	2152 - 0008	0218 - 0402	2244 - 0025	2307 - 0019
Max Reflectivity (dBZ)	70.7	69.99	69.6	69.2	69.0
{time of occurrence (UTC)}	{0207}	{2203}	{0247}	{2301}	{2324}
Max Convergence* (10^{-3} s^{-1})	-4.03	-8.79	-3.16	-4.96	-4.66
{time of occurrence (UTC)}	(0150)	(2157)	(0258)	(0019)	(2324)

Again this analysis will begin by closely examining the most intense cell, Cell 1, which also had sufficient 0.5 km AGL data unlike some of the other surface-based cells in this dataset. Cell 1 initiated just west and slightly north of the KOAX radar site at about 0138 UTC 06/21. Thus, the environment which Cell 1 initiated within would be very well represented by the synoptic sounding taken from KOAX at 0000 UTC 06/21 which indicated over 4000 J/kg of CAPE (and no CIN) available for a surface-based parcel (Figure 4.9). This cell propagated northeast for approximately the first 25 minutes of its lifecycle before turning more easterly. During this same time, the cell quickly got surrounded by other areas of rapidly developing convection. The cell became no longer distinguishable within a convective line by around 0241 UTC 06/21, still just northwest of the KOAX radar site. The cell reached peak intensity at 0207 UTC 06/21 with a composite reflectivity value of 70 dBZ (Table 4.3). This was just prior to the cell beginning to take a more easterly trajectory.

The convergence column was initially a bit difficult to distinguish, with separated areas of convergence within the cell rather than a coherent column in the cell's first

observations at 0144 UTC 06/21. The convergence in the region of the updraft was more organized thereafter. Overall, a convergence column was detected (as defined in the methodology) in 8 of the 11 observed times for this cell. Some of the most coherent convergence columns were observed near the middle of the time frame for which this cell was analyzed (Figure 4.13).

As can be clearly seen in the convergence column observed from Cell 1 at 0218 UTC 06/21, the convergence column very coherently extends all the way to 0.5 km AGL. This was generally the case throughout the analyzed time frame for Cell 1. The only exception is at 0207 UTC when a convergence value of $-0.48 \cdot 10^{-3} \text{ s}^{-1}$ was observed at the base of the convergence column. This is important to note when considering observations of convergence at a single time. In other words, divergence can be observed at the base of a convergence column even in a case that should be surface-based.

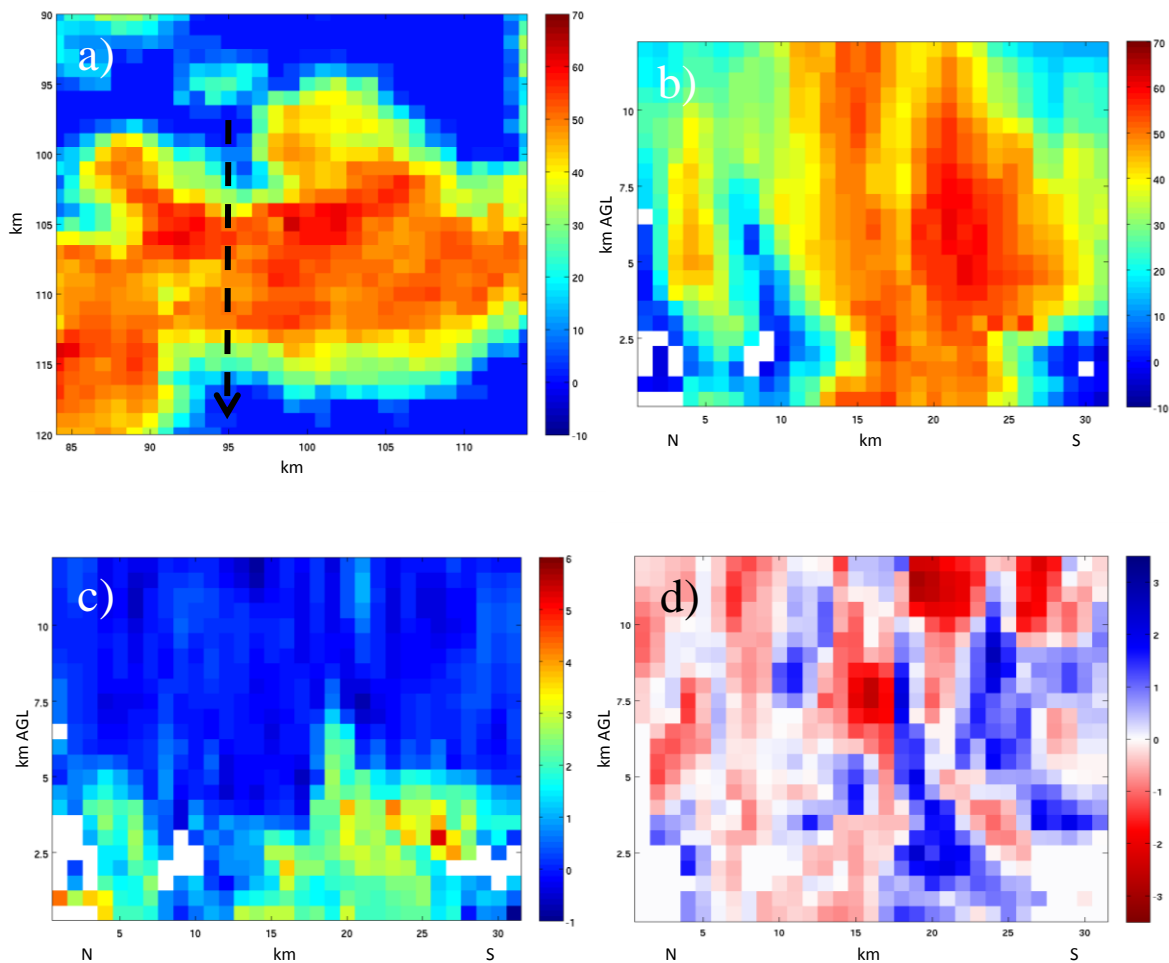


Figure 4.13: a) Plan view of reflectivity (dBZ) at 2 km AGL centered on SB 1 Cell 1. Dashed arrow indicates the location of the north (N)-to-south (S) cross-sections shown in b), c) and d). b) Reflectivity (dBZ) cross-section of SB 1 Cell 1. c) Z_{DR} (dB) cross-section of SB 1 Cell 1. d) Convergence (blue)/divergence (red) (10^{-3} s^{-1}) cross-section of SB 1 Cell 1. All valid at 0218 UTC 06/21/14.

When examining the average convergence column profile from all observed times in Cell 1, convergence values of around $0.4 \cdot 10^{-3} \text{ s}^{-1}$ occur in the lowest 1 km AGL (Figure 4.14). Obviously, convergence is expected to extend all the way to the surface in this case given the fact that SBCAPE is equivalent to MUCAPE, and thus the EILB is at the surface. The height of the maximum convergence generally occurred between 3 and 6 km AGL. A couple of outliers, particularly early in the cell's lifecycle, occurred within a secondary peak in convergence in the upper-levels of the cell. This corresponds well with

the overall average convergence column profile which clearly indicated a peak in convergence from 3.5 km to 4.5 km AGL, just less than a value of $1 \times 10^{-3} \text{ s}^{-1}$ (Figure 4.14).

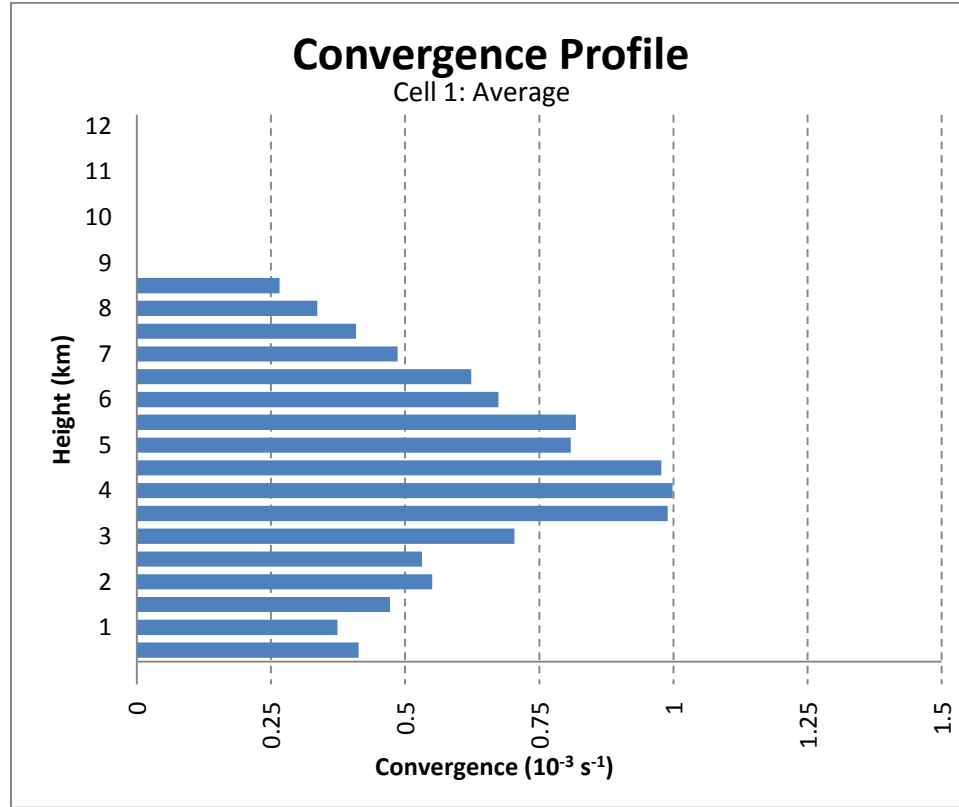


Figure 4.14: Average convergence with height for all times analyzed in SB 1 Cell 1.

An extension of this analysis to the remaining 4 cells examined for this case reveals fairly similar results to that observed within Cell 1. Only 2 of the remaining 4 cells (Cells 3 and 5) had sufficient data at 0.5 km AGL. Cell 2 had 0.5 km AGL data at only one time which was considered in the overall statistics but not individual statistics for Cell 2. The average convergence profile for Cells 3 and 5, respectively, indicated convergence that extended all the way to the near surface level (Figure 4.15), with values in excess of $0.3 \times 10^{-3} \text{ s}^{-1}$ (Figure 4.16). This is in agreement with the low-level convergence observed and discussed above with respect to Cell 1. Again, this result was expected given that no CIN existed within the observed proximity sounding for a parcel

lifted from the surface. Thus, convergence of parcels would be expected to extend all the way to the lowest levels observed by the radar within this event. This was also observed by a very coherent convergence column extending down to the near-surface level as well. Divergence occurred at 0.5 km AGL at only two other times in the other two cells observed with 0.5 km AGL radar data.

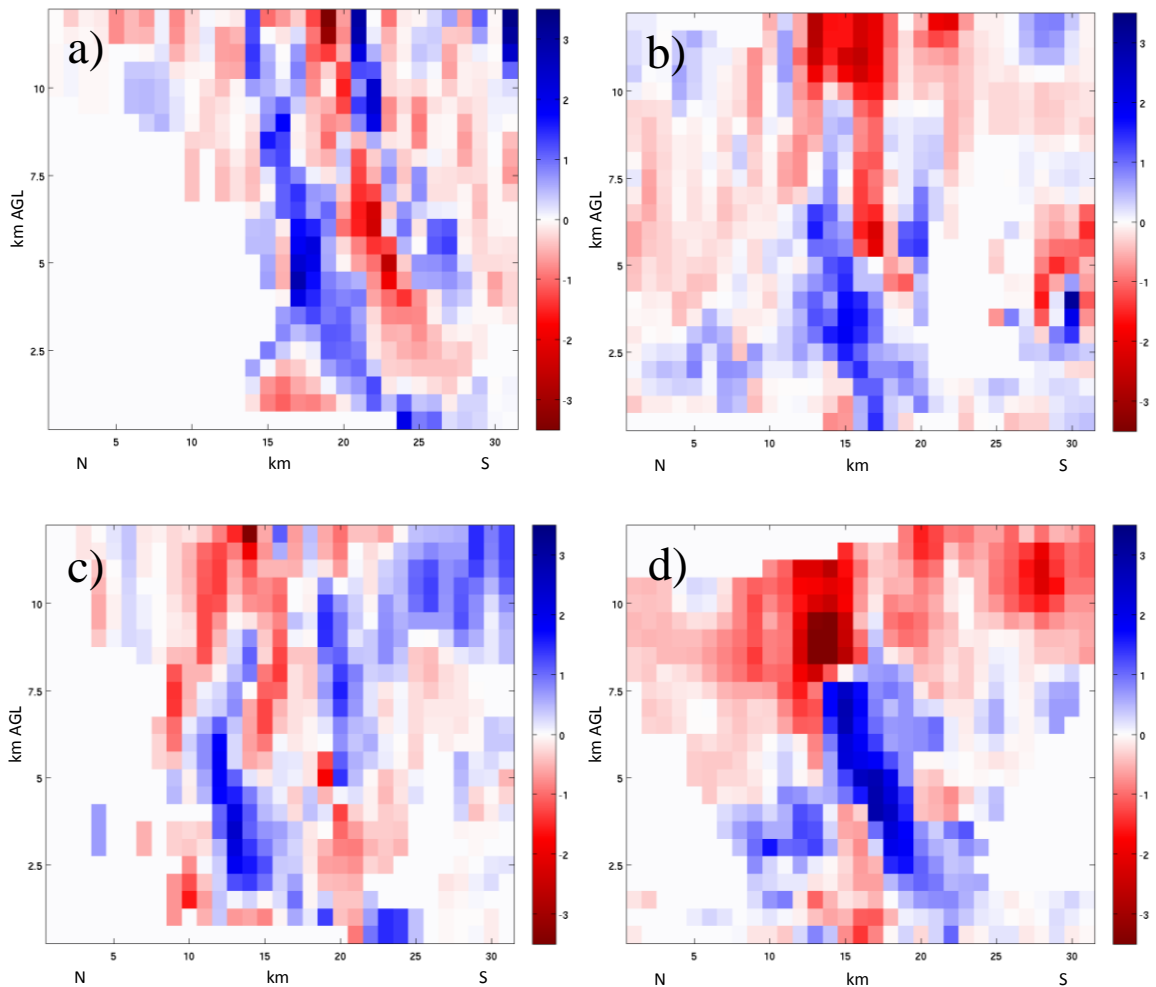


Figure 4.15: a) North (N)-to-South (S) Convergence (blue)/divergence (red) (10^{-3} s^{-1}) cross-section of SB 1 Cell 2 valid at 2221 UTC 06/20/14. b) Same as a) of SB 1 Cell 3 valid at 0322 UTC 06/21/14. c) Same as a) of SB 1 Cell 4 valid at 2307 UTC 06/20/14. d) Same as a) of SB 1 Cell 5 valid at 2352 UTC 06/20/14.

The height of maximum convergence from Cells 2-5 also corroborates that found in the analysis of Cell 1. The maximum convergence height consistently occurs within

the 3.5 km to 4.5 km AGL range (Figure 4.16). The only exception to this was within Cell 4 which displayed a maximum convergence height at 10 km AGL within the secondary upper-level peak of convergence. A secondary upper-level peak in convergence was also commonly observed in Cells 2-5. However, the low-level maximum convergence height for even Cell 4 fell within the 3.5 km to 4.5 km AGL range.

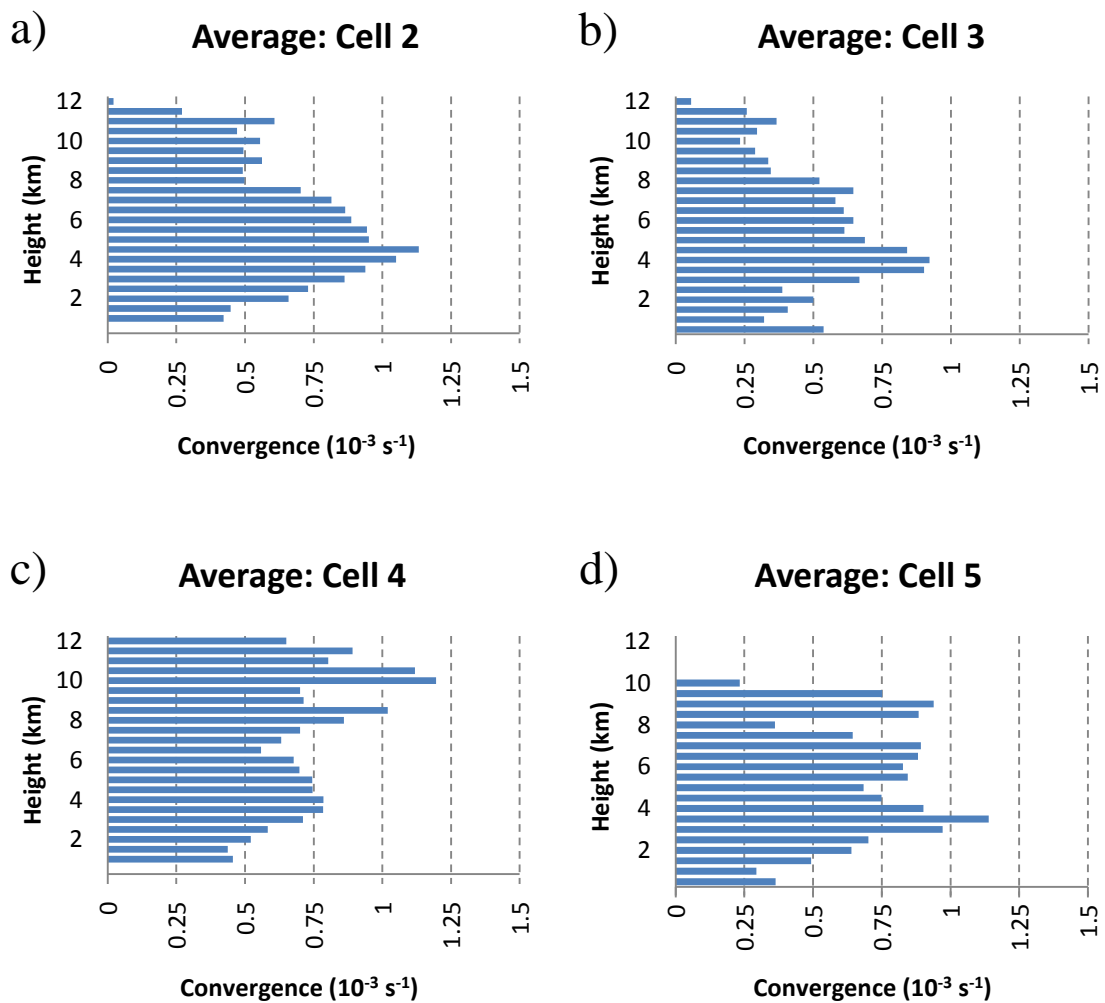


Figure 4.16: a) Average convergence with height for all times analyzed in SB 1 Cell 2. b) Average convergence with height for all times analyzed in SB 1 Cell 3. c) Average convergence with height for all times analyzed in SB 1 Cell 4. d) Average convergence with height for all times analyzed in SB 1 Cell 5.

In summary, the convergence column within the analyzed cells from this surface-based case do extend all the way to the 0.5 km AGL level with an overall average value of $0.43 \cdot 10^{-3} \text{ s}^{-1}$ with a standard deviation of $0.35 \cdot 10^{-3} \text{ s}^{-1}$. The range of average values for each individual convective cell was from $0.36 \cdot 10^{-3} \text{ s}^{-1}$ up to $0.54 \cdot 10^{-3} \text{ s}^{-1}$. However, values of divergence (negative convergence) can be observed at individual observed times for a particular cell. This seemed to be rare however, occurring only 12% of the time. Convergence values are then typically maximized within the 3.5 km to 4.5 km AGL range, with values generally from $0.8 \cdot 10^{-3} \text{ s}^{-1}$ to $1.20 \cdot 10^{-3} \text{ s}^{-1}$. A double peak in convergence is often observed with a secondary, upper-level, and typically lesser in magnitude peak occurring around 8 km to 11 km AGL.

4.4 Elevated versus Surface-Based Convergence Comparisons

When comparing the convergence column characteristics from the two analyzed cases, the elevated case (IOP 1) from 02 April 2014 and the surface-based case (SB 1) from 20 June 2014, there are several noteworthy similarities. First, both convective types, based on these two cases, on average reach maximum convergence values between $0.8 \cdot 10^{-3} \text{ s}^{-1}$ and $1.20 \cdot 10^{-3} \text{ s}^{-1}$. The height at which this maximum occurred (with respect to the low-level maximum) was also generally the same, although the range for the elevated case was somewhat larger, ranging from 2.5 km AGL to 5 km AGL. The low-level maximum convergence height was more consistent for the surface-based case, ranging on average from only 3.5 to 4.5 km AGL.

Furthermore, both cases typically showed a double peak in convergence values with height. As discussed in the individual cases, this weaker, upper-level peak usually

occurred a few kilometers above the low-level peak. This secondary upper-level convergence maximum typically occurred a bit higher in the surface-based case, 8 km AGL to 11 km AGL, than it did in the elevated case, 6 km AGL to 10 km AGL. This observation is likely due in part to the fact that the cells during IOP 1 were not as tall as those observed during SB 1. The difference in height for the upper-level convergence maximum is probably more attributable to environmental conditions on the particular day rather than a feature specific to either elevated or surface-based convection. However, to say either way is to go beyond the evidence in this study. The broader observation of a double peak in convergence within the convergence column in both convective types seems acceptable however.

With respect to the tilt or slope of the convergence column, it might seem based on qualitatively comparing those from IOP 1 (Figures 4.5d and 4.7) to those of SB 1 (Figures 4.13d and 4.15) that the columns in IOP 1 have a greater slope than those in the surface-based case. Given that the convergence column is a proxy for the updraft itself, any notable difference in the slope would seem to indicate a difference in the slope of the updraft. To make a quick quantitative comparison of this, the difference in the location in both the north-south and east-west direction was calculated between 0.5 km AGL and 6 km AGL. Using the differences in both respective directions, simple trigonometry was then used to calculate the slope. No respect to direction was necessarily given. However, in both IOP 1 and SB 1, the convergence column almost exclusively was tilted from south-to-north. Meanwhile, the convergence column typically had no tilt or a slight west-to-east tilt in both cases in the east-west direction. On average, the tilt of the cells in IOP 1 was slightly greater than that of SB 1, with average slopes of 6.85 km and 4.61 km both

over a change in height from 0.5 km AGL to 6 km AGL. It is likely that the slope of the updraft is largely governed by the synoptic setup on a particular day however. Thus, while certainly a result of interest, it is far from conclusive with regards to any difference in slope between elevated and surface-based convection.

The observation most key to the objectives of this study is with respect to any notable differences in convergence values at the base of the convergence column, particularly at 0.5 km AGL. Of course, it is hypothesized that due to an EILB that is above 0.5 km AGL in the elevated case, but extends to the surface in the surface-based case, that convergence values would be significantly less at the 0.5 km AGL level in the elevated case. Given that SBCAPE for the elevated case was 0 J/kg, no surface convergence due to the convective cell's inflow should be contributing to convergence at this level.

In an examination of 3-dimensional cross-sections through the observed cells, a somewhat more coherent convergence column extending to the surface within the cells observed in SB 1 can begin to be noted as compared to those from IOP 1 (Figures 4.5, 4.7, 4.13, and 4.15). That is to say that, at least qualitatively, there seems to be an extension of convergence of a greater magnitude all the way to the surface in the surface-based cells as compared to the elevated cells.

Quantitatively, the overall average for all analyzed cells in IOP 1, as described above, was only $0.13 \cdot 10^{-3} \text{ s}^{-1}$ with a variance of 0.11 (Table 4.4). Meanwhile, the overall average for all analyzed cells in SB 1 (which included no times from Cell 4 due to insufficient 0.5 km AGL data) was $0.45 \cdot 10^{-3} \text{ s}^{-1}$ with a variance of 0.12 (Table 4.4). To

determine if these averages differ statistically, a pooled T test, based on the assumptions that populations and variances from both cases are equal, was conducted. There are 23 values in the sample of elevated convection (IOP 1) and 26 values in the sample of surface-based convection (SB 1) based on all times sampled at 0.5 km AGL over the 5 cells for IOP 1 and the 4 cells for SB 1. This gives us 47 degrees of freedom (note the dependency issue discussed below). The test is based on a null hypothesis that the two averages are equal, $SB_{1,0.5} = IOP_{1,0.5}$, and a null hypothesis that the convergence at 0.5 km AGL is greater in the surface-based case compared to the elevated cases, $SB_{1,0.5} > IOP_{1,0.5}$. The result of the test was a test statistic of 3.214 and a P value less than 0.005. Thus, based on this testing method it can be concluded that the convergence values at 0.5 km AGL in the two cases are not the same (reject the null hypothesis) and that the surface-based case is higher at a 95% confidence interval. The difference can be seen graphically using a box-and-whisker plot comparing the two cases (Figure 4.17).

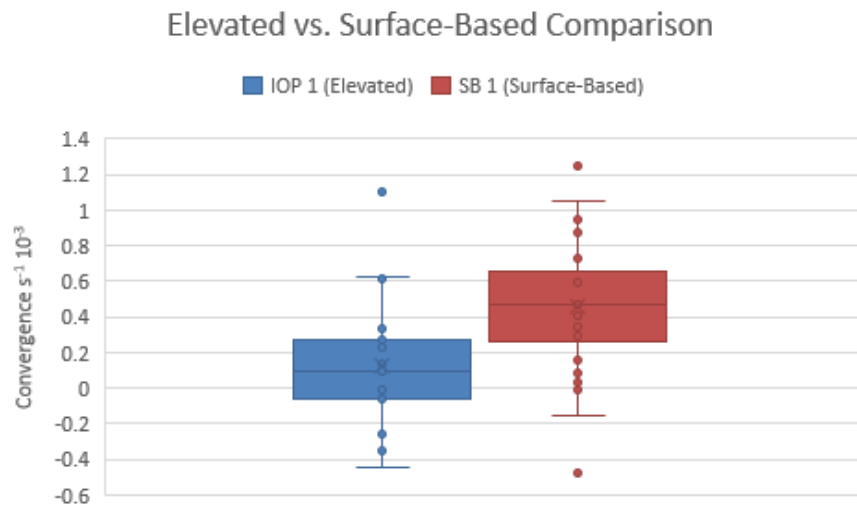


Figure 4.17: A box-and-whisker plot comparing 0.5 km AGL convergence from all cells analyzed in IOP 1 (elevated) to the same from all cells (with sufficient data) analyzed in SB 1 (surface-based). The box is indicative of the 25th and 75th percentiles, respectively. The ‘x’ marks the average value while the line near the center of the box is representative of the median value.

With regards to the statistical testing, each individual observed time was treated independently. However, given that each particular cell was observed at multiple times, each individual time is not truly independent. This is a concern with the statistical approach taken herein, especially with regard to the degrees of freedom, but finding a solution to this problem is somewhat difficult. Therefore, at least as an initial approach to statistical testing, each observed time for any of the observed cells was treated as independent. A more statistically robust approach that avoids this dependency issue should be considered in the future.

It should also be noted that this test is based on the event as a whole and not on any individual cell. As observed in both IOP 1 and SB 1, individual times observed in a cell's lifecycle, and even a cell's overall average, may differ from the typically observed convergence for convective cells during an event. This would likely be a lesser issue if cells were able to be observed at 0.5 km AGL for longer periods of time in order to average out varying degrees of noise apparent with the radar-derived convergence.

Table 4.4: Comparisons of the 0.5 km AGL convergence from all times in all analyzed cells from IOP 1 to the same for that of SB 1.

	Average Convergence at 0.5 km AGL	Variance of Convergence at 0.5 km AGL	Standard Deviation of Convergence at 0.5 km AGL
IOP 1	$0.13 \cdot 10^{-3} \text{ s}^{-1}$	0.11	$0.33 \cdot 10^{-3} \text{ s}^{-1}$
SB 1	$0.45 \cdot 10^{-3} \text{ s}^{-1}$	0.12	$0.35 \cdot 10^{-3} \text{ s}^{-1}$

Nevertheless, based on the comparisons of all cells observed in the 02 April 2014 elevated case (IOP 1) and the 20 June 2014 surface-based case (SB 1), it seems we can

provide statistical evidence that the radar-derived convergence below the EILB in an elevated case is lower than 0.5 km AGL convergence for a surface-based case. Given this, radar-derived convergence values from below the EILB may be able to provide further evidence in determining whether cells associated with a particular event are elevated or surface-based. This information would be particularly useful in cases that have greater values of MUCAPE even though some amount of SBCAPE exists. Of course, the EILB would need to be greater than at least 0.5 km for the radar to observe any potential difference, and even then, cells to be analyzed would need to be at a close proximity to the radar site.

4.5 Remaining IOP Convergence Column Summaries

An examination of the remaining IOPs will follow with the intention to see if the results from the comparison of the elevated 02 April 2014 case to the surface-based 20 June 2014 case can be applied to the other IOPs with more questionable degrees of elevated inflow based on skew-t charts alone. Since the two cases of comparison were approached as an entire event and not with respect to each individual convective cell, this same approach will initially be used for these cases. However, it is worthwhile to remember that based on the thermodynamic analysis alone, it is difficult to determine whether the case as a whole is either elevated or surface-based. Thus, considerations should be given to the possibility of both elevated and surface-based convective types within one case. Furthermore, a transition from one type to the other could also occur. This potential will be scrutinized more closely if overall case results seem to point to that possibility.

First, IOP 4 will be considered as it was expected to be predominately elevated, if not completely, based on observed soundings from the PRECIP field team in Chickasha, OK. As already briefly noted, while these observed soundings did indicate no SBCAPE available (Table 4.1), much of the convective event occurred a considerable distance further to the south. This would place much of the observed convection closer to the synoptic warm front and thus would likely increase the potential for SBCAPE to be introduced. Furthermore, it would almost certainly lower the EILB. With an EILB of around 0.9 km AGL in the 0400 and 0600 UTC 07/17/14 observed soundings, it is very reasonable to assume an EILB lowering to around the crucial observable height of 0.5 km AGL. Nevertheless, this is only a possibility and the observed radar results should give a clearer understanding of the convective nature of these cells.

The overall average profile for all cells observed in IOP 4 (Cell 5 did not have sufficient 0.5 km AGL data) follows the overall convergence column pattern to be expected based on the results from both IOP 1 and SB 1. That is, convergence reached a maximum at a height around 3.5 to 4 km AGL with a secondary peak in convergence around 8 km AGL (Table 4.5). With respect the 0.5 km AGL level, the average convergence value was $0.26 \cdot 10^{-3} \text{ s}^{-1}$. Furthermore, the range of averages for the 4 cells with 0.5 km AGL data only varied from $0.22 \cdot 10^{-3} \text{ s}^{-1}$ to $0.28 \cdot 10^{-3} \text{ s}^{-1}$ (Table 4.5), which is indicative of the overall consistency of the values in this case. Obviously, this value at 0.5 km AGL is higher than the average from IOP 1 but lower than that of SB 1. This value seems very reasonable given that the EILB is likely lower than IOP 1 but SBCAPE is probably limited, if available at all. Though the value seems very reasonable, it does little

to confirm either convective mode when comparing it to either IOP 1 or SB 1. However, the value is somewhat closer to the average of the observed purely elevated case (IOP 1).

Table 4.5: Summary of the convergence column within the analyzed cells from IOP 4.

	Cell 1	Cell 2	Cell 3	Cell 4	Cell 5	5 Cell Average
Average 0.5 km AGL Convergence (10^{-3} s^{-1})	0.27	0.28	0.22	0.27	-	0.26
Standard Deviation of Convergence at 0.5 km AGL (10^{-3} s^{-1})	0.36	0.60	0.30	0.32	-	0.39
Average Max Convergence (10^{-3} s^{-1})	0.85	0.92	0.98	0.91	0.73	0.77
Average Max Convergence Height (km AGL)	3.5	4.0	8.5	3.5	4.0	3.5

Based on the observed soundings from Nebraska City, NE, IOP 5 should also have been a predominately elevated case. While this case did have over 500 J/kg of SBCAPE in the observed 0000 UTC 05/06/15 sounding, the EILB was elevated to around 0.7-0.8 km AGL due to an inversion that resulted in 284 J/kg of SBCIN (Table 4.1). The CIN threshold based on the work of Thompson et al. (2007) was less than 250 J/kg. Moreover, the 0300 UTC 06/05 sounding had an EILB of roughly 2.7 km AGL. In fact, more of the convection analyzed in this case occurred in closer proximity to the 0300 UTC 06/05 sounding. However, observed soundings were taken a bit too far east with respect to where convection occurred and thus was analyzed. Nevertheless, it would seem plausible that lower values of convergence might extend higher into the lower atmosphere than in some of the other observed cases, including IOP 1. It is certainly

beneficial that this occurred with this case because low-level radar data from Hastings, NE (KUEX) was particularly limited for this case. In fact, no 0.5 km AGL radar data was available no matter the distance from the radar for this case. This was likely a result of some degree of subrefraction with respect to the radar beam.

Lower convergence values a bit higher into the lower atmosphere are, in fact, exactly what were generally observed. The overall average at 1 km AGL was only $0.12 \cdot 10^{-3} \text{ s}^{-1}$ (Table 4.6). Not only was this the lowest overall event observed average below the EILB, but it was also one of the most consistent with a standard deviation of only $0.25 \cdot 10^{-3} \text{ s}^{-1}$ at 1 km AGL. Values trended up from there, with a convergence value of $0.21 \cdot 10^{-3} \text{ s}^{-1}$ at 1.5 km AGL, still relatively low, and then up to $0.37 \cdot 10^{-3} \text{ s}^{-1}$ by 2 km AGL, a point which was nearing the observed EILB by the 0300 UTC 06/05 Nebraska City, NE sounding. Therefore, despite a lack of low-level radar data, the 1-1.5 km AGL data, which largely lie below the EILB based on the aforementioned observed sounding, seem to indicate that convection in this event was indeed primarily elevated.

Of note however, was the one deviant cell with respect to the average results. While the approach generally taken in this research has been to examine convective type with respect to the entirety of the event (i.e., all analyzed cells), it is worthwhile to note that Cell 4 had an average 1 km AGL convergence value of $0.65 \cdot 10^{-3} \text{ s}^{-1}$, a value considerably different than the event average of $0.12 \cdot 10^{-3} \text{ s}^{-1}$ (Table 4.6). It should be mentioned that the Cell 4 1 km AGL average convergence value is based on only the average of 3 observed times due to a lack of data however. Nevertheless, the 1.5 km AGL convergence for Cell 4 was also the highest of the 5 analyzed cells. What makes this observation of particular interest is that this was the only analyzed cell that occurred

before 0200 UTC. Cell 4’s lifecycle was from 0022-0142 UTC 06/05, making the observed sounding from 0000 UTC 06/05, with a much lower EILB (and below 1 km AGL) most representative of this cell. So, this seems to provide at least some indication that a change in EILB height could be observed within the convergence (divergence) radar product when the change is of considerable (at least > 0.5 km AGL) distance.

Table 4.6: Summary of the convergence column within the analyzed cells from IOP 5. The asterisk (*) highlights the change for this IOP of a low-level analyzed height of 1 km AGL rather than 0.5 km AGL (as in other cases) due to insufficient 0.5 km AGL data for IOP 5.

	Cell 1	Cell 2	Cell 3	Cell 4	Cell 5	5 Cell Average
Average 1 km* AGL Convergence (10^{-3} s^{-1})	0.05	0.14	-	0.65	-	0.12
Standard Deviation of Convergence at 1 km* AGL (10^{-3} s^{-1})	0.14	0.14	-	0.20	-	0.25
Average Max Convergence (10^{-3} s^{-1})	1.18	0.50	1.31	0.82	0.64	0.75
Average Max Convergence Height (km AGL)	4.0	4.5	7.5	6.0	3.5	6.0

IOPs 2 and 7 were similar in that considerable amounts of SBCAPE were available within some of the observed soundings (Table 4.1). For example, the observed sounding from Stuart, IA at 2200 UTC 06/04/14 had over 600 J/kg of SBCAPE, while the 0200 UTC 06/25/15 sounding from Bloomfield, IA had over 900 J/kg of SBCAPE. In fact, in the observed 2200 UTC 06/04/14 sounding from Stuart, IA, SBCAPE was equal to MUCAPE. Thus, certainly surface influences would be expected. Meanwhile, the

soundings from Bloomfield, IA in IOP 7 had EILBs that were all below 0.5 km, and therefore, observations from these cells would be expected to reflect a surface-based case.

Based on the overall cell averages at 0.5 km AGL (only Cells 1-3 had sufficient 0.5 km AGL data for IOP 2; all 5 cells had sufficient 0.5 km AGL data in IOP 7) these two cases did display the highest values of average convergence at 0.5 km AGL of the IOPs. IOP 2 had an average 0.5 km AGL convergence value of $0.46 \cdot 10^{-3} \text{ s}^{-1}$ (Table 4.7), while the same for IOP 7 was $0.40 \cdot 10^{-3} \text{ s}^{-1}$ (Table 4.8). Of course, these values very much correspond with the 0.5 km AGL average convergence value from SB 1 of $0.43 \cdot 10^{-3} \text{ s}^{-1}$. However, both IOPs 2 and 7 have very high overall standard deviations, indicative of a wide range of convergence values near the surface. Indeed, individual 0.5 km AGL convergence cell averages ranged from as high as $1.47 \cdot 10^{-3} \text{ s}^{-1}$ (Cell 2) to as low as $-0.02 \cdot 10^{-3} \text{ s}^{-1}$ (Cell 3) for IOP 2 (Table 4.7) and from $1.03 \cdot 10^{-3} \text{ s}^{-1}$ (Cell 5) to $0.14 \cdot 10^{-3} \text{ s}^{-1}$ (Cell 2) in IOP 7 (Table 4.8). This could indicate that these cases displayed a mix of both mostly elevated and mostly surface-based cells. Certainly, this does seem possible based upon the observed soundings from the two cases. Both cases displayed soundings with some amount of SBCAPE, but at the same time displayed higher amounts of MUCAPE (Table 4.1). Do these findings indicate that in such a situation, both convective types are conceivable? The data seems to indicate this possibility. Furthermore, this could even indicate that cells were transitioning from one convective type to another during the analyzed time frames.

Table 4.7: Summary of the convergence column within the analyzed cells from IOP 2.

	Cell 1	Cell 2	Cell 3	Cell 4	Cell 5	5 Cell Average
Average 0.5 km AGL Convergence (10^{-3} s^{-1})	0.26	1.47	-0.02	-	-	0.46
Standard Deviation of Convergence at 0.5 km AGL (10^{-3} s^{-1})	0.41	1.48	0.39	-	-	0.86
Average Max Convergence (10^{-3} s^{-1})	1.71	1.47	1.29	1.01	1.06	1.13
Average Max Convergence Height (km AGL)	7.0	0.5	8.0	10.0	5.5	5.5

Table 4.8: Summary of the convergence column within the analyzed cells from IOP 7.

	Cell 1	Cell 2	Cell 3	Cell 4	Cell 5	5 Cell Average
Average 0.5 km AGL Convergence (10^{-3} s^{-1})	0.23	0.14	0.37	0.35	1.03	0.40
Standard Deviation of Convergence at 0.5 km AGL (10^{-3} s^{-1})	0.40	0.29	0.91	0.71	0.76	0.71
Average Max Convergence (10^{-3} s^{-1})	1.13	1.37	1.19	1.41	1.45	1.13
Average Max Convergence Height (km AGL)	4.0	3.5	4.0	4.0	6.5	5.5

To further explore this possibility, a closer examination of Cell 1 from IOP 2 will be taken. This cell clearly developed and propagated southeastward through an environment undisturbed by any other convection for much of its analyzed lifecycle.

Thus, the observed sounding from Stuart, IA at 2200 UTC 06/04/14 (which was a pre-convective sounding) was likely very representative of the environment in which this thunderstorm was propagating, despite being somewhat displaced from the analyzed cell (which was in eastern Nebraska). Clearly, this sounding would indicate surface-based convection. However, the overall convergence average (based on 12 observations) for Cell 1 at 0.5 km AGL was only $0.26 \cdot 10^{-3} \text{ s}^{-1}$ (Table 4.7), a value somewhat lower than expected based on the aforementioned findings for surface-based convection. A closer inspection of the analyzed lifecycle of this particular convective cell seems to reveal two different phases of convergence at the near-surface level. In the 0.5 km AGL convergence time plot of Cell 1 (Figure 4.18), a decrease in convergence can be clearly observed at around 2058 UTC 06/04/14. In fact, the average convergence at 0.5 km AGL at and before this time was $0.50 \cdot 10^{-3} \text{ s}^{-1}$, a value which would seem to be more indicative of surface-based convection. Meanwhile, the same value for the available observed times after 2058 UTC 06/04/14 was only $-0.08 \cdot 10^{-3} \text{ s}^{-1}$. Thus, there seems to be a very clear difference in low-level convergence during the lifecycle of this cell, potentially indicating a change in convective mode.

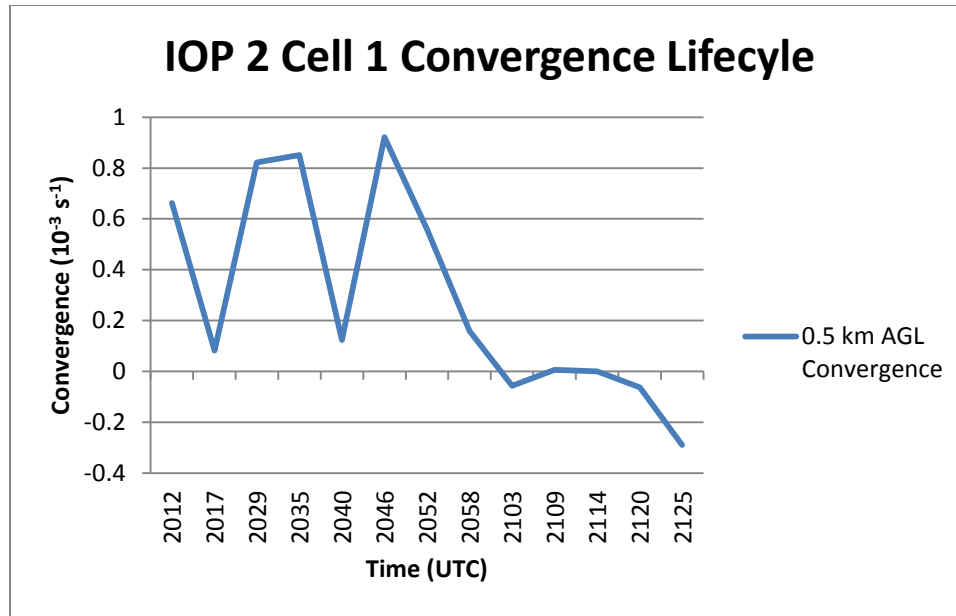


Figure 4.18: Summary of convergence at 0.5 km AGL over the lifecycle of IOP 2 Cell 1.

Radar reflectivity from this cell would also point to potential evidence of a transition around this time frame. Before 2058 UTC 06/04/14, the analyzed cell was a southeast propagating linear segment (Figure 4.19a, b). However, after this time, the analyzed portion of this cell is that of a developing comma head, which lags somewhat behind the leading edge of the convective line (Figure 4.19c, d, e). It seems very reasonable that this portion of the cell could have been more elevated given that the cold pool, likely along the leading edge of the convection, stabilized the lowest levels of the environment. The sounding from Stuart, IA observed at 0000 UTC 06/05/14, which had around 100 J/kg of SBCAPE but over 1000 J/kg (MUCAPE) when lifting from around 2.1 km AGL, provides further evidence for this possibility given that it was observed after initial convection.

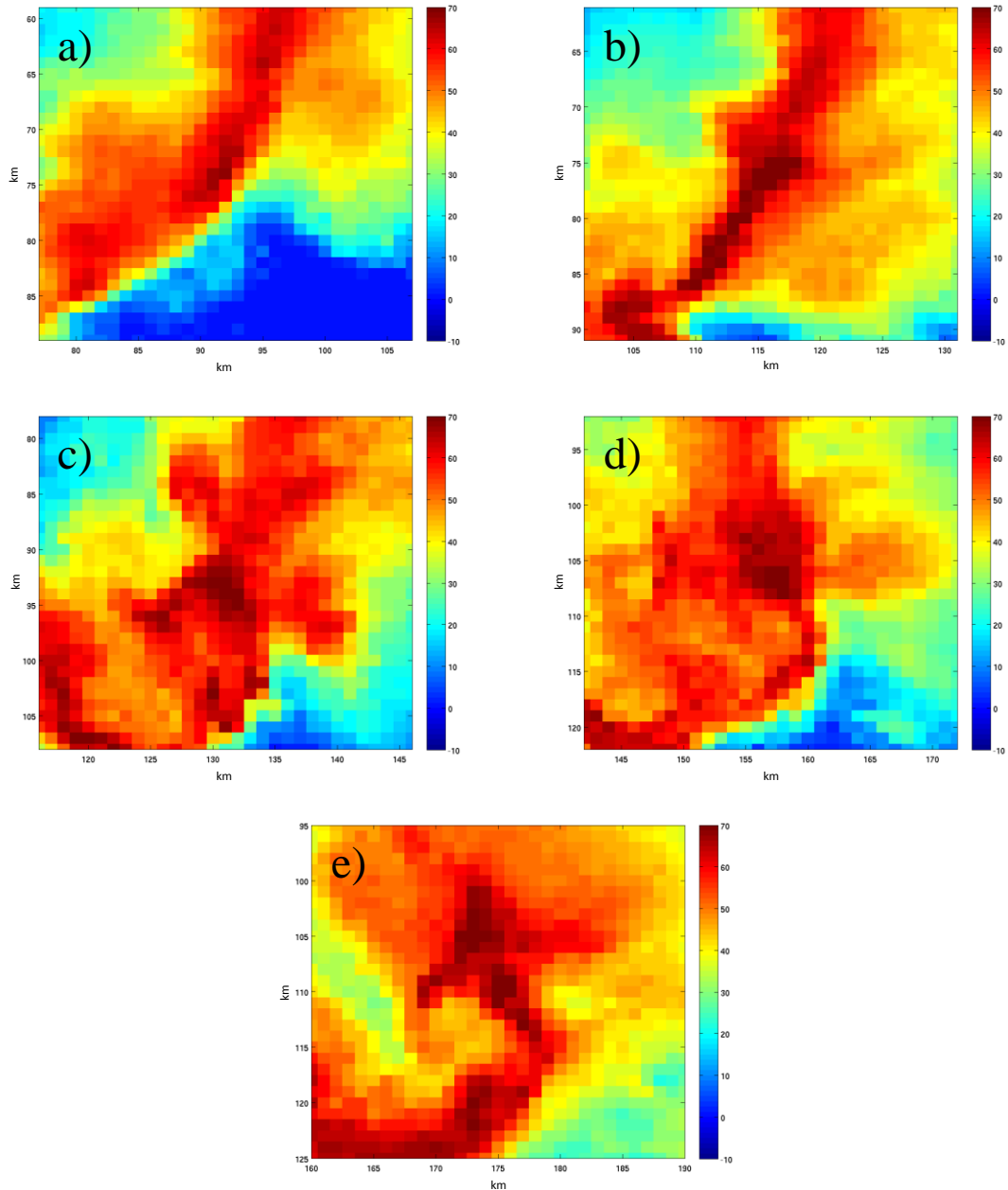


Figure 4.19: Radar reflectivity at 2 km AGL during the analyzed lifecycle of IOP 2 Cell 1 at a) 2029 UTC, b) 2046 UTC, c) 2103 UTC, d) 2125 UTC, and e) 2142 UTC all valid for 06/04/14.

In summary, there seems to be overall evidence pointing to the classification of a convective event as either elevated or surface-based using the low-level radar-derived convergence, particularly convergence near the base of the convergence column below the EILB. Data seems to indicate that at least IOP 5 was predominately an elevated

convective case given its convergence beneath the EILB was most similar to that of IOP 1. IOP 4 was also very similar to that of IOP 1 and was likely to some degree elevated. Higher low-level convergence values here may have been indicative of a lower EILB in this case as compared to IOP 1. Furthermore, it even seems possible that some surface-based parcels were ingested in some of these cells based upon the three-dimensional view of the convergence column.

Finally, it seems that cases in which sufficient SBCAPE is available, but a much higher amount of MUCAPE is available, such as was the case during portions of IOPs 2 and 7, that a mix of elevated and surface-based cells is possible. Moreover, a transition from one convective type to another could certainly be argued based on the data available from these two cases. While the classification of a convective type at a specific time within a cell's lifecycle, or even a particular cell as a whole, based on these results seems to be much less reliable than a basis for the classification of the entire event, there does appear to be some indication that such a cell-by-cell classification can be made. This would particularly be the case where near-surface convergence values are consistent for an extended period of time.

Chapter 5: Conclusions

5.1 Summary

Recent studies of elevated convection have resulted in a refined understanding of how to classify this convective type based on a thermodynamic profile. Most importantly, to state that convection is elevated when surface-based CAPE (SBCAPE) is available despite potentially much higher amounts of elevated or most unstable CAPE (MUCAPE) can be quite often flawed. This would be particularly so if the effective inflow layer, the layer of expected convective inflow based on thresholds of CAPE and CIN (>100 J/kg of CAPE and > -250 J/kg of CIN) as defined by Thompson et al. (2007), extends all the way to the surface or near-surface layer. Furthermore, events have been observed that transition from surface-based convection to elevated and vice-versa. Given that each convective type poses somewhat different severe hazards, it can be essential to know the convective type of an event or cell in order to better understand the severe risks associated therewith. Thus, this research explores an alternative method to using thermodynamic profiles alone to discriminate convection as either elevated or surface-based using dual-pol Doppler radar observations. Moreover, thermodynamic profiles are limited in time and are also modified by the convection itself. Thus, the real-time analysis of convective type that radar observations could provide would be quite useful.

Radar observations are the most reasonable method by which to observe individual convective cells from an event collectively in real-time with a great deal of resolution. However, radar studies specifically of elevated convective cells have been limited. Certainly no studies have approached the possible identification of a convective

cell as either elevated or surface-based using primarily radar observations. In order to determine between the two convective types by using radar observations, a differentiating feature would need to be observed in the data. With this in mind, the seemingly best radar product to use for this would be the convergence (divergence) product derived from Doppler detected velocities. The idea being that low-level convergence would be reduced, and potentially even divergent, in the near-surface layer because the convective cell would be rooted above a low-level stable layer preventing storm inflow from the near-surface layer. Meanwhile, inflow would extend all the way to the surface in a surface-based convective cell, and thus, near-surface convergence in a surface-based cell would be higher than near-surface convergence in an elevated convective cell.

In order to best assess this potential, the convergence for a given convective cell needed to be isolated to only the cell's convective updraft. This way, convergence within a convective cell present for various other reasons would not be a factor in the observed convergence, thereby allowing specifically convergence associated with the updraft to be assessed. Therefore, it was necessary to locate the convective updraft within any given cell. Much research has shown the effectiveness of relating a column of enhanced differential reflectivity (Z_{DR}) that extends above the environmental freezing level to be associated with the convective updraft (e.g., Illingworth et al. 1987, Brandes et al. 1995, Scharfenberg et al. 2005, Kumjian 2013). This is related to the lofting of supercooled water drops above the freezing level due to the vertical motions within the updraft. Thus, locating the Z_{DR} column is a good method for locating the convective updraft of a cell. Once the Z_{DR} column was located within a cell, the area of convergence located in generally this same location was assumed to be associated with the convective updraft.

This was subjectively confirmed when this region of convergence extended into the bounded weak echo region of some of the observed cells within this study. The bounded weak echo region is, of course, also associated with the convective updraft of particularly intense thunderstorms, most often supercells.

It was found that the area of convergence that was collocated with the Z_{DR} column also typically extended in a columnar fashion within the convective cell. Therefore, within this study a method by which we can locate the “convergence column” associated with the cell’s updraft was determined. This observation of a convergence column within the convective updraft is the first of its kind. It is then presumed that the convergence column, including its shape, depth and intensity can be used as a proxy to understand the shape, depth and intensity of the updraft.

In specific application to this research, the base of this convergence column, or the degree to which the convergence extends to the near-surface layer, is used as a proxy for determining the near-surface inflow. While certain other factors could contribute to near-surface convergence, the near-surface convergence should, at the very least, be reduced with the subtraction of surface inflow which should not be present in an elevated convective cell.

This idea was then applied to radar observations from the cases observed by the PRECIP field team which collected upper-air data via weather balloons. Thus, the thermodynamic environment was able to be directly compared to the radar observations of cells that were initially expected to be elevated. However, based on the aforementioned studies (e.g., Corfidi et al. 2008, Nowotarski et al. 2011, Schumacher

2015), the classification of some of these cases as elevated could be called into question. Using both NWS and PRECIP field team upper-air observations as well as NWS WSR-88D dual-pol Doppler radar, a known elevated case on 02 April 2014 and a known surface-based case on 20 June 2014 were used to compare the two convective types' convergence columns and specifically low-level convergence values. These results were then used in order to better understand the convective type associated with four other intense observation periods (IOPs) associated with the PRECIP effort.

5.2 Conclusions

Upper-air observations from the PRECIP field team during an event on 02 April 2014 in Clinton, MO were used to confirm that the event had no SBCAPE available. Meanwhile, around 1000 J/kg of MUCAPE was available in the observed environment. Given that no SBCAPE was available, this case could be assumed to be purely elevated with no surface inflow influences. Radar observations from the KEAX radar site confirmed convergence columns associated with convective cells that traversed the region. A 5 cell 0.5 km AGL convergence average (based on a 9 km² average) was 0.13 10⁻³ s⁻¹. Meanwhile, the same analysis was performed for a case from 20 June 2014 near Omaha, NE in which SBCAPE was equal to MUCAPE. In other words, convective cells from this case could be assumed to be purely surface-based. The same 0.5 km AGL convergence average located at the base of the updraft for 4 cells observed in this case was 0.45 10⁻³ s⁻¹. Using a pooled T test with a test statistic of 3.214 we can statistically say that the 0.5 km AGL convergence was higher in the surface-based case as compared to the purely elevated case at a 95% confidence interval.

Using the results from these two cases for comparison, the radar observations from four other PRECIP IOPs were examined. IOP 5, which had the highest observed effective inflow level base (EILB) of any representative sounding in all cases in the study, had the lowest near-surface convergence (which was at 1 km AGL for this case due to data limitations) average of only $0.12 \cdot 10^{-3} \text{ s}^{-1}$. IOP 4, which likely had an EILB around or potentially below the lowest observed level by the radar at 0.5 km AGL based on the observed soundings and the relative location of the convective cells, had a convergence average of $0.26 \cdot 10^{-3} \text{ s}^{-1}$. There were even periods within the lifecycle of Cell 1 of IOP 4 where the data suggested more of a surface-based influence. Thus, these radar observations of the convergence column are allowing the transition of a cell from one convective mode to another to be observed in near-real time. Furthermore, this is allowing the possibility to make a determination on convective type in an otherwise uncertain thermodynamic environment.

Meanwhile, the two cases that had observed EILBs that extended all the way to the near-surface layer, IOPs 2 and 7, respectively, had the highest observed 0.5 km AGL convergence averages among the IOPs at 0.46 and $0.40 \cdot 10^{-3} \text{ s}^{-1}$, respectively. Therefore, these cases certainly seem to have had surface-based influences despite being located north of a warm front in the synoptic cold sector. Furthermore, throughout much of both of these events, much higher amounts of MUCAPE was present compared to SBCAPE. The data also suggests that convective cells in these events may be a mix of both convective types. Moreover, the convective cells could also transition from one convective type to another, as seemed to be the case discussed in Section 4.4 with respect to Cell 1 of IOP 2.

Therefore, the overarching results of this research seem to indicate the following:

- Convergence associated with the convective updraft can be identified using radar by first locating the Z_{DR} column. Such an area of convergence is herein termed a convergence column.
- Low-level radar-observed convergence (particularly that below the EILB) is statistically reduced in association with elevated convective cells as compared to their surface-based counterparts.
- Convergence observed using radar can be used in association with representative thermodynamic diagrams of the environment to determine with greater certainty whether a collective group of convective cells are either elevated or surface-based or somewhere on a spectrum between.
- While the data herein makes it difficult to determine the convective mode on a cell-by-cell basis, there is evidence pointing to this possibility. With this comes the potential to observe the transition of a convective cell from one convective type to another.
- Events with some amount of SBCAPE but higher amounts of MUCAPE seem to be a mix of both convective types with the potential for individual cells to transition between the two types.
- Convective events occurring north of synoptic warm fronts, and thus within the “cold sector,” should not necessarily be assumed to be elevated.

5.3 Future Work

First, at many points within this work, further substantiating data would be welcomed. An extension to more than one purely elevated case would be advantageous in order to better understand the range in which the near-surface convergence values would occur. The same could also be said with respect to surface-based cases. With a better established dataset, these results could be much more confidently accepted. Furthermore, at many points within the dataset used in this study, 0.5 km AGL data was insufficient for the analyzed cells. An approach that used only cells that had sufficient 0.5 km AGL data would likely produce more robust results.

Nevertheless, given that evidence throughout this study continually points to a noticeable difference in the near-surface convergence, extensions outside of more data certainly seem worthwhile. First, better efforts to confirm the ability to consistently note differences in near-surface convergence on a cell-by-cell basis as opposed to an overall event basis is needed. In cases where a mix of both convective types is likely to occur, such as cases similar to IOPs 2 and 7 examined herein, there is a need to make more certain classifications of particular cells in order to best assess potential severe hazards as well as other factors such as cell longevity and propagation. Moreover, if a cell-by-cell determination can be made, this information could then be more readily applied in real-time observations which would be especially useful for potentially transitioning cells from one convective type to another. Operationally, if more consistent results per cell and individual times observed within a cell's lifecycle can be achieved, a radar tool monitoring the near-surface convergence could make one more aware of a cell's convective type and whether a transition may be occurring.

Some of the need for more consistent results on an individual time basis could be solved by a better algorithm to locate the Z_{DR} column from within the cell. As noted in Section 3.5.1, an improvement could certainly be made given the set levels from which the Z_{DR} column is selected from. Since the environmental freezing level changes from event-to-event, a more flexible approach to the layer from which the Z_{DR} column would be located would be best. The author is certain that the misidentification of the Z_{DR} column likely led to some inconsistent convergence values within the study. The data extracted from the convergence column is only as good as the proper locating of the Z_{DR} column given their general collocation. The best results in this study were derived from times when the Z_{DR} column was very clearly properly located.

Finally, with respect to the identification of the convergence column, a completely new concept introduced here, the potential research extensions are many. Since this column is a proxy for the updraft of the cell, it is very plausible that a vertically integrated value for the convergence column may have some applicability to the overall intensity of the cell. As the convergence column deepens or becomes more intense, does the overall intensity of the cell via reflectivity follow suite? The reverse of this idea with regards to a weakening cell could also be explored. Moreover, how does the convergence column magnitude and height relate to hail potential? One would hypothesize that a strong region within the convergence column extending well above the freezing level could potentially be a sign of hail growth. Furthermore, as demonstrated in Section 4.4, characteristics of the updraft such as slope can be explored. There is undoubtedly more to be examined with respect to such characteristics. These are only a few initial and limited potential uses of the convergence column.

Lastly, a couple of interesting convergence column patterns were found during this study that could use further exploration. In many cases, a convergence column wishbone feature appeared in the 3-dimensional cross-sections, with an area of divergence near the surface creating the wishbone shape (Appendix B). This area of divergence was typically located at the base of the convective downdraft based on an assessment of reflectivity. Thus, this pattern within the convergence (divergence) product is presumably indicative of some degree of outflow winds in association with the convective downdraft. And finally, observed with a supercell that occurred during IOP 7 in Iowa, was the descending convergence column in association with the rear flank downdraft of the supercell (Appendix B). This identification was made based on a strong area of coherent convergence extending to the surface near the rear of the cell that was not collocated with the Z_{DR} column. A second, ascending convergence column, if you will, was also identified associated with the Z_{DR} column/updraft as was typically the case in this study. Certainly it would seem that there is further potential research possibilities related to the descending convergence column and rear flank downdrafts within thunderstorms.

Appendix A

The following is an excerpt of MATLAB code that locates the Z_{DR} column as described in the Chapter 3.

```
for i=1:10
    lszheight={1:i};
end

for ls = 1:25
    xcount=0;
    for lxs = xlmin:xlmax
        xcount = xcount+1;
        ycount=0;
        for lsy = ylmin:ylmax
            ycount = ycount+1;
            lszheight{ls,1}(xcount,ycount)=zheight{ls,1}(lxs,
            lsy);
        end
    end
end

for lxs = xlmin:xlmax
    xcount = xcount+1;
    ycount=0;
    for lsy = ylmin:ylmax
        ycount = ycount+1;
        lszcomp(xcount,ycount)=zcomp(lxs,lsy);
    end
end

maxzc{1,b} = lszcomp(1,1);

for mzcX = 31:62
    for mzcY = 1:31
        if lszcomp(mzcX,mzcY)>maxzc{1,b}
            maxzc{1,b} = lszcomp(mzcX,mzcY);
        end
    end
end

for hh = 1:16
    z3by3{hh,1}=zeros(lsm,lsn);
    avgz3by3{hh,1}=zeros(lsm,lsn);
    for o=2:(31-1)
        for l=2:(31-1)
            z3by3{hh,1}(o,l)=(lszheight{hh,1}(o-1,l-1))
            +(lszheight{hh,1}(o,l-1))+(lszheight{hh,1}(o+1,l-
```

```

1))+(lszheight{hh,1}(o-1,1))
+(lszheight{hh,1}(o,1))+(lszheight{hh,1}
(o+1,1))+(lszheight{hh,1}(o-1,l+1))
+(lszheight{hh,1}(o,l+1))+(lszheight{hh,1}
(o+1,l+1));
avgz3by3{hh,1}=(z3by3{hh,1}./9);
end
end

%maxofavg{1,b}(1,1)=starttime;

maxofavgz{1,b}(hh,1)=avgz3by3{hh,1}(1,1);
for o=12:22
    for l=12:22
        if (avgz3by3{hh,1}(o,l)>maxofavgz{1,b}(hh,1))
            maxofavgz{1,b}(hh,1)=avgz3by3{hh,1}(o,l);
            maxofavgz{1,b}(hh,2)=o;
            maxofavgz{1,b}(hh,3)=l;
        end
    end
end
end

maxz{1,b} = maxofavgz{1,b}(1,1);
for mz = 1:16
    if maxofavgz{1,b}(mz,1) > maxz{1,b}
        maxz{1,b}=maxofavgz{1,b}(mz,1);
    end
end

for i=1:10
    lszdrheight={1:i};
end

for ls = 1:25
    xcount=0;
    for lsx = xmin:xmax
        xcount = xcount+1;
        ycount=0;
        for lsy = ymin:ymax
            ycount = ycount+1;
            lszdrheight{ls,1}(xcount,ycount)=
            zdrheight{ls,1}(lsx,lsy);
        end
    end
end

lszdrheight=lszdrheight;

for hh = 1:16
    zdr3by3{hh,1}=zeros(lsm,lsn);
    avgzdr3by3{hh,1}=zeros(lsm,lsn);

```

```

for o=2:(31-1)
    for l=2:(31-1)
        if lszheight{hh,1}(o,l)>25
            if lszheight{hh,1}(o-1,l-1)<25
                lszdrheight{hh,1}(o-1,l-1)=0;
            end

            if lszheight{hh,1}(o,l-1)<25
                lszdrheight{hh,1}(o,l-1)=0;
            end

            if lszheight{hh,1}(o+1,l-1)<25
                lszdrheight{hh,1}(o+1,l-1)=0;
            end

            if lszheight{hh,1}(o-1,l)<25
                lszdrheight{hh,1}(o-1,l)=0;
            end

            if lszheight{hh,1}(o+1,l)<25
                lszdrheight{hh,1}(o+1,l)=0;
            end

            if lszheight{hh,1}(o-1,l+1)<25
                lszdrheight{hh,1}(o-1,l+1)=0;
            end

            if lszheight{hh,1}(o,l+1)<25
                lszdrheight{hh,1}(o,l+1)=0;
            end

            if lszheight{hh,1}(o+1,l+1)<25
                lszdrheight{hh,1}(o+1,l+1)=0;
            end

            zdr3by3{hh,1}(o,l)=(lszdrheight{hh,1}(o-1,l-1))+lszdrheight{hh,1}(o,l-1))
            +(lszdrheight{hh,1}(o+1,l-1))
            +(lszdrheight{hh,1}(o-1,l))
            +(lszdrheight{hh,1}(o,l))
            +(lszdrheight{hh,1}(o+1,l))
            +(lszdrheight{hh,1}(o-1,l+1))
            +(lszdrheight{hh,1}(o,l+1))
            +(lszdrheight{hh,1}(o+1,l+1));
            avgzdr3by3{hh,1}=(zdr3by3{hh,1}./9);
        end
    end
end

%maxofavg{1,b}(1,1)=starttime;

maxofavg{2,b}(hh,1)=avgzdr3by3{hh,1}(1,1);

```

```

        for o=12:22
            for l=12:22
                if (avgzdr3by3{hh,1}(o,l)>maxofavg{2,b}(hh,1))
                    maxofavg{2,b}(hh,1)=avgzdr3by3{hh,1}(o,l);
                    maxofavg{2,b}(hh,2)=o;
                    maxofavg{2,b}(hh,3)=l;
                end
            end
        end
    end
end

lszdrheight=lszdrheighth;

zdrcheckx=0;
zdrchecky=0;
zdrcheckx6=0;
zdrchecky6=0;

if abs(maxofavg{2,b}(6,2)-maxofavg{2,b}(5,2))<3
    zdrcheckx=zdrcheckx+1;
end

if abs(maxofavg{2,b}(7,2)-maxofavg{2,b}(5,2))<3
    zdrcheckx=zdrcheckx+1;
end

if abs(maxofavg{2,b}(8,2)-maxofavg{2,b}(5,2))<3
    zdrcheckx=zdrcheckx+1;
end

if abs(maxofavg{2,b}(6,3)-maxofavg{2,b}(5,3))<3
    zdrchecky=zdrchecky+1;
end

if abs(maxofavg{2,b}(7,3)-maxofavg{2,b}(5,3))<3
    zdrchecky=zdrchecky+1;
end

if abs(maxofavg{2,b}(8,3)-maxofavg{2,b}(5,3))<3
    zdrchecky=zdrchecky+1;
end

if zdrcheckx>1 && zdrchecky>1
    zdrcol{1,b}(1,1)=maxofavg{2,b}(5,2);
    zdrcol{1,b}(1,2)=maxofavg{2,b}(5,3);
end

if abs(maxofavg{2,b}(7,2)-maxofavg{2,b}(6,2))<3
    zdrcheckx6=zdrcheckx6+1;
end

if abs(maxofavg{2,b}(8,2)-maxofavg{2,b}(6,2))<3

```

```

        zdrcheckx6=zdrcheckx6+1;
end

if abs(maxofavg{2,b}(9,2)-maxofavg{2,b}(6,2))<3
    zdrcheckx6=zdrcheckx6+1;
end

if abs(maxofavg{2,b}(7,3)-maxofavg{2,b}(6,3))<3
    zdrchecky6=zdrchecky6+1;
end

if abs(maxofavg{2,b}(8,3)-maxofavg{2,b}(6,3))<3
    zdrchecky6=zdrchecky6+1;
end

if abs(maxofavg{2,b}(9,3)-maxofavg{2,b}(6,3))<3
    zdrchecky6=zdrchecky6+1;
end

if (zdrcheckx<1 && zdrchecky<1) && (zdrcheckx6<1 && zdrchecky6<1)
    msg = 'Error. No ZDR Column.';
    error(msg)
end

if (zdrcheckx + zdrchecky) > (zdrcheckx6 + zdrchecky6)
    zdrcol{1,b}(1,1)=maxofavg{2,b}(5,2);
    zdrcol{1,b}(1,2)=maxofavg{2,b}(5,3);
    zch=5;
end

if (zdrcheckx + zdrchecky) == (zdrcheckx6 + zdrchecky6)
    if maxofavg{2,b}(5,1)>maxofavg{2,b}(6,1)
        zdrcol{1,b}(1,1)=maxofavg{2,b}(5,2);
        zdrcol{1,b}(1,2)=maxofavg{2,b}(5,3);
        zch=5;
    end

    if maxofavg{2,b}(6,1)>maxofavg{2,b}(5,1)
        zdrcol{1,b}(1,1)=maxofavg{2,b}(6,2);
        zdrcol{1,b}(1,2)=maxofavg{2,b}(6,3);
        zch=6;
    end
end

if (zdrcheckx + zdrchecky) < (zdrcheckx6 + zdrchecky6)
    zdrcol{1,b}(1,1)=maxofavg{2,b}(6,2);
    zdrcol{1,b}(1,2)=maxofavg{2,b}(6,3);
    zch=6;
end

```

The following is an excerpt of MATLAB code that extracts the values and location of the convergence column based upon the starting location at the base of the Z_{DR} column as described in Chapter 3.

```

maxdiv{1,b}(1,1)=lsdivheight{1,1}(zdrcol{1,b}(1,1),zdrcol{1,b}(1,2));

maxcon{1,b}(1,1)=lsdivheight{1,1}(zdrcol{1,b}(1,1),zdrcol{1,b}(1,2));
maxdiv{1,b}(1,2)=1;
maxcon{1,b}(1,2)=1;
if isnan(maxdiv{1,b}(1,1))
    maxdiv{1,b}(1,1)=0;
end
if isnan(maxcon{1,b}(1,1))
    maxcon{1,b}(1,1)=0;
end

ccolmx{zch,b}=lsdivheight{zch,1}(zdrcol{1,b}(1,1),zdrcol{1,b}(1,2));
ccolmx{zch,b}(1,2)=zdrcol{1,b}(1,1);
ccolmx{zch,b}(1,3)=zdrcol{1,b}(1,2);

if isnan(lsdivheight{zch,1}(zdrcol{1,b}(1,1)-1,zdrcol{1,b}(1,2)-1))

else if ccolmx{zch,b}(1,1)>lsdivheight{zch,1}(zdrcol{1,b}(1,1)-1,zdrcol{1,b}(1,2)-1)
    ccolmx{zch,b}(1,1)=lsdivheight{zch,1}(zdrcol{1,b}(1,1)-1,zdrcol{1,b}(1,2)-1);
    ccolmx{zch,b}(1,2)=zdrcol{1,b}(1,1)-1;
    ccolmx{zch,b}(1,3)=zdrcol{1,b}(1,2)-1;
end

end

if isnan(lsdivheight{zch,1}(zdrcol{1,b}(1,1)-1,zdrcol{1,b}(1,2)))

else if ccolmx{zch,b}(1,1)>lsdivheight{zch,1}(zdrcol{1,b}(1,1)-1,zdrcol{1,b}(1,2))
    ccolmx{zch,b}(1,1)=lsdivheight{zch,1}(zdrcol{1,b}(1,1)-1,zdrcol{1,b}(1,2));
    ccolmx{zch,b}(1,2)=zdrcol{1,b}(1,1)-1;
    ccolmx{zch,b}(1,3)=zdrcol{1,b}(1,2);
end

end
if isnan(lsdivheight{zch,1}(zdrcol{1,b}(1,1)-1,zdrcol{1,b}(1,2)+1))

```

```

else if ccolmx{zch,b}(1,1)>lsdivheight{zch,1}(zdrcol{1,b}(1,1)-1,
zdrcol{1,b}(1,2)+1)
ccolmx{zch,b}(1,1)=lsdivheight{zch,1}(zdrcol{1,b}(1,1)-1,
zdrcol{1,b}(1,2)+1);
ccolmx{zch,b}(1,2)=zdrcol{1,b}(1,1)-1;
ccolmx{zch,b}(1,3)=zdrcol{1,b}(1,2)+1;
end
end

if isnan(lsdivheight{zch,1}(zdrcol{1,b}(1,1), zdrcol{1,b}(1,2)-
1))

else if ccolmx{zch,b}(1,1)>lsdivheight{zch,1}(zdrcol{1,b}(1,1),
zdrcol{1,b}(1,2)-1)
ccolmx{zch,b}(1,1)=lsdivheight{zch,1}(zdrcol{1,b}(1,1),
zdrcol{1,b}(1,2)-1);
ccolmx{zch,b}(1,2)=zdrcol{1,b}(1,1);
ccolmx{zch,b}(1,3)=zdrcol{1,b}(1,2)-1;
end
end

if isnan(lsdivheight{zch,1}(zdrcol{1,b}(1,1), zdrcol{1,b}(1,2)))

else if ccolmx{zch,b}(1,1)>lsdivheight{zch,1}(zdrcol{1,b}(1,1),
zdrcol{1,b}(1,2))
ccolmx{zch,b}(1,1)=lsdivheight{zch,1}(zdrcol{1,b}(1,1),
zdrcol{1,b}(1,2));
ccolmx{zch,b}(1,2)=zdrcol{1,b}(1,1);
ccolmx{zch,b}(1,3)=zdrcol{1,b}(1,2);
end
end

if isnan(lsdivheight{zch,1}(zdrcol{1,b}(1,1),
zdrcol{1,b}(1,2)+1))

else if ccolmx{zch,b}(1,1)>lsdivheight{zch,1}(zdrcol{1,b}(1,1),
zdrcol{1,b}(1,2)+1)
ccolmx{zch,b}(1,1)=lsdivheight{zch,1}(zdrcol{1,b}(1,1),
zdrcol{1,b}(1,2)+1);
ccolmx{zch,b}(1,2)=zdrcol{1,b}(1,1);
ccolmx{zch,b}(1,3)=zdrcol{1,b}(1,2)+1;
end
end

if isnan(lsdivheight{zch,1}(zdrcol{1,b}(1,1)+1, zdrcol{1,b}(1,2)-
1))

else if ccolmx{zch,b}(1,1)>lsdivheight{zch,1}(zdrcol{1,b}(1,1)+1,
zdrcol{1,b}(1,2)-1)

```

```

        ccolmx{zch,b}(1,1)=lsdivheight{zch,1}(zdrcol{1,b}(1,1)+1,
        zdrcol{1,b}(1,2)-1);
        ccolmx{zch,b}(1,2)=zdrcol{1,b}(1,1)+1;
        ccolmx{zch,b}(1,3)=zdrcol{1,b}(1,2)-1;
    end
end

if isnan(lsdivheight{zch,1}(zdrcol{1,b}(1,1)+1,
    zdrcol{1,b}(1,2)))

else if ccolmx{zch,b}(1,1)>lsdivheight{zch,1}(zdrcol{1,b}(1,1)+1,
    zdrcol{1,b}(1,2))
    ccolmx{zch,b}(1,1)=lsdivheight{zch,1}(zdrcol{1,b}(1,1)+1,
    zdrcol{1,b}(1,2));
    ccolmx{zch,b}(1,2)=zdrcol{1,b}(1,1)+1;
    ccolmx{zch,b}(1,3)=zdrcol{1,b}(1,2);
end

end

if isnan(lsdivheight{zch,1}(zdrcol{1,b}(1,1)+1,
    zdrcol{1,b}(1,2)+1))

else if ccolmx{zch,b}(1,1)>lsdivheight{zch,1}(zdrcol{1,b}(1,1)+1,
    zdrcol{1,b}(1,2)+1)
    ccolmx{zch,b}(1,1)=lsdivheight{zch,1}(zdrcol{1,b}(1,1)+1,
    zdrcol{1,b}(1,2)+1);
    ccolmx{zch,b}(1,2)=zdrcol{1,b}(1,1)+1;
    ccolmx{zch,b}(1,3)=zdrcol{1,b}(1,2)+1;
end

end

xmax=ccolmx{zch,b}(1,2);
ymax=ccolmx{zch,b}(1,3);
nanc=0;
ccolmxsum{zch,b}=lsdivheight{zch,1}(xmax,ymax);

if isnan(lsdivheight{zch,1}(xmax-1,ymax))
    nanc=nanc+1;
else
    ccolmxsum{zch,b}=ccolmxsum{zch,b}+lsdivheight{zch,1}(xmax-
    1,ymax);
end

if isnan(lsdivheight{zch,1}(xmax-1,ymax-1))
    nanc=nanc+1;
else
    ccolmxsum{zch,b}=ccolmxsum{zch,b}+lsdivheight{zch,1}(xmax-
    1,ymax-1);
end

if isnan(lsdivheight{zch,1}(xmax,ymax-1))
    nanc=nanc+1;

```

```

else
    ccolmxsum{zch,b}=ccolmxsum{zch,b}+lsdivheight{zch,1}(xmax,y
max-1);
end

if isnan(lsdivheight{zch,1}(xmax+1,ymax))
    nanc=nanc+1;
else
    ccolmxsum{zch,b}=ccolmxsum{zch,b}+lsdivheight{zch,1}(xmax+1
,ymax);
end

if isnan(lsdivheight{zch,1}(xmax+1,ymax+1))
    nanc=nanc+1;
else
    ccolmxsum{zch,b}=ccolmxsum{zch,b}+lsdivheight{zch,1}(xmax+1
,ymax+1);
end

if isnan(lsdivheight{zch,1}(xmax,ymax+1))
    nanc=nanc+1;
else
    ccolmxsum{zch,b}=ccolmxsum{zch,b}+lsdivheight{zch,1}(xmax,y
max+1);
end

if isnan(lsdivheight{zch,1}(xmax-1,ymax+1))
    nanc=nanc+1;
else
    ccolmxsum{zch,b}=ccolmxsum{zch,b}+lsdivheight{zch,1}(xmax-
1,ymax+1);
end

if isnan(lsdivheight{zch,1}(xmax+1,ymax-1))
    nanc=nanc+1;
else
    ccolmxsum{zch,b}=ccolmxsum{zch,b}+lsdivheight{zch,1}(xmax+1
,ymax-1);
end

if nanc==0;
    ccolmxavg{zch,b}=(ccolmxsum{zch,b}/9);
end
if nanc==1;
    ccolmxavg{zch,b}=(ccolmxsum{zch,b}/8);
end
if nanc==2;
    ccolmxavg{zch,b}=(ccolmxsum{zch,b}/7);
end
if nanc==3;
    ccolmxavg{zch,b}=(ccolmxsum{zch,b}/6);
end

```

```

if nanc>3;
    ccolmxsum{zch,b}=NaN;
    ccolmxavg{zch,b}=NaN;
end

if zch == 5
    divdwn=4;
    while(divdwn>0)
        a1=ccolmx{divdwn+1,b}(1,2);
        a2=ccolmx{divdwn+1,b}(1,3);
        ccolmx{divdwn,b}(1,1)=lsdivheight{divdwn,1}(a1, a2);
        ccolmx{divdwn,b}(1,2)=a1;
        ccolmx{divdwn,b}(1,3)=a2;

        if isnan(lsdivheight{divdwn,1}(a1-1, a2-1))

        else if
            ccolmx{divdwn,b}(1,1)>lsdivheight{divdwn,1}(a1-1,
            a2-1)
            ccolmx{divdwn,b}(1,1)=lsdivheight{divdwn,1}(a1-1,
            a2-1);
            ccolmx{divdwn,b}(1,2)=a1-1;
            ccolmx{divdwn,b}(1,3)=a2-1;
            end

        end

        if isnan(lsdivheight{divdwn,1}(a1-1, a2))

        else if
            ccolmx{divdwn,b}(1,1)>lsdivheight{divdwn,1}(a1-1,
            a2)
            ccolmx{divdwn,b}(1,1)=lsdivheight{divdwn,1}(a1-1,
            a2);
            ccolmx{divdwn,b}(1,2)=a1-1;
            ccolmx{divdwn,b}(1,3)=a2;
            end

        end

        if isnan(lsdivheight{divdwn,1}(a1-1, a2+1))

        else if
            ccolmx{divdwn,b}(1,1)>lsdivheight{divdwn,1}(a1-1,
            a2+1)
            ccolmx{divdwn,b}(1,1)=lsdivheight{divdwn,1}(a1-1,
            a2+1);
            ccolmx{divdwn,b}(1,2)=a1-1;
            ccolmx{divdwn,b}(1,3)=a2+1;
            end

        end

        if isnan(lsdivheight{divdwn,1}(a1-1, a2+2))

```

```

else if
    ccolmx{divdwn,b}(1,1)>lsvdivheight{divdwn,1}(a1-1,
    a2+2)
    ccolmx{divdwn,b}(1,1)=lsvdivheight{divdwn,1}(a1-1,
    a2+2);
    ccolmx{divdwn,b}(1,2)=a1-1;
    ccolmx{divdwn,b}(1,3)=a2+2;
end
end

if isnan(lsvdivheight{divdwn,1}(a1, a2-1))

else if
    ccolmx{divdwn,b}(1,1)>lsvdivheight{divdwn,1}(a1,
    a2-1)
    ccolmx{divdwn,b}(1,1)=lsvdivheight{divdwn,1}(a1,
    a2-1);
    ccolmx{divdwn,b}(1,2)=a1;
    ccolmx{divdwn,b}(1,3)=a2-1;
end
end

if isnan(lsvdivheight{divdwn,1}(a1, a2))

else if
    ccolmx{divdwn,b}(1,1)>lsvdivheight{divdwn,1}(a1,
    a2)
    ccolmx{divdwn,b}(1,1)=lsvdivheight{divdwn,1}(a1,
    a2);
    ccolmx{divdwn,b}(1,2)=a1;
    ccolmx{divdwn,b}(1,3)=a2;
end
end

if isnan(lsvdivheight{divdwn,1}(a1, a2+1))

else if
    ccolmx{divdwn,b}(1,1)>lsvdivheight{divdwn,1}(a1,
    a2+1)
    ccolmx{divdwn,b}(1,1)=lsvdivheight{divdwn,1}(a1,
    a2+1);
    ccolmx{divdwn,b}(1,2)=a1;
    ccolmx{divdwn,b}(1,3)=a2+1;
end
end

if isnan(lsvdivheight{divdwn,1}(a1, a2+2))

else if
    ccolmx{divdwn,b}(1,1)>lsvdivheight{divdwn,1}(a1,
    a2+2)

```

```

        ccolmx{divdwn,b}(1,1)=lsdivheight{divdwn,1}(a1,
        a2+2);
        ccolmx{divdwn,b}(1,2)=a1;
        ccolmx{divdwn,b}(1,3)=a2+2;
        end
    end

    if isnan(lsdivheight{divdwn,1}(a1+1, a2-1))

    else if
        ccolmx{divdwn,b}(1,1)>lsdivheight{divdwn,1}(a1+1,
        a2-1)
        ccolmx{divdwn,b}(1,1)=lsdivheight{divdwn,1}(a1+1,
        a2-1);
        ccolmx{divdwn,b}(1,2)=a1+1;
        ccolmx{divdwn,b}(1,3)=a2-1;
        end
    end

    if isnan(lsdivheight{divdwn,1}(a1+1, a2))

    else if
        ccolmx{divdwn,b}(1,1)>lsdivheight{divdwn,1}(a1+1,
        a2)
        ccolmx{divdwn,b}(1,1)=lsdivheight{divdwn,1}(a1+1,
        a2);
        ccolmx{divdwn,b}(1,2)=a1+1;
        ccolmx{divdwn,b}(1,3)=a2;
        end
    end

    if isnan(lsdivheight{divdwn,1}(a1+1, a2+1))

    else if
        ccolmx{divdwn,b}(1,1)>lsdivheight{divdwn,1}(a1+1,
        a2+1)
        ccolmx{divdwn,b}(1,1)=lsdivheight{divdwn,1}(a1+1,
        a2+1);
        ccolmx{divdwn,b}(1,2)=a1+1;
        ccolmx{divdwn,b}(1,3)=a2+1;
        end
    end

    if isnan(lsdivheight{divdwn,1}(a1+1, a2+2))

    else if
        ccolmx{divdwn,b}(1,1)>lsdivheight{divdwn,1}(a1+1,
        a2+2)
        ccolmx{divdwn,b}(1,1)=lsdivheight{divdwn,1}(a1+1,
        a2+2);
        ccolmx{divdwn,b}(1,2)=a1+1;
        ccolmx{divdwn,b}(1,3)=a2+2;

```

```

        end
    end

    xmax=ccolmx{divdwn,b}(1,2);
    ymax=ccolmx{divdwn,b}(1,3);
    nanc=0;

    ccolmxsum{divdwn,b}=lsdivheight{divdwn,1}(xmax,ymax);

    if isnan(lsdivheight{divdwn,1}(xmax-1,ymax))
        nanc=nanc+1;
    else
        ccolmxsum{divdwn,b}=ccolmxsum{divdwn,b}+lsdivheight{divdwn,1}(xmax-1,ymax);
    end

    if isnan(lsdivheight{divdwn,1}(xmax-1,ymax-1))
        nanc=nanc+1;
    else
        ccolmxsum{divdwn,b}=ccolmxsum{divdwn,b}+lsdivheight{divdwn,1}(xmax-1,ymax-1);
    end

    if isnan(lsdivheight{divdwn,1}(xmax,ymax-1))
        nanc=nanc+1;
    else
        ccolmxsum{divdwn,b}=ccolmxsum{divdwn,b}+lsdivheight{divdwn,1}(xmax,ymax-1);
    end

    if isnan(lsdivheight{divdwn,1}(xmax+1,ymax))
        nanc=nanc+1;
    else
        ccolmxsum{divdwn,b}=ccolmxsum{divdwn,b}+lsdivheight{divdwn,1}(xmax+1,ymax);
    end

    if isnan(lsdivheight{divdwn,1}(xmax+1,ymax+1))
        nanc=nanc+1;
    else
        ccolmxsum{divdwn,b}=ccolmxsum{divdwn,b}+lsdivheight{divdwn,1}(xmax+1,ymax+1);
    end

    if isnan(lsdivheight{divdwn,1}(xmax,ymax+1))
        nanc=nanc+1;
    else
        ccolmxsum{divdwn,b}=ccolmxsum{divdwn,b}+lsdivheight{divdwn,1}(xmax,ymax+1);
    end

    if isnan(lsdivheight{divdwn,1}(xmax-1,ymax+1))
        nanc=nanc+1;
    else
        ccolmxsum{divdwn,b}=ccolmxsum{divdwn,b}+lsdivheight{divdwn,1}(xmax-1,ymax+1);
    end
end

```

```

    if isnan(lsddivheight{divdwn,1}(xmax+1,ymax-1))
        nanc=nanc+1;
    else
        ccolmxsum{divdwn,b}=ccolmxsum{divdwn,b}+lsdivheight{divdwn,1}(xmax+1,ymax-1);
    end

    if nanc==0;
        ccolmxavg{divdwn,b}=(ccolmxsum{divdwn,b}/9);
    end
    if nanc==1;
        ccolmxavg{divdwn,b}=(ccolmxsum{divdwn,b}/8);
    end
    if nanc==2;
        ccolmxavg{divdwn,b}=(ccolmxsum{divdwn,b}/7);
    end
    if nanc==3;
        ccolmxavg{divdwn,b}=(ccolmxsum{divdwn,b}/6);
    end
    if nanc>3;
        ccolmxsum{divdwn,b}=NaN;
        ccolmxavg{divdwn,b}=NaN;
    end

    divdwn=divdwn-1;

end
end

if zch == 6
    divdwn=5;
    while(divdwn>0)
        a1=ccolmx{divdwn+1,b}(1,2);
        a2=ccolmx{divdwn+1,b}(1,3);
        ccolmx{divdwn,b}(1,1)=lsdivheight{divdwn,1}(a1, a2);
        ccolmx{divdwn,b}(1,2)=a1;
        ccolmx{divdwn,b}(1,3)=a2;

        if isnan(lsddivheight{divdwn,1}(a1-1, a2-1))

        else if
            ccolmx{divdwn,b}(1,1)>lsdivheight{divdwn,1}(a1-1,
            a2-1)
            ccolmx{divdwn,b}(1,1)=lsdivheight{divdwn,1}(a1-1,
            a2-1);
            ccolmx{divdwn,b}(1,2)=a1-1;
            ccolmx{divdwn,b}(1,3)=a2-1;
        end

    end

    if isnan(lsddivheight{divdwn,1}(a1-1, a2))

```

```

else if
    ccolmx{divdwn,b}(1,1)>lsvdivheight{divdwn,1}(a1-1,
    a2)
    ccolmx{divdwn,b}(1,1)=lsvdivheight{divdwn,1}(a1-1,
    a2);
    ccolmx{divdwn,b}(1,2)=a1-1;
    ccolmx{divdwn,b}(1,3)=a2;
    end
end

if isnan(lsvdivheight{divdwn,1}(a1-1, a2+1))

else if
    ccolmx{divdwn,b}(1,1)>lsvdivheight{divdwn,1}(a1-1,
    a2+1)
    ccolmx{divdwn,b}(1,1)=lsvdivheight{divdwn,1}(a1-1,
    a2+1);
    ccolmx{divdwn,b}(1,2)=a1-1;
    ccolmx{divdwn,b}(1,3)=a2+1;
    end
end

if isnan(lsvdivheight{divdwn,1}(a1-1, a2+2))

else if
    ccolmx{divdwn,b}(1,1)>lsvdivheight{divdwn,1}(a1-1,
    a2+2)
    ccolmx{divdwn,b}(1,1)=lsvdivheight{divdwn,1}(a1-1,
    a2+2);
    ccolmx{divdwn,b}(1,2)=a1-1;
    ccolmx{divdwn,b}(1,3)=a2+2;
    end
end

if isnan(lsvdivheight{divdwn,1}(a1, a2-1))

else if
    ccolmx{divdwn,b}(1,1)>lsvdivheight{divdwn,1}(a1,
    a2-1)
    ccolmx{divdwn,b}(1,1)=lsvdivheight{divdwn,1}(a1,
    a2-1);
    ccolmx{divdwn,b}(1,2)=a1;
    ccolmx{divdwn,b}(1,3)=a2-1;
    end
end

if isnan(lsvdivheight{divdwn,1}(a1, a2))

else if
    ccolmx{divdwn,b}(1,1)>lsvdivheight{divdwn,1}(a1,
    a2)

```

```

        ccolmx{divdwn,b}(1,1)=lsdivheight{divdwn,1}(a1,
        a2);
        ccolmx{divdwn,b}(1,2)=a1;
        ccolmx{divdwn,b}(1,3)=a2;
        end
    end

    if isnan(lsdivheight{divdwn,1}(a1, a2+1))

    else if
        ccolmx{divdwn,b}(1,1)>lsdivheight{divdwn,1}(a1,
        a2+1)
        ccolmx{divdwn,b}(1,1)=lsdivheight{divdwn,1}(a1,
        a2+1);
        ccolmx{divdwn,b}(1,2)=a1;
        ccolmx{divdwn,b}(1,3)=a2+1;
        end
    end

    if isnan(lsdivheight{divdwn,1}(a1, a2+2))

    else if
        ccolmx{divdwn,b}(1,1)>lsdivheight{divdwn,1}(a1,
        a2+2)
        ccolmx{divdwn,b}(1,1)=lsdivheight{divdwn,1}(a1,
        a2+2);
        ccolmx{divdwn,b}(1,2)=a1;
        ccolmx{divdwn,b}(1,3)=a2+2;
        end
    end

    if isnan(lsdivheight{divdwn,1}(a1+1, a2-1))

    else if
        ccolmx{divdwn,b}(1,1)>lsdivheight{divdwn,1}(a1+1,
        a2-1)
        ccolmx{divdwn,b}(1,1)=lsdivheight{divdwn,1}(a1+1,
        a2-1);
        ccolmx{divdwn,b}(1,2)=a1+1;
        ccolmx{divdwn,b}(1,3)=a2-1;
        end
    end

    if isnan(lsdivheight{divdwn,1}(a1+1, a2))

    else if
        ccolmx{divdwn,b}(1,1)>lsdivheight{divdwn,1}(a1+1,
        a2)
        ccolmx{divdwn,b}(1,1)=lsdivheight{divdwn,1}(a1+1,
        a2);
        ccolmx{divdwn,b}(1,2)=a1+1;
        ccolmx{divdwn,b}(1,3)=a2;

```

```

        end
    end

    if isnan(lsddivheight{divdwn,1}(a1+1, a2+1))

    else if
        ccolmx{divdwn,b}(1,1)>lsdivheight{divdwn,1}(a1+1,
        a2+1)
        ccolmx{divdwn,b}(1,1)=lsdivheight{divdwn,1}(a1+1,
        a2+1);
        ccolmx{divdwn,b}(1,2)=a1+1;
        ccolmx{divdwn,b}(1,3)=a2+1;
        end
    end

    if isnan(lsddivheight{divdwn,1}(a1+1, a2+2))

    else if
        ccolmx{divdwn,b}(1,1)>lsdivheight{divdwn,1}(a1+1,
        a2+2)
        ccolmx{divdwn,b}(1,1)=lsdivheight{divdwn,1}(a1+1,
        a2+2);
        ccolmx{divdwn,b}(1,2)=a1+1;
        ccolmx{divdwn,b}(1,3)=a2+2;
        end
    end

    xmax=ccolmx{divdwn,b}(1,2);
    ymax=ccolmx{divdwn,b}(1,3);
    nanc=0;

    ccolmxsum{divdwn,b}=lsdivheight{divdwn,1}(xmax,ymax);

    if isnan(lsddivheight{divdwn,1}(xmax-1,ymax))
        nanc=nanc+1;
    else
        ccolmxsum{divdwn,b}=ccolmxsum{divdwn,b}+lsdivheight{divdwn,1}(xmax-1,ymax);
    end

    if isnan(lsddivheight{divdwn,1}(xmax-1,ymax-1))
        nanc=nanc+1;
    else
        ccolmxsum{divdwn,b}=ccolmxsum{divdwn,b}+lsdivheight{divdwn,1}(xmax-1,ymax-1);
    end

    if isnan(lsddivheight{divdwn,1}(xmax,ymax-1))
        nanc=nanc+1;
    else
        ccolmxsum{divdwn,b}=ccolmxsum{divdwn,b}+lsdivheight{divdwn,1}(xmax,ymax-1);
    end

```

```

end

if isnan(lsddivheight{divdwn,1}(xmax+1,ymax))
    nanc=nanc+1;
else
    ccolmxsum{divdwn,b}=ccolmxsum{divdwn,b}+lsdivheight{divdwn,1}(xmax+1,ymax);
end

if isnan(lsddivheight{divdwn,1}(xmax+1,ymax+1))
    nanc=nanc+1;
else
    ccolmxsum{divdwn,b}=ccolmxsum{divdwn,b}+lsdivheight{divdwn,1}(xmax+1,ymax+1);
end

if isnan(lsddivheight{divdwn,1}(xmax,ymax+1))
    nanc=nanc+1;
else
    ccolmxsum{divdwn,b}=ccolmxsum{divdwn,b}+lsdivheight{divdwn,1}(xmax,ymax+1);
end

if isnan(lsddivheight{divdwn,1}(xmax-1,ymax+1))
    nanc=nanc+1;
else
    ccolmxsum{divdwn,b}=ccolmxsum{divdwn,b}+lsdivheight{divdwn,1}(xmax-1,ymax+1);
end

if isnan(lsddivheight{divdwn,1}(xmax+1,ymax-1))
    nanc=nanc+1;
else
    ccolmxsum{divdwn,b}=ccolmxsum{divdwn,b}+lsdivheight{divdwn,1}(xmax+1,ymax-1);
end

if nanc==0;
    ccolmxavg{divdwn,b}=(ccolmxsum{divdwn,b}/9);
end
if nanc==1;
    ccolmxavg{divdwn,b}=(ccolmxsum{divdwn,b}/8);
end
if nanc==2;
    ccolmxavg{divdwn,b}=(ccolmxsum{divdwn,b}/7);
end
if nanc==3;
    ccolmxavg{divdwn,b}=(ccolmxsum{divdwn,b}/6);
end
if nanc>3;
    ccolmxsum{divdwn,b}=NaN;
    ccolmxavg{divdwn,b}=NaN;

```

```

        end

        divdwn=divdwn-1;
    end
end
end

if zch == 5
    divup=6;
    while(ccolmx{divup-1,b}(1,1)<-0.25)
        a1=ccolmx{divup-1,b}(1,2);
        a2=ccolmx{divup-1,b}(1,3);
        ccolmx{divup,b}(1,1)=lsdivheight{divup,1}(a1, a2);
        ccolmx{divup,b}(1,2)=a1;
        ccolmx{divup,b}(1,3)=a2;

        if isnan(lsdivheight{divup,1}(a1-1, a2-2))

        else if ccolmx{divup,b}(1,1)>lsdivheight{divup,1}(a1-
            1, a2-2)
            ccolmx{divup,b}(1,1)=lsdivheight{divup,1}(a1-1,
                a2-2);
            ccolmx{divup,b}(1,2)=a1-1;
            ccolmx{divup,b}(1,3)=a2-2;
            end
        end

        if isnan(lsdivheight{divup,1}(a1-1, a2-1))

        else if ccolmx{divup,b}(1,1)>lsdivheight{divup,1}(a1-
            1, a2-1)
            ccolmx{divup,b}(1,1)=lsdivheight{divup,1}(a1-1,
                a2-1);
            ccolmx{divup,b}(1,2)=a1-1;
            ccolmx{divup,b}(1,3)=a2-1;
            end
        end

        end

        if isnan(lsdivheight{divup,1}(a1-1, a2))

        else if ccolmx{divup,b}(1,1)>lsdivheight{divup,1}(a1-
            1, a2)
            ccolmx{divup,b}(1,1)=lsdivheight{divup,1}(a1-1,
                a2);
            ccolmx{divup,b}(1,2)=a1-1;
            ccolmx{divup,b}(1,3)=a2;
            end
        end

        end

        if isnan(lsdivheight{divup,1}(a1-1, a2+1))

        else if ccolmx{divup,b}(1,1)>lsdivheight{divup,1}(a1-
            1, a2+1)

```

```

        ccolmx{divup,b}(1,1)=lsdivheight{divup,1}(a1-1,
        a2+1);
        ccolmx{divup,b}(1,2)=a1-1;
        ccolmx{divup,b}(1,3)=a2+1;
    end
end

if isnan(lsdivheight{divup,1}(a1, a2-2))

else if ccolmx{divup,b}(1,1)>lsdivheight{divup,1}(a1,
    a2-2)
        ccolmx{divup,b}(1,1)=lsdivheight{divup,1}(a1, a2-
        2);
        ccolmx{divup,b}(1,2)=a1;
        ccolmx{divup,b}(1,3)=a2-2;
    end
end

if isnan(lsdivheight{divup,1}(a1, a2-1))

else if ccolmx{divup,b}(1,1)>lsdivheight{divup,1}(a1,
    a2-1)
        ccolmx{divup,b}(1,1)=lsdivheight{divup,1}(a1, a2-
        1);
        ccolmx{divup,b}(1,2)=a1;
        ccolmx{divup,b}(1,3)=a2-1;
    end
end

if isnan(lsdivheight{divup,1}(a1, a2))

else if ccolmx{divup,b}(1,1)>lsdivheight{divup,1}(a1,
    a2)
        ccolmx{divup,b}(1,1)=lsdivheight{divup,1}(a1,
        a2);
        ccolmx{divup,b}(1,2)=a1;
        ccolmx{divup,b}(1,3)=a2;
    end
end

if isnan(lsdivheight{divup,1}(a1, a2+1))

else if ccolmx{divup,b}(1,1)>lsdivheight{divup,1}(a1,
    a2+1)
        ccolmx{divup,b}(1,1)=lsdivheight{divup,1}(a1,
        a2+1);
        ccolmx{divup,b}(1,2)=a1;
        ccolmx{divup,b}(1,3)=a2+1;
    end
end

if isnan(lsdivheight{divup,1}(a1+1, a2-2))

```

```

else if
    ccolmx{divup,b}(1,1)>lsvheight{divup,1}(a1+1,
    a2-2)
    ccolmx{divup,b}(1,1)=lsvheight{divup,1}(a1+1,
    a2-2);
    ccolmx{divup,b}(1,2)=a1+1;
    ccolmx{divup,b}(1,3)=a2-2;
end
end

if isnan(lsvheight{divup,1}(a1+1, a2-1))

else if
    ccolmx{divup,b}(1,1)>lsvheight{divup,1}(a1+1,
    a2-1)
    ccolmx{divup,b}(1,1)=lsvheight{divup,1}(a1+1,
    a2-1);
    ccolmx{divup,b}(1,2)=a1+1;
    ccolmx{divup,b}(1,3)=a2-1;
end
end

if isnan(lsvheight{divup,1}(a1+1, a2))

else if
    ccolmx{divup,b}(1,1)>lsvheight{divup,1}(a1+1,
    a2)
    ccolmx{divup,b}(1,1)=lsvheight{divup,1}(a1+1,
    a2);
    ccolmx{divup,b}(1,2)=a1+1;
    ccolmx{divup,b}(1,3)=a2;
end
end

if isnan(lsvheight{divup,1}(a1+1, a2+1))

else if
    ccolmx{divup,b}(1,1)>lsvheight{divup,1}(a1+1,
    a2+1)
    ccolmx{divup,b}(1,1)=lsvheight{divup,1}(a1+1,
    a2+1);
    ccolmx{divup,b}(1,2)=a1+1;
    ccolmx{divup,b}(1,3)=a2+1;
end
end

xmax=ccolmx{divup,b}(1,2);
ymax=ccolmx{divup,b}(1,3);
nanc=0;
ccolmxsum{divup,b}=lsvheight{divup,1}(xmax,ymax);

```

```

if isnan(lsdiveight{divup,1}(xmax-1,ymax))
    nanc=nanc+1;
else
    ccolmxsum{divup,b}=ccolmxsum{divup,b}+lsdiveight
    {divup,1}(xmax-1,ymax);
end

if isnan(lsdiveight{divup,1}(xmax-1,ymax-1))
    nanc=nanc+1;
else
    ccolmxsum{divup,b}=ccolmxsum{divup,b}+lsdiveight
    {divup,1}(xmax-1,ymax-1);
end

if isnan(lsdiveight{divup,1}(xmax,ymax-1))
    nanc=nanc+1;
else
    ccolmxsum{divup,b}=ccolmxsum{divup,b}+lsdiveight
    {divup,1}(xmax,ymax-1);
end

if isnan(lsdiveight{divup,1}(xmax+1,ymax))
    nanc=nanc+1;
else
    ccolmxsum{divup,b}=ccolmxsum{divup,b}+lsdiveight
    {divup,1}(xmax+1,ymax);
end

if isnan(lsdiveight{divup,1}(xmax+1,ymax+1))
    nanc=nanc+1;
else
    ccolmxsum{divup,b}=ccolmxsum{divup,b}+lsdiveight
    {divup,1}(xmax+1,ymax+1);
end

if isnan(lsdiveight{divup,1}(xmax,ymax+1))
    nanc=nanc+1;
else
    ccolmxsum{divup,b}=ccolmxsum{divup,b}+lsdiveight
    {divup,1}(xmax,ymax+1);
end

if isnan(lsdiveight{divup,1}(xmax-1,ymax+1))
    nanc=nanc+1;
else
    ccolmxsum{divup,b}=ccolmxsum{divup,b}+lsdiveight
    {divup,1}(xmax-1,ymax+1);
end

if isnan(lsdiveight{divup,1}(xmax+1,ymax-1))
    nanc=nanc+1;
else

```

```

        ccolmxsum{divup,b}=ccolmxsum{divup,b}+lsdivheight
        {divup,1}(xmax+1,ymax-1);
    end

    if nanc==0;
        ccolmxavg{divup,b}=(ccolmxsum{divup,b}/9);
    end
    if nanc==1;
        ccolmxavg{divup,b}=(ccolmxsum{divup,b}/8);
    end
    if nanc==2;
        ccolmxavg{divup,b}=(ccolmxsum{divup,b}/7);
    end
    if nanc==3;
        ccolmxavg{divup,b}=(ccolmxsum{divup,b}/6);
    end
    if nanc>3;
        ccolmxsum{divup,b}=NaN;
        ccolmxavg{divup,b}=NaN;
    end

    divup=divup+1;
    if divup==20
        break
    end
end
end

if zch == 6
    divup=7;
    while(ccolmx{divup-1,b}(1,1)<-0.25)
        a1=ccolmx{divup-1,b}(1,2);
        a2=ccolmx{divup-1,b}(1,3);
        ccolmx{divup,b}(1,1)=lsdivheight{divup,1}(a1, a2);
        ccolmx{divup,b}(1,2)=a1;
        ccolmx{divup,b}(1,3)=a2;

        if isnan(lsdivheight{divup,1}(a1-1, a2-2))

        else if ccolmx{divup,b}(1,1)>lsdivheight{divup,1}(a1-
            1, a2-2)
            ccolmx{divup,b}(1,1)=lsdivheight{divup,1}(a1-1,
            a2-2);
            ccolmx{divup,b}(1,2)=a1-1;
            ccolmx{divup,b}(1,3)=a2-2;
        end

    end

    if isnan(lsdivheight{divup,1}(a1-1, a2-1))

    else if ccolmx{divup,b}(1,1)>lsdivheight{divup,1}(a1-
        1, a2-1)

```

```

        ccolmx{divup,b}(1,1)=lsdivheight{divup,1}(a1-1,
        a2-1);
        ccolmx{divup,b}(1,2)=a1-1;
        ccolmx{divup,b}(1,3)=a2-1;
        end
    end

    if isnan(lsdivheight{divup,1}(a1-1, a2))

    else if ccolmx{divup,b}(1,1)>lsdivheight{divup,1}(a1-
    1, a2)
        ccolmx{divup,b}(1,1)=lsdivheight{divup,1}(a1-1,
        a2);
        ccolmx{divup,b}(1,2)=a1-1;
        ccolmx{divup,b}(1,3)=a2;
        end
    end

    if isnan(lsdivheight{divup,1}(a1-1, a2+1))

    else if ccolmx{divup,b}(1,1)>lsdivheight{divup,1}(a1-
    1, a2+1)
        ccolmx{divup,b}(1,1)=lsdivheight{divup,1}(a1-1,
        a2+1);
        ccolmx{divup,b}(1,2)=a1-1;
        ccolmx{divup,b}(1,3)=a2+1;
        end
    end

    if isnan(lsdivheight{divup,1}(a1, a2-2))

    else if ccolmx{divup,b}(1,1)>lsdivheight{divup,1}(a1,
    a2-2)
        ccolmx{divup,b}(1,1)=lsdivheight{divup,1}(a1, a2-
        2);
        ccolmx{divup,b}(1,2)=a1;
        ccolmx{divup,b}(1,3)=a2-2;
        end
    end

    if isnan(lsdivheight{divup,1}(a1, a2-1))

    else if ccolmx{divup,b}(1,1)>lsdivheight{divup,1}(a1,
    a2-1)
        ccolmx{divup,b}(1,1)=lsdivheight{divup,1}(a1, a2-
        1);
        ccolmx{divup,b}(1,2)=a1;
        ccolmx{divup,b}(1,3)=a2-1;
        end
    end

    if isnan(lsdivheight{divup,1}(a1, a2))

```

```

else if ccolmx{divup,b}(1,1)>lsvdivheight{divup,1}(a1,
a2)
    ccolmx{divup,b}(1,1)=lsvdivheight{divup,1}(a1,
a2);
    ccolmx{divup,b}(1,2)=a1;
    ccolmx{divup,b}(1,3)=a2;
end
end

if isnan(lsvdivheight{divup,1}(a1, a2+1))

else if ccolmx{divup,b}(1,1)>lsvdivheight{divup,1}(a1,
a2+1)
    ccolmx{divup,b}(1,1)=lsvdivheight{divup,1}(a1,
a2+1);
    ccolmx{divup,b}(1,2)=a1;
    ccolmx{divup,b}(1,3)=a2+1;
end
end

if isnan(lsvdivheight{divup,1}(a1+1, a2-2))

else if
    ccolmx{divup,b}(1,1)>lsvdivheight{divup,1}(a1+1,
a2-2)
    ccolmx{divup,b}(1,1)=lsvdivheight{divup,1}(a1+1,
a2-2);
    ccolmx{divup,b}(1,2)=a1+1;
    ccolmx{divup,b}(1,3)=a2-2;
end
end

if isnan(lsvdivheight{divup,1}(a1+1, a2-1))

else if
    ccolmx{divup,b}(1,1)>lsvdivheight{divup,1}(a1+1,
a2-1)
    ccolmx{divup,b}(1,1)=lsvdivheight{divup,1}(a1+1,
a2-1);
    ccolmx{divup,b}(1,2)=a1+1;
    ccolmx{divup,b}(1,3)=a2-1;
end
end

if isnan(lsvdivheight{divup,1}(a1+1, a2))

else if
    ccolmx{divup,b}(1,1)>lsvdivheight{divup,1}(a1+1,
a2)

    ccolmx{divup,b}(1,1)=lsvdivheight{divup,1}(a1+1,
a2);

```

```

        ccolmx{divup,b}(1,2)=a1+1;
        ccolmx{divup,b}(1,3)=a2;
    end
end

if isnan(lsdiveheight{divup,1}(a1+1, a2+1))

else if
    ccolmx{divup,b}(1,1)>lsdiveheight{divup,1}(a1+1,
    a2+1)
    ccolmx{divup,b}(1,1)=lsdiveheight{divup,1}(a1+1,
    a2+1);
    ccolmx{divup,b}(1,2)=a1+1;
    ccolmx{divup,b}(1,3)=a2+1;
    end
end

xmax=ccolmx{divup,b}(1,2);
ymax=ccolmx{divup,b}(1,3);
nanc=0;

ccolmxsum{divup,b}=lsdiveheight{divup,1}(xmax,ymax);

if isnan(lsdiveheight{divup,1}(xmax-1,ymax))
    nanc=nanc+1;
else
    ccolmxsum{divup,b}=ccolmxsum{divup,b}+lsdiveheight
    {divup,1}(xmax-1,ymax);
end

if isnan(lsdiveheight{divup,1}(xmax-1,ymax-1))
    nanc=nanc+1;
else
    ccolmxsum{divup,b}=ccolmxsum{divup,b}+lsdiveheight
    {divup,1}(xmax-1,ymax-1);
end

if isnan(lsdiveheight{divup,1}(xmax,ymax-1))
    nanc=nanc+1;
else
    ccolmxsum{divup,b}=ccolmxsum{divup,b}+lsdiveheight
    {divup,1}(xmax,ymax-1);
end

if isnan(lsdiveheight{divup,1}(xmax+1,ymax))
    nanc=nanc+1;
else
    ccolmxsum{divup,b}=ccolmxsum{divup,b}+lsdiveheight
    {divup,1}(xmax+1,ymax);
end

if isnan(lsdiveheight{divup,1}(xmax+1,ymax+1))

```

```

        nanc=nanc+1;
    else
        ccolmxsum{divup,b}=ccolmxsum{divup,b}+lsdivheight
        {divup,1}(xmax+1,ymax+1);
    end

    if isnan(lsdivheight{divup,1}(xmax,ymax+1))
        nanc=nanc+1;
    else
        ccolmxsum{divup,b}=ccolmxsum{divup,b}+lsdivheight
        {divup,1}(xmax,ymax+1);
    end

    if isnan(lsdivheight{divup,1}(xmax-1,ymax+1))
        nanc=nanc+1;
    else
        ccolmxsum{divup,b}=ccolmxsum{divup,b}+lsdivheight
        {divup,1}(xmax-1,ymax+1);
    end

    if isnan(lsdivheight{divup,1}(xmax+1,ymax-1))
        nanc=nanc+1;
    else
        ccolmxsum{divup,b}=ccolmxsum{divup,b}+lsdivheight
        {divup,1}(xmax+1,ymax-1);
    end

    if nanc==0;
        ccolmxavg{divup,b}=(ccolmxsum{divup,b}/9);
    end
    if nanc==1;
        ccolmxavg{divup,b}=(ccolmxsum{divup,b}/8);
    end
    if nanc==2;
        ccolmxavg{divup,b}=(ccolmxsum{divup,b}/7);
    end
    if nanc==3;
        ccolmxavg{divup,b}=(ccolmxsum{divup,b}/6);
    end
    if nanc>3;
        ccolmxsum{divup,b}=NaN;
        ccolmxavg{divup,b}=NaN;
    end

    divup=divup+1;
    if divup == 25
        break
    end
end
end
end

```

Appendix B

The following section provides examples of unique patterns of convergence observed during this study. In particular, these include a wishbone convergence column (B.1d) and the descending convergence column associated with the rear flank downdraft (B.2d).

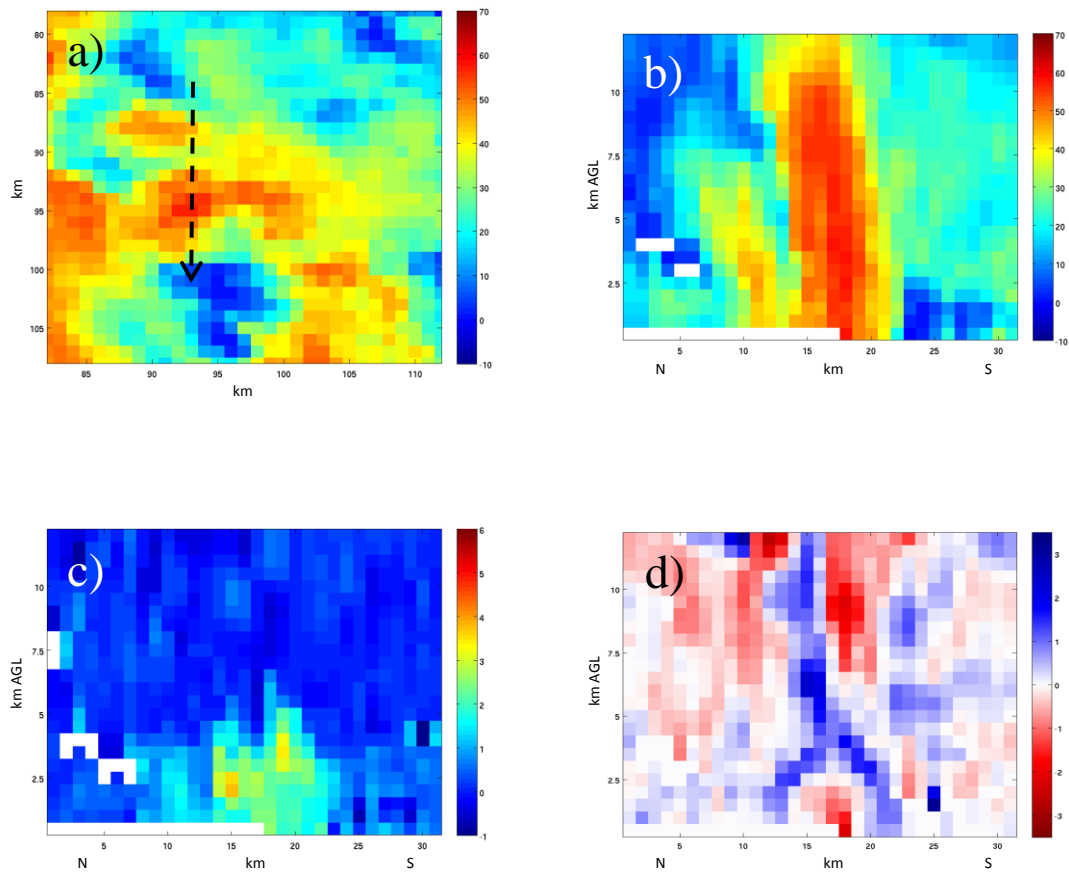


Figure B.1: a) Planview of reflectivity (dBZ) at 2 km AGL centered on SB 1 Cell 3. Dashed arrow indicates the location of the north (N)-to-south (S) cross-sections shown in b), c) and d). b) Reflectivity (dBZ) cross-section of SB 1 Cell 3. c) Z_{DR} (dB) cross-section of SB 1 Cell 3. d) Convergence (blue)/divergence (red) ($10^{-3} s^{-1}$) cross-section of SB 1 Cell 3 indicating a wishbone pattern. All valid at 0333 UTC 06/21/14.

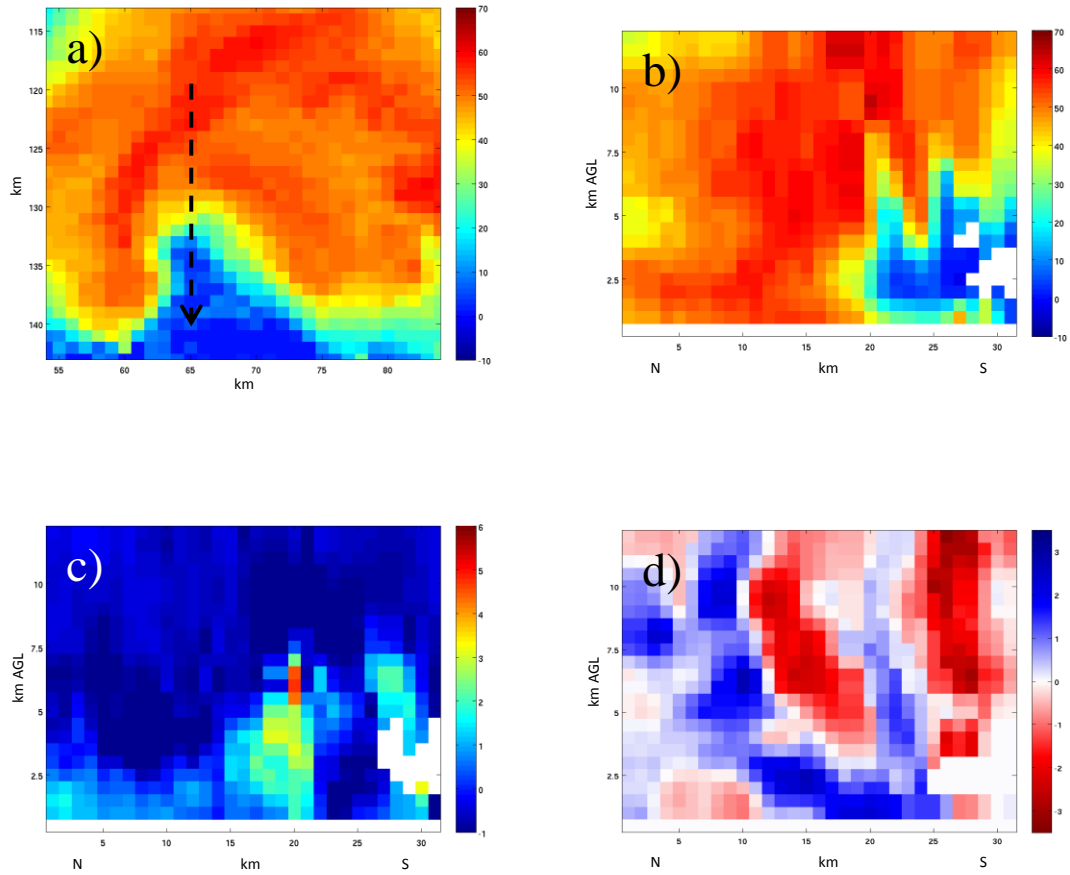


Figure B.2: a) Planview of reflectivity (dBZ) at 2 km AGL centered on IOP 7 Cell 4. Dashed arrow indicates the location of the north (N)-to-south (S) cross-sections shown in b), c) and d). b) Reflectivity (dBZ) cross-section of IOP 7 Cell 4. c) Z_{DR} (dB) cross-section of IOP 7 Cell 4. d) Convergence (blue)/divergence (red) (10^{-3} s^{-1}) cross-section of IOP 7 Cell 4 indicating a wishbone pattern. All valid at 2357 UTC 06/24/15.

The following provides more examples of convergence columns. An example from each cell examined in each of the cases studied is provided in order to provide a wide array of convergence column examples. The corresponding cross-section of differential reflectivity (Z_{DR}) will also be shown in order to portray the collocation with the Z_{DR} column.

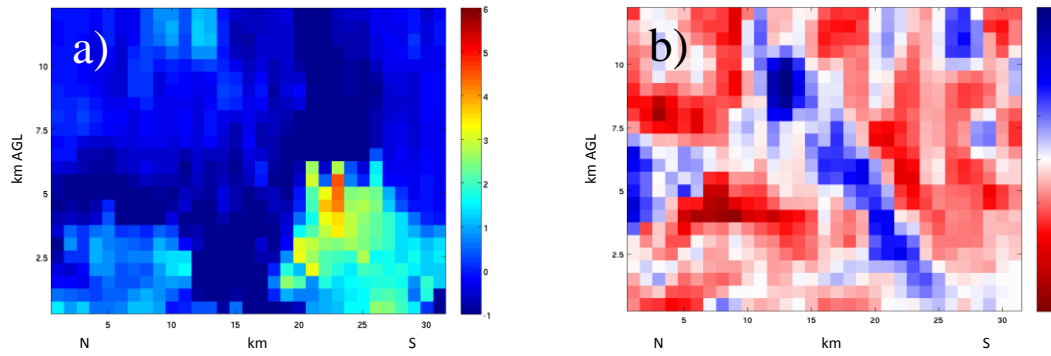


Figure B.3: a) Z_{DR} (dB) north (N)-to-south (S) cross-section of IOP 2 Cell 1. b) Convergence (blue)/divergence (red) ($10^{-3} s^{-1}$) north (N)-to-south (S) cross-section of IOP 2 Cell 1. Both valid at 2136 UTC 06/03/14.

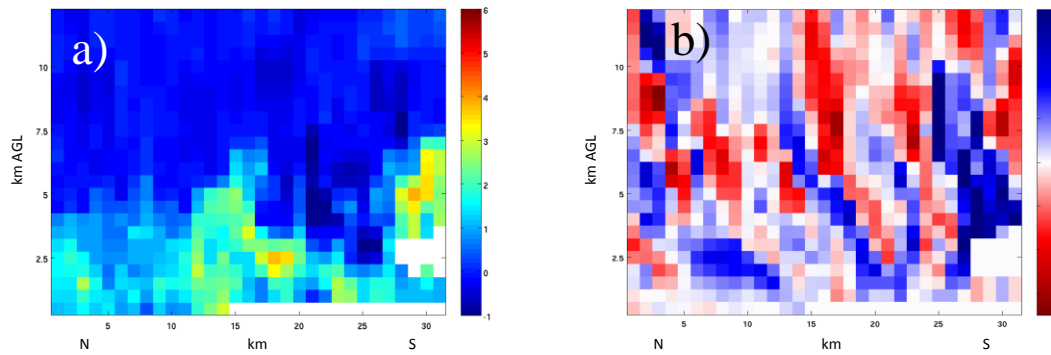


Figure B.4: a) Z_{DR} (dB) north (N)-to-south (S) cross-section of IOP 2 Cell 2. b) Convergence (blue)/divergence (red) ($10^{-3} s^{-1}$) north (N)-to-south (S) cross-section of IOP 2 Cell 2. Both valid at 0114 UTC 06/04/14.

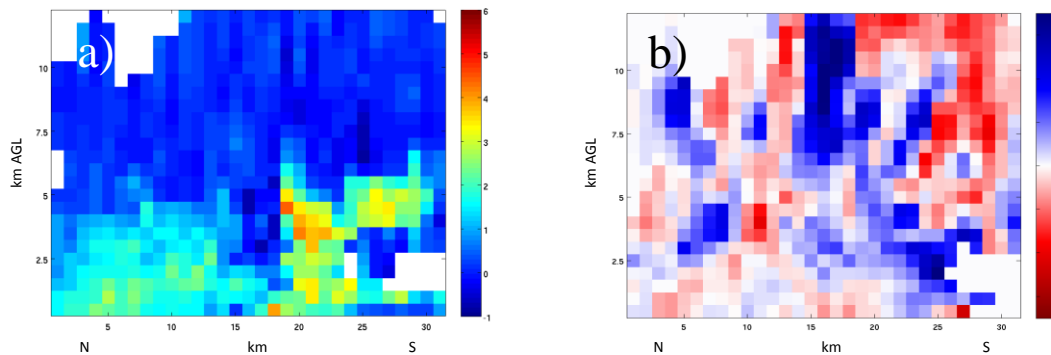


Figure B.5: a) Z_{DR} (dB) north (N)-to-south (S) cross-section of IOP 2 Cell 3. b) Convergence (blue)/divergence (red) ($10^{-3} s^{-1}$) north (N)-to-south (S) cross-section of IOP 2 Cell 3. Both valid at 2204 UTC 06/03/14.

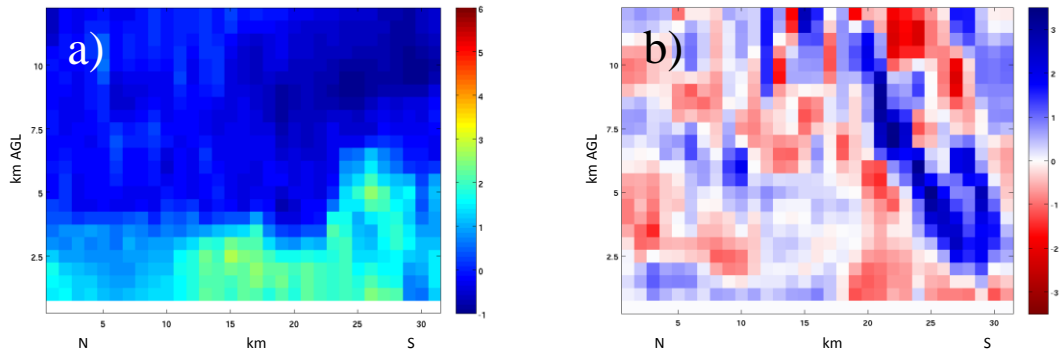


Figure 6: a) Z_{DR} (dB) north (N)-to-south (S) cross-section of IOP 2 Cell 4. b) Convergence (blue)/divergence (red) (10^{-3} s^{-1}) north (N)-to-south (S) cross-section of IOP 2 Cell 4. Both valid at 0250 UTC 06/04/14.

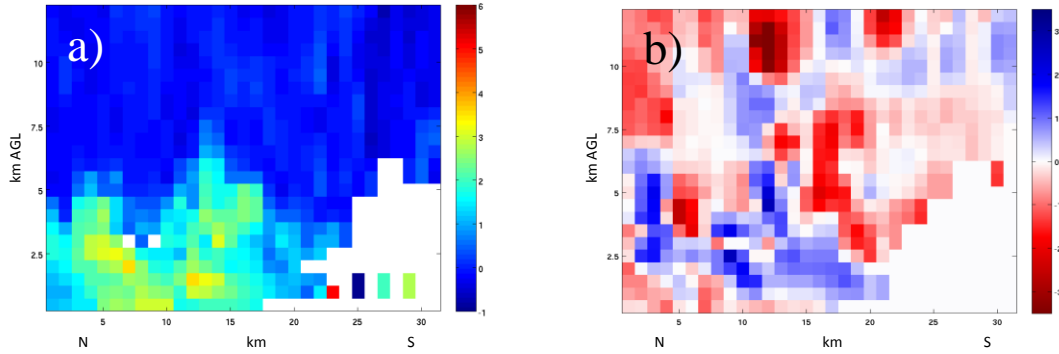


Figure B.7: a) Z_{DR} (dB) north (N)-to-south (S) cross-section of IOP 2 Cell 5. b) Convergence (blue)/divergence (red) (10^{-3} s^{-1}) north (N)-to-south (S) cross-section of IOP 2 Cell 5. Both valid at 2340 UTC 06/03/14.

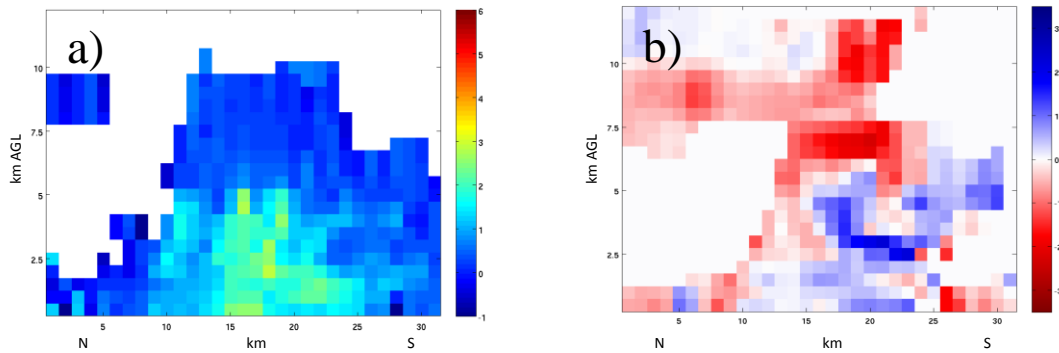


Figure B.8: a) Z_{DR} (dB) north (N)-to-south (S) cross-section of IOP 4 Cell 1. b) Convergence (blue)/divergence (red) (10^{-3} s^{-1}) north (N)-to-south (S) cross-section of IOP 4 Cell 1. Both valid at 0342 UTC 07/17/14.

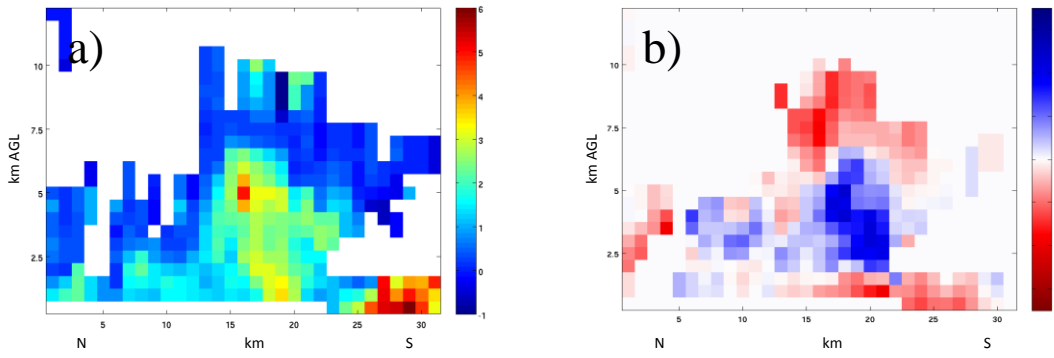


Figure B.9: a) Z_{DR} (dB) north (N)-to-south (S) cross-section of IOP 4 Cell 2. b) Convergence (blue)/divergence (red) ($10^{-3} s^{-1}$) north (N)-to-south (S) cross-section of IOP 4 Cell 2. Both valid at 0311 UTC 07/17/14.

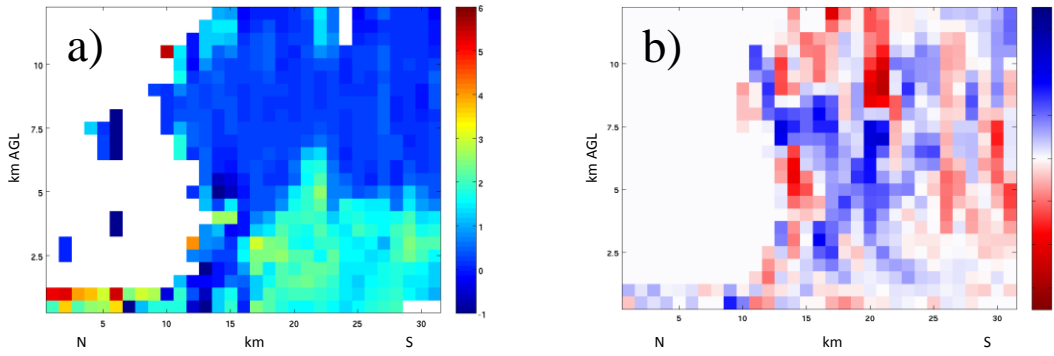


Figure B.10: a) Z_{DR} (dB) north (N)-to-south (S) cross-section of IOP 4 Cell 3. b) Convergence (blue)/divergence (red) ($10^{-3} s^{-1}$) north (N)-to-south (S) cross-section of IOP 4 Cell 3. Both valid at 0501 UTC 07/17/14.

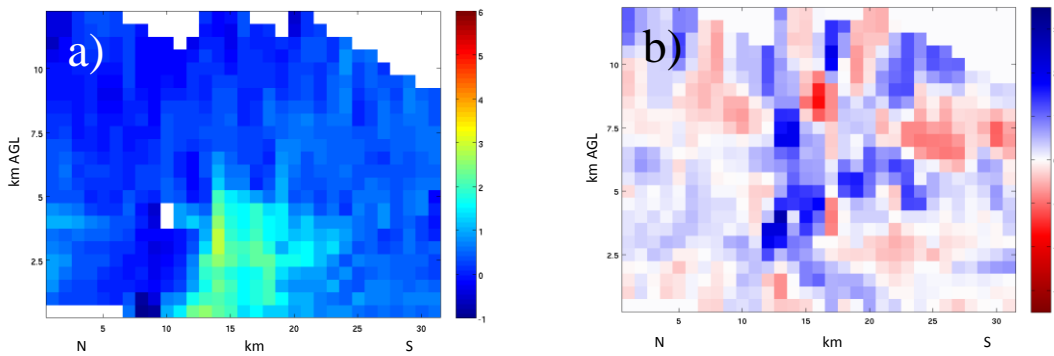


Figure B.11: a) Z_{DR} (dB) north (N)-to-south (S) cross-section of IOP 4 Cell 4. b) Convergence (blue)/divergence (red) ($10^{-3} s^{-1}$) north (N)-to-south (S) cross-section of IOP 4 Cell 4. Both valid at 0419 UTC 07/17/14.

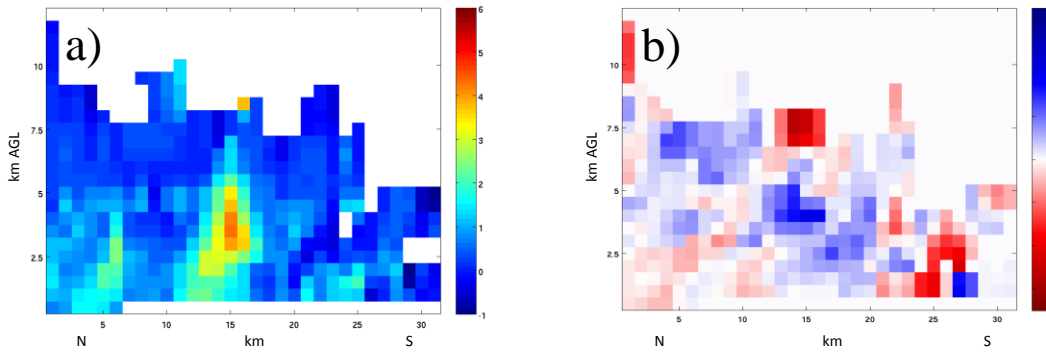


Figure B.12: a) Z_{DR} (dB) north (N)-to-south (S) cross-section of IOP 4 Cell 5. b) Convergence (blue)/divergence (red) (10^{-3} s^{-1}) north (N)-to-south (S) cross-section of IOP 4 Cell 5. Both valid at 0321 UTC 07/17/14.

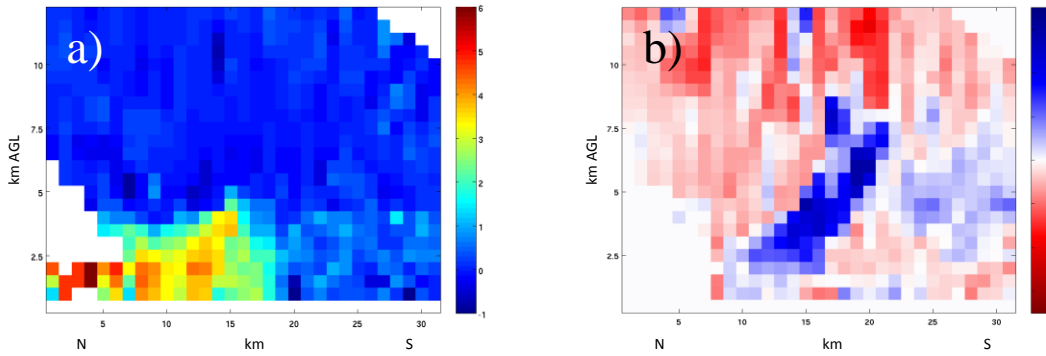


Figure B.13: a) Z_{DR} (dB) north (N)-to-south (S) cross-section of IOP 5 Cell 1. b) Convergence (blue)/divergence (red) (10^{-3} s^{-1}) north (N)-to-south (S) cross-section of IOP 5 Cell 1. Both valid at 0533 UTC 06/05/15.

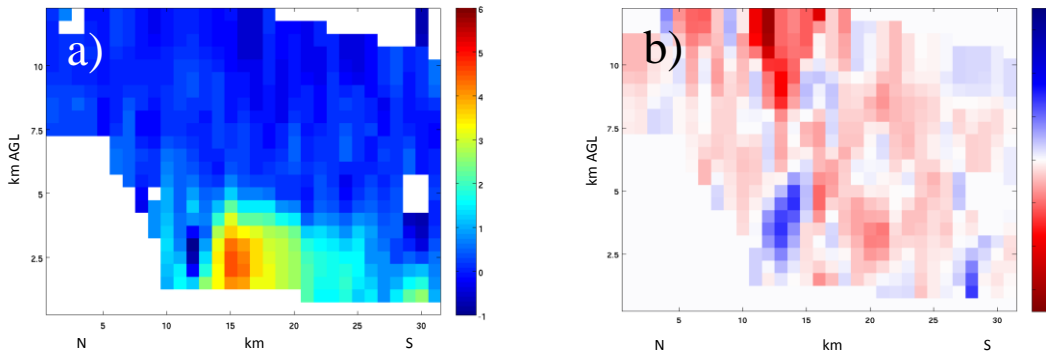


Figure B.14: a) Z_{DR} (dB) north (N)-to-south (S) cross-section of IOP 5 Cell 2. b) Convergence (blue)/divergence (red) (10^{-3} s^{-1}) north (N)-to-south (S) cross-section of IOP 5 Cell 2. Both valid at 0733 UTC 06/05/15.

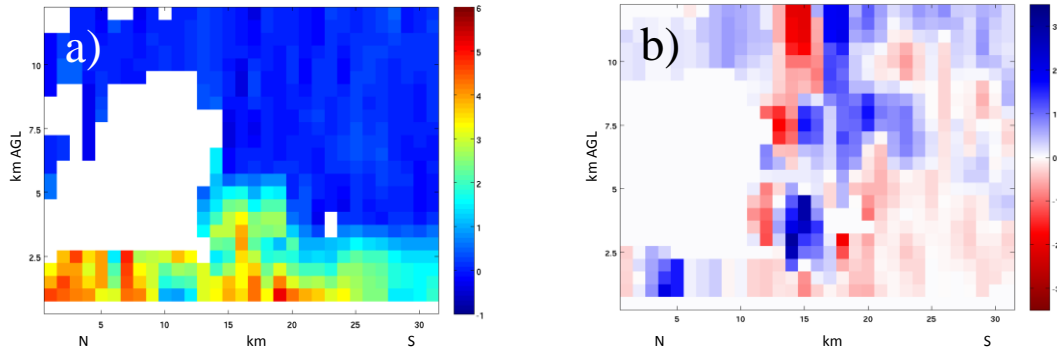


Figure B.15: a) Z_{DR} (dB) north (N)-to-south (S) cross-section of IOP 5 Cell 3. b) Convergence (blue)/divergence (red) (10^{-3} s^{-1}) north (N)-to-south (S) cross-section of IOP 5 Cell 3. Both valid at 0311 UTC 06/05/15.

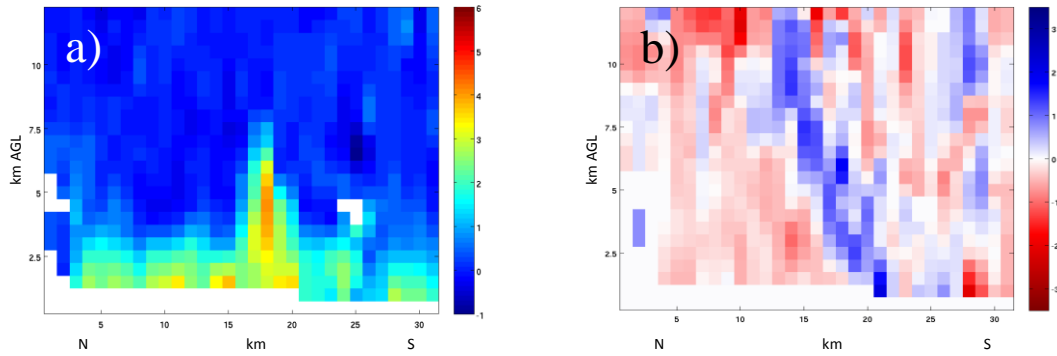


Figure B.16: a) Z_{DR} (dB) north (N)-to-south (S) cross-section of IOP 5 Cell 4. b) Convergence (blue)/divergence (red) (10^{-3} s^{-1}) north (N)-to-south (S) cross-section of IOP 5 Cell 4. Both valid at 0042 UTC 06/05/15.

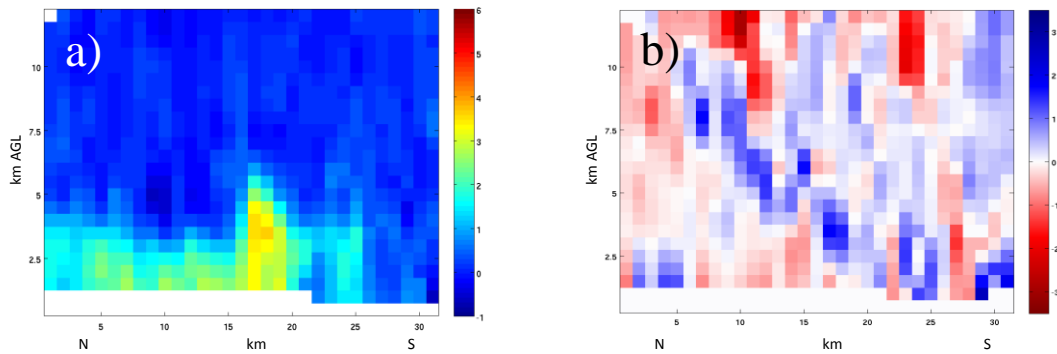


Figure B.17: a) Z_{DR} (dB) north (N)-to-south (S) cross-section of IOP 5 Cell 5. b) Convergence (blue)/divergence (red) (10^{-3} s^{-1}) north (N)-to-south (S) cross-section of IOP 5 Cell 5. Both valid at 0131 UTC 06/05/15.

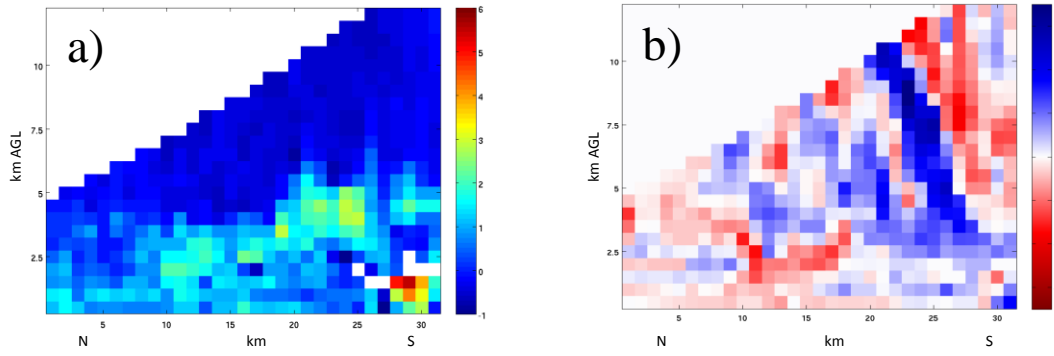


Figure B.18: a) Z_{DR} (dB) north (N)-to-south (S) cross-section of IOP 7 Cell 1. b) Convergence (blue)/divergence (red) (10^{-3} s^{-1}) north (N)-to-south (S) cross-section of IOP 7 Cell 1. Both valid at 0353 UTC 06/25/15.

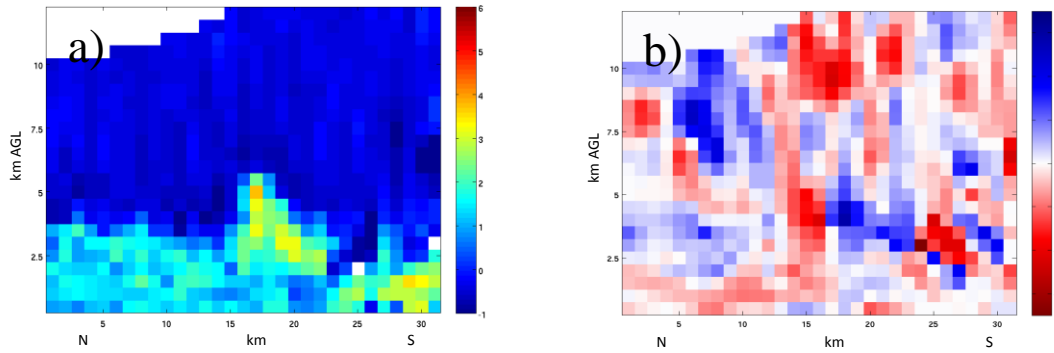


Figure B.19: a) Z_{DR} (dB) north (N)-to-south (S) cross-section of IOP 7 Cell 2. b) Convergence (blue)/divergence (red) (10^{-3} s^{-1}) north (N)-to-south (S) cross-section of IOP 7 Cell 2. Both valid at 0646 UTC 06/25/15.

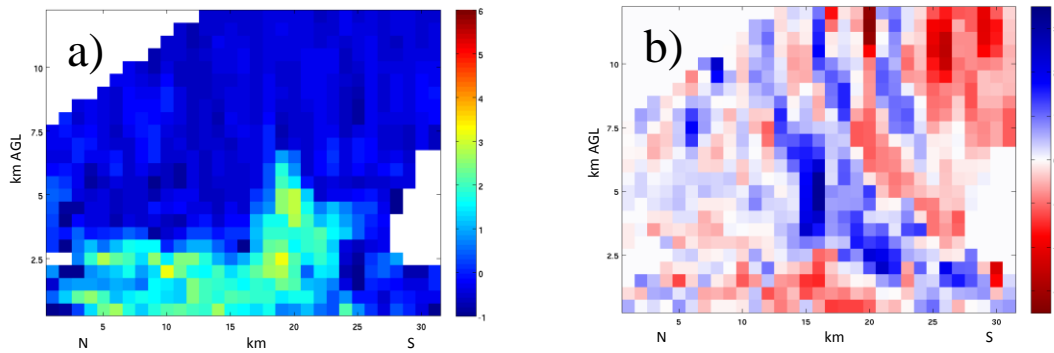


Figure B.20: a) Z_{DR} (dB) north (N)-to-south (S) cross-section of IOP 7 Cell 3. b) Convergence (blue)/divergence (red) (10^{-3} s^{-1}) north (N)-to-south (S) cross-section of IOP 7 Cell 3. Both valid at 0543 UTC 06/25/15.

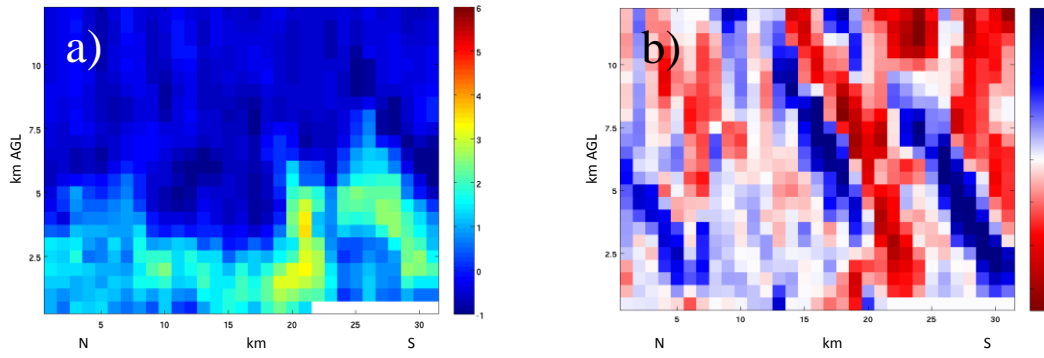


Figure B.21: a) Z_{DR} (dB) north (N)-to-south (S) cross-section of IOP 7 Cell 4. b) Convergence (blue)/divergence (red) (10^{-3} s^{-1}) north (N)-to-south (S) cross-section of IOP 7 Cell 4. Both valid at 0142 UTC 06/25/15.

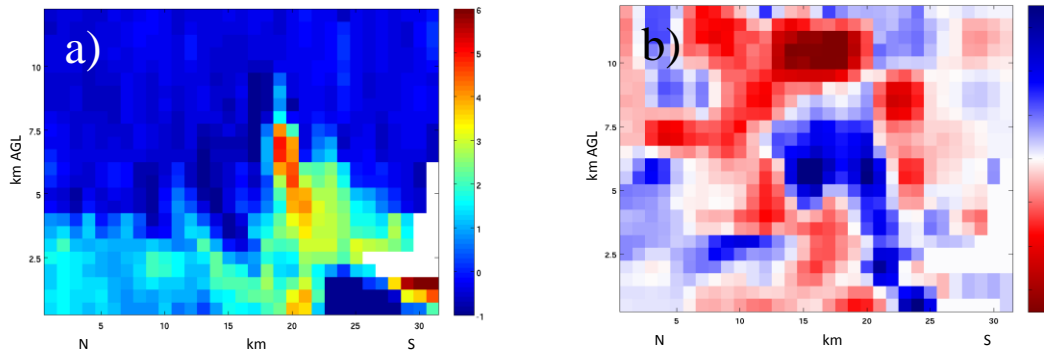


Figure 22: a) Z_{DR} (dB) north (N)-to-south (S) cross-section of IOP 7 Cell 5. b) Convergence (blue)/divergence (red) (10^{-3} s^{-1}) north (N)-to-south (S) cross-section of IOP 7 Cell 5. Both valid at 2346 UTC 06/24/15.

References

- Augustine, J. A., and F. Caracena, 1994: Lower-tropospheric precursors to nocturnal MCS development over the central United States. *Wea. Forecasting*, **9**, 116-135.
- Billings, J. M., and M. D. Parker, 2012: Evolution and maintenance of the 22-23 June 2003 nocturnal convection during BAMEX. *Wea. Forecasting*, **27**, 279-300.
- Bluestein, H. B., A. L. Pazmany, J. C. Galloway, and R. E. McIntosh, 1995: Studies of the substructure of severe convective storms using a mobile 3-mm-wavelength Doppler radar. *Bull. Amer. Meteor. Soc.*, **76**, 2155–2169.
- Brandes, E. A., 1977: Flow in severe thunderstorms observed by dual-Doppler radar. *Mon. Wea. Rev.*, **105**, 113-120.
- Brandes, E. A., J. Vivekanandan, J. D. Tuttle, and C. J. Kessinger, 1995: A study of thunderstorm microphysics with multiparameter radar and aircraft observations. *Mon. Wea. Rev.*, **123**, 3129-3143.
- Bringi, V. N., D. A. Burrows, and S. M. Menon, 1991: Multiparameter radar and aircraft study of raindrop spectral evolution in warm-based clouds. *J. Appl. Meteor.*, **30**, 853-880.
- Byers, H. R., and R. R. Braham, 1948: Thunderstorm structure and circulation. *J. Meteor.*, **5**, 71-86.
- Colman, B. R., 1990a: Thunderstorms above frontal surfaces in environments without positive CAPE. Part I: A climatology. *Mon. Wea. Rev.*, **118**, 1103-1121.
- Colman, B. R., 1990b: Thunderstorms above frontal surfaces in environments without positive CAPE. Part II: Organization and instability mechanism. *Mon. Wea. Rev.*, **118**: 1123-1144.
- Coniglio, M. C., H. E. Brooks, S. F. Corfidi, and S. J. Weiss, 2007: Forecasting the maintenance of quasi-linear mesoscale convective systems. *Wea. Forecasting*, **22**, 556–570.
- Corfidi, S. F., S. J. Corfidi, and D. M. Schultz, 2008: Elevated convection and castellanus: Ambiguities, significance, and questions. *Wea. Forecasting*, **23**, 1280-1303.

- Cotton, W. R., M. S. Lin, R. L. McAnelly, and C. J. Tremback, 1989: A composite model of mesoscale convective complexes. *Mon. Wea. Rev.*, **117**, 765–783.
- Emanuel, K. A., 1983: Frontal circulations in the presence of small moist symmetric stability. *J. Atmos. Sci.*, **42**: 1062-1071.
- Fritsch, J. M., and G. S. Forbes, 2001: Mesoscale convective systems. *Severe Convective Storms, Meteor. Monogr.*, No. 50, Amer. Meteor. Soc., 323–357.
- Grant, B. N., 1995: Elevated cold-sector severe thunderstorms: A preliminary study. *Natl. Wea. Dig.*, **19**(4), 25-31.
- Hall, M. P. M., J. W. F. Goddard, and S. M. Cherry, 1984: Identification of hydrometeors and other targets by dual-polarization radar. *Radio. Sci.*, **19**, 132-140.
- Horgan, K. L., D. M. Schultz, J. E. Hales, S. F. Corfidi, and R. H. Johns, 2007: A five-year climatology of elevated severe convective storms in the United States east of the Rocky Mountains. *Wea. Forecasting*, **22**, 1031-1044.
- Houze, R. A., Jr., M. I. Biggerstaff, S. A. Rutledge, and B. F. Smull, 1989: Interpretation of Doppler weather radar displays of midlatitude mesoscale convective systems. *Bull. Amer. Meteor. Soc.*, **70**, 608–619.
- Illingworth, A. J., J. W. F. Goddard, and S. M. Cherry, 1987: Polarization radar studies of precipitation development in convective storms. *Quart. J. Roy. Meteor. Soc.*, **113**, 469-489.
- Junker, N. W., R. S. Schneider, and S. L. Fauver, 1999: A study of heavy rainfall events during the great Midwest flood of 1993. *Wea. Forecasting*, **14**, 701–712
- Kumjian, M. R., 2013: Principles and application of dual-polarization weather radar. Part II: Warm- and cold-season applications. *J. Operational Meteor.*, **1** (20), 243-264.
- Lakshamanan, V., T. Smith, K. Hondl, G. J. Stumpf, and A. Witt, 2006: A real-time, three dimensional, rapidly updating, heterogeneous radar merger technique for reflectivity, velocity and derived products. *Wea. Forecasting*, **21**, 802-823
- Lakshamanan, V., T. Smith, G. Stumpf, and K. Hondl, 2007: The Warning Decision Support System – Integrated Information. *Wea. Forecasting*, **22**, 596-612.
- Maddox, R. A., C. F. Chappell, and L. R. Hoxit, 1979: Synoptic and meso- α scale aspects of flash flood events. *Bull. Amer. Meteor. Soc.*, **60**, 115-123.
- Marsham, J. H., S. B. Trier, T. M. Weckwerth, and J. W. Wilson, 2011: Observations of elevated convection initiation leading to a surface-based squall line during 13 June IHOP_2002. *Mon. Wea. Rev.*, **139**, 247-271.

- McCoy, L. P., 2014: Analysis of heavy-rain-producing elevated thunderstorms in the MO-KS-OK region of the United States.
- Means, L. L., 1952: On thunderstorm forecasting in the central United States. *Mon. Wea. Rev.*, **80**, 165-189.
- Miller, M. L., V. Lakshmanan, and T. M. Smith, 2013: An automated method for depicting mesocyclone paths and intensities. *Wea. Forecasting*, **28**, 570-585.
- Moore, J. T., and G. E. VanKnope, 1992: The effect of jet-streak curvature on kinematic fields. *Mon. Wea. Rev.*, **120**, 2429–2441.
- Moore, J. T., A. C. Czarnetzki, and P. S. Market, 1998: Heavy precipitation associated with elevated thunderstorms formed in a convectively unstable layer aloft. *Meteorol. Appl.*, **5**, 373-384.
- Moore, J. T., F. H. Glass, C. E. Graves, S. M. Rochette, and M. J. Singer, 2003: The environment of warm-season elevated thunderstorms associated with heavy rainfall over the central United States. *Wea. Forecasting*, **18**, 861-878.
- Newman, J. F., V. A. Lakshmanan, P. L. Heinselman, M. B. Richman, and T. M. Smith, 2013: Range-correcting azimuthal shear in Doppler radar data. *Wea. Forecasting*, **28**, 194-211.
- Nowotarski, C. J., P. M. Markowski, and Y. P. Richardson, 2011: The characteristics of numerically simulated supercell storms situated over statistically stable boundary layers. *Mon. Wea. Rev.*, **139**, 3139-3162.
- Parker, M. D., 2008: Response of simulated squall lines to low-level cooling. *J. Atmos. Sci.*, **65**, 1323-1341.
- Przybylinski, R. W., 1995: The bow echo: Observations, numerical simulations, and severe weather detection methods. *Wea. Forecasting*, **10**, 203–218.
- Rochette, S. M., and J. T. Moore, 1996: Initiation of an elevated mesoscale convective system associated with heavy rainfall. *Wea. Forecasting*, **11**, 443–457.
- Rochette, S. M., J. T. Moore, and P. S. Market, 1999: The importance of parcel choice in elevated CAPE computations. *Natl. Wea. Dig.*, **23** (4) 20–32.
- Scharfenberg, K. A., D. J. Miller, T. J. Schuur, P. T. Schlatter, S. E. Giangrande, V. M. Melnikov, D. W. Burgess, D. L. Andra, M. P. Foster, and J. M. Krause, 2005: The Joint Polarization Experiment: Polarimetric radar in forecasting and warning decision making. *Wea. Forecasting*, **20**, 775-788.

- Schumacher, R. S., 2015: Sensitivity of precipitation accumulation in elevated convective systems to small changes in low-level moisture. *J. Atmos. Sci.*, **72**, 2507-2524.
- Smith, T., and K. L. Elmore, 2004: The use of radial velocity derivatives to diagnose rotation and divergence. Preprints, *11th Conf. on Aviation, Range, and Aerospace*, Hyannis, MA, Amer. Meteor. Soc., P5.6.
- Smull, B. F., and J. A. Augustine, 1993: Multiscale analysis of a mesoscale convective complex. *Mon. Wea. Rev.*, **121**, 103-132.
- Thompson, R. L., C. M. Mead, and R. Edwards, 2007: Effective storm-relative helicity and bulk shear in supercell thunderstorm environments. *Wea. Forecasting*, **22**, 102-115.
- Trier, S. B., and Parsons, 1993: Evolution of environmental conditions preceding the development of a nocturnal mesoscale convective complex. *Mon. Wea. Rev.*, **121**, 1078-1098.
- Tuttle, J. D., V. N. Bringi, H. D. Orville, and F. J. Kopp, 1989: Multiparameter radar study of a microburst: Comparison with model results. *J. Atmos. Sci.*, **46**, 601-620.
- Wakimoto, R. M., 1982: The life cycle of thunderstorm gust fronts as viewed with Doppler radar and rawinsonde data. *Mon. Wea. Rev.*, **110**, 1060-1082.
- Williams, R., 1991: Comments on thunderstorms above frontal surfaces in environments without positive CAPE. Part I: A climatology. *Mon. Wea. Rev.*, **119**, 2511-2513.
- Wilson, J. W., and R. D. Roberts, 2006: Summary of convective storm initiation and evolution during IHOP: Observational and Modeling Perspective. *Mon. Wea. Rev.*, **134**, 23-47.